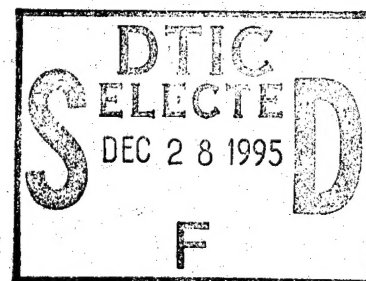# Damage Development Mechanisms in Notched Graphite Epoxy Composite Laminates during Compressive Fatigue Loading

Virginia Polytechnic Inst. and State Univ.
Blacksburg

DTIC
SELECTED
DEC 2 8 1995
F

Nov 81

19951226 018

DISCLAIMER NOTICE

UNCLASSIFIED

Technical Report
distributed by

**DEFENSE
TECHNICAL
INFORMATION
CENTER**

DTIC Acquiring Information-
Imparting Knowledge

Cameron Station
Alexandria, Virginia 22304-6145

UNCLASSIFIED
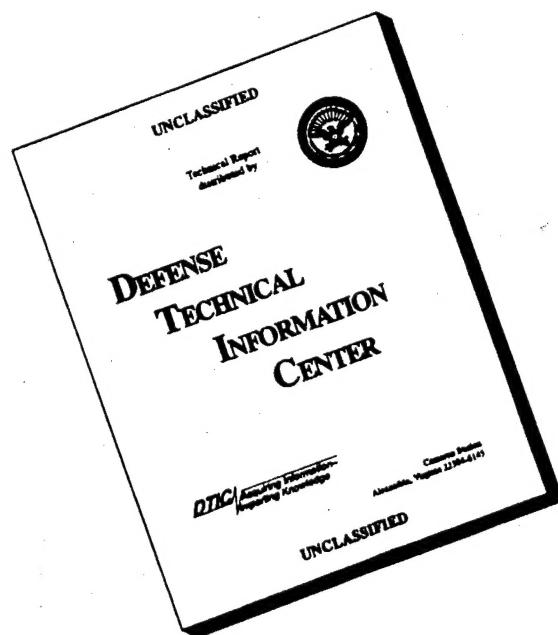
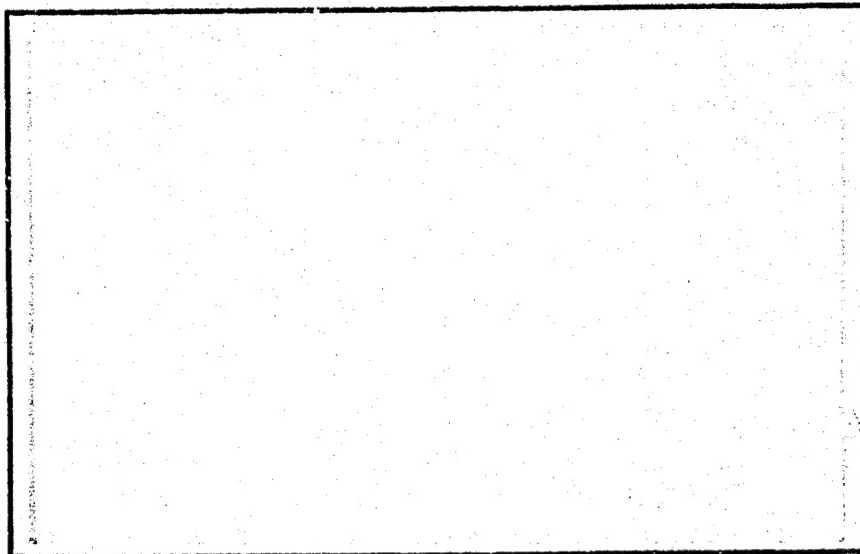## THIS DOCUMENT IS BEST QUALITY AVAILABLE. THE COPY FURNISHED TO DTIC CONTAINED A SIGNIFICANT NUMBER OF PAGES WHICH DO NOT REPRODUCE LEGIBLY.

OF COLLEGE ENGINEERING

VIRGINIA POLYTECHNIC INSTITUTE AND STATE UNIVERSITY

BLACKSBURG, VIRGINIA

BIBLIOGRAPHIC INFORMATION

Damage Development Mechanisms in Notched Graphite Epoxy
Composite Laminates during Compressive Fatigue Loading,

Nov 81

Norman Frederick Black.

PERFORMER: Virginia Polytechnic Inst. and State Univ.,
            Blacksburg. Dept. of Engineering Science and
            Mechanics.
            VPI-E-81.34

This study has investigated the damage development
mechanisms in notched graphite epoxy composite laminates
during constant amplitude compressive fatigue loading.
Laminates of two different stacking sequences were tested.
The effect of the center notch on local stress-strain
behavior during static loading, and the relationship between
fatigue damage and the resulting life, stiffness, and
strength of the laminates have been observed.

VPI-E-81.34

DAMAGE DEVELOPMENT MECHANISMS IN NOTCHED GRAPHITE EPOXY
COMPOSITE LAMINATES DURING COMPRESSIVE FATIGUE LOADING

by

Norman Frederick Black

Department of Engineering Science and Mechanics
Virginia Polytechnic Institute and State University
Blacksburg, Virginia 24061-4899

November 1981

Accesion For		
NTIS CRA&I	☑	
DTIC TAB	☐	
Unannounced	☐	
Justification		
By		
Distribution /		
Availability Codes		
Dist	Avail and / or Special	
A-1		

ACKNOWLEDGEMENTS

TABLE OF CONTENTS

iii

LIST OF TABLES

LIST OF FIGURES

I. INTRODUCTION

1.1 Scope

Fibrous composite materials have become standard structural features in many of today's engineering designs. Military aircraft manufacturers must implement composite materials to remain competitive in an industry that demands strong and lightweight aircraft. In areas where high strength and stiffness to weight ratios are required, composite materials emerge unquestionably as prime material candidates. Because of these qualities, composite materials show great promise for large scale usage in the transportation industry as energy costs continue to increase.

Composite material technology has been developed to date almost exclusively by the aerospace and aircraft industries. The current state-of-the-art is well illustrated by McDonnell Aircraft Company's AV-8B Harrier Aircraft. By constructing the tail and wing skins, and forward fuselage out of graphite epoxy, a weight savings of 430 pounds was achieved over conventional materials [1]. The significance of this design is that the forward fuselage was completely constructed out of composite materials. In the past, composites have been limited to flat plate-like structures, such as wing skins and control surfaces, with little implementation as shells or other structural components subjected to large compressive loadings and buckling conditions.

Frequently, the design of composite structures includes discontinuities such as cutouts, notches (holes), and ply terminations. Holes are commonly required for fastening the laminate to the substructure and

1

become critical regions under compressive loadings for several reasons. The stresses and strains in the uniform portions of the laminate may be well within the safe design limits but will greatly increase in regions around the hole, causing local damage. Associated with the hole is a triaxial stress field which will promote rapid matrix deterioration. The developing damage will degrade the local stiffness components and cause microbuckling. The combined effect of the compressive loading and microbuckling will accelerate damage growth and lead to local failure. Clearly, the need exists for experimental observations relating the stress field in the vicinity of the hole to the developing compressive damage.

The design of composite structures for compressive loadings requires a unified understanding of the compressive behavior of the material. The approach toward an understanding must include attempts to:

- determine the damage types and their associated growth patterns, or collectively, damage mechanisms,
- relate the damage mechanisms to the state of stress and type of loading (i.e., static and fatigue),
- determine the effects of damage on the life, stiffness, and strength of the laminate, and
- predict the response of larger structures from laboratory data. Paralleling this effort must be the development of nondestructive investigation methods to accurately monitor damage in laboratory laminates and in-service structures.

1.2 Literature Summary

The compressive damage characteristics of graphite epoxy composite laminates have been given considerable attention recently in the literature. The possibility of inducing out of plane deflections makes compression testing much more cumbersome than tension testing. Several different test fixtures and procedures have been developed to handle this behavior [2-6], and the test methods have been investigated to observe the dependence of compression data on test parameters [3-6]. Investigators have characterized the compressive damage mechanisms for several popular families of laminate configurations under static and fatigue loadings [4,7,8]. Some studies have been concerned with the effects that the environment has on compressive material response [4,9-12]. Efforts have been made to mathematically model compressive fatigue damage and predict life and residual strength [8,13]. Collectively, these efforts are directed toward a unified understanding of the compressive response of graphite epoxy laminates. Although this investigation is not directly concerned with all of the areas mentioned above, a brief summary of the literature is helpful in placing the objectives and conclusions of the present investigation in proper perspective.

Jamison and Black [2] have demonstrated that, for thin laminates, the resistance to out of plane (lateral) deflection can be used to empirically predict elastic column buckling. A loading jig was used to impart a small load perpendicular to the specimen surface at a given in-plane compressive load. The ratio of the lateral load to the measured

lateral deflection is the contrived lateral stiffness corresponding to the in-plane compressive load. The lateral stiffness was measured at several in-plane compressive loads and the relationship was used to predict the buckling load; i.e., the in-plane compressive load producing zero lateral stiffness. The predicted buckling load for the case of a [0/90/0/90]$_s$ graphite epoxy specimen was in excellent agreement with the experimentally measured value. The utility of this technique has not yet been fully appreciated to date.

Clark and Lisagor [3] compared the results of three popular loading methods for compressive behavior of T300/5208 graphite epoxy composite specimens. Compression tests were performed using a modified IITRI "wedge grip" fixture, a face-supported fixture, and an end-loaded-coupon fixture. It was found that each of these fixtures were able to provide reliable compressive property data in certain instances. The IITRI fixture provided consistent data for unidirectional specimens while the face-supported fixture provided the most consistent results for [±45/∓45]$_s$ specimens. Modulus data were essentially the same for all three fixtures except in the case of the [±45/∓45]$_s$ specimens tested with the IITRI fixture which showed a large variation with specimen width. Strength values were found to be strongly dependent on the specimen width in [±45/∓45]$_s$ specimens tested with the IITRI fixture. This was attributed to an increased biaxial state of stress existing in narrower specimens resulting from the high Poisson's ratio under axial load. It was also noted that specimens experiencing large strain variations across the surface during testing had lower compressive strengths than more uniformly strained specimens.

Sandorff, et al. [4] have developed a test fixture which models the in-service compression response of composite laminates. Thin laminates are supported by fixtures placed at regular intervals which make line contact with the specimen surface. This produces a multipinned support condition which prevents gross out of plane buckling. Thus, the laminate can withstand a higher load than that which would cause elastic buckling in the fixed end, unsupported free length situation, while still experiencing local buckling.

Sandorff, et al. have classified compressive column failures as being geometry controlled, material integrity controlled, or some combination of these. Pure elastic instability occurs in long columns while fully supported columns fail in a crushing, delamination, or shear mode, or a combination of modes. Failure in long columns is therefore geometry controlled while material integrity controls failure in the fully supported columns. Short columns represent the case of combined long and fully supported column failure. The Euler buckling equation was found to be nonconservative in the short column range. It was suggested [9] that the consideration of shear stiffness as well as bending stiffness in the buckling equation would produce better predictions over the entire range of lengths.

Rosenfeld and Gause [5] have compressively fatigued composite faced honeycomb sandwich specimens in four point bending to simulate actual in-service conditions. The specimens were initially impact damaged to levels common in aircraft structures. The impact damaged area did not grow during fatigue, instead the damage in the impacted area became more

severe during cyclic loading. They also reported that center notched specimens showed improvements in compressive fatigue performance when mechanical fasteners were used as local constraints. In these specimens the stress producing a fatigue life in the region of 10^4 cycles increased by approximately 10 percent. It was also noted that the compressive fatigue characteristics of graphite epoxy laminates show strain rate dependency.

Phillips [6] has reported the effect of local buckling on the compressive fatigue life of notched graphite epoxy specimens. Specimens with center holes were fatigued with antibuckling plates containing cutout windows. The size of the windows were varied to allow changes in the specimen free length. It was found that decreasing the free length, and therefore the amount of local buckling, significantly increased the fatigue life. The investigation also included the effect of load truncation in a standardized load spectrum test on fatigue life. The removal of either the high or low loads in the spectrum produced lives greater than those obtained in complete spectrum tests. Life increases were most noticeable with truncations at the high load end.

An excellent description of compression fatigue damage mechanisms is provided by Saff [7]. The general damage sequence begins with intralaminar matrix cracking occurring at fiber discontinuities, such as center notches, after a very few load cycles. Depending upon the stacking sequence, delamination may develop independently or follow severely cracked regions. The interaction of delamination and intralaminar cracking degrades the matrix which reduces fiber support and load transfer in compression and tension, respectively.

Saff described the different compressive damage growth patterns in fiber and matrix dominated notched laminates. The fiber dominated laminates initially crack in the zero deg. plies at tangents to the hole in the loading direction. These zero deg. ply cracks form bounds on the ensuing matrix cracks and delaminations that occur, both in the plane and through-the-thickness. Failure will occur before large scale damage can spread outside this region. Final failure is governed by fiber instability brought on by matrix deterioration. In matrix dominated laminates, a region of intense damage grows perpendicular to the load direction and is bounded by cracking in off-axis plies, typically $\pm$45 deg. plies. Extensive delamination will usually develop and cracks in the zero deg. plies will extend beyond this region. Failure may be governed by dominant delamination growth or local fiber collapse brought on by matrix deterioration.

Whitcomb [8] has investigated the tensile and compressive fatigue characteristics of notched orthotropic ($[0/\pm45/0]_s$ and $[45/0/-45/0]_s$) and quasi-isotropic ($[90/\pm45/0]_s$ and $[45/90/-45/0]_s$) laminates. The fatigue damage observed consisted of matrix cracking and delamination. Delaminations grew in alignment with the load direction in the ortho-tropic laminates and less so in the quasi-isotropic laminates. Plies cracked in the same regions as they delaminated, but there seemed to be no correlation between crack density and delamination extent. Ply cracks did not directly propagate into adjacent plies of differing fiber orientation; however, in some instances, they did join with delami-nations to form continuous links through-the-thickness. Micrographs of deplied lamina indicated very few broken fibers, and fracture surfaces

revealed very little fiber-matrix disbonding. It was concluded that fiber orientation and the sign of the loading affected delamination growth. Fatigue loading was found to cause only small longitudinal stiffness changes, $\pm$(3 to 7) percent, for both compressive and tensile loading.

The effects of high temperature and moisture environments on static compressive properties have been studied by Lauraitis and Sandorff [9], Ryder [10], and Wang [11]. Lauraitis and Sandorff found the elastic strength of long-column laminates to be unaffected by moisture and temperature. Strength decreases due to environmental effects in intermediate and fully supported columns were dependent on the material system and laminate configuration. Ryder and Wang found strength decreases of 20 and 30 percent, respectively, in zero deg. laminates subjected to high temperatures and an elevated moisture content. Wang noted that the effects of temperature and/or moisture on stiffness were minimal in $[0]_8$ laminates but more significant in $[\pm45]_{2s}$ laminates. The influence of moisture content on strength was insignificant as compared to high temperatures in the $[\pm45]_{2s}$ laminates.

Ryder and Walker [12] have investigated environmental effects on the static and cyclic compressive properties of notched and unnotched, quasi-isotropic laminates. High temperature and moisture content caused an increase in the dispersion of notched strength data. High temperature and humidity decreased the fatigue lives of unnotched and notched $[0/45/90/-45_2/90/45/0]_s$ coupons, as compared to room temperature results, by about a factor of 3 for unnotched specimens and 10 for

notched specimens. The residual strength of unnotched coupons were found to decrease due to fatigue loading at high temperature and humidity.

Predictions of the compressive damage growth pattern in notched laminates using finite element stress analysis data have been made. Ratwani and Kan [13], using a NASTRAN computer program, have found that the location of large interlaminar stresses coincided with the location of delaminations which grew under cyclic loading. Whitcomb [8] observed that finite element analysis accurately predicted initial delamination growth, but was inaccurate in predicting further damage. This is not surprising since the altered stress field in the damaged laminate, which is not considered in the finite element stress analysis, governs further damage growth. Delamination was largely found in regions of high inter-laminar shear and normal tensile stresses, but was also found in regions of high interlaminar shear and compressive normal stresses.

A recent comprehensive literature survey by Saff [7] describes the methodologies used in predicting compressive fatigue life and residual strength in composite laminates. These methods have been categorized as empirical studies, simple degradation models, or more elaborate fatigue damage models. Empirical studies are practical for predicting fatigue life of in-service composite structures. Degradation models use simple mathematical formulations to predict life and residual strength. Fatigue damage models are mathematically more cumbersome, and in most situations less practical, than degradation models because of the complicated manner in which damage occurs in composite materials. Miner's cumulative damage rule is a popular degradation model applied to

composite materials. Miner's rule, as applied to homogeneous materials, has been reported to be very unconservative in predicting fatigue life of graphite epoxy laminates under spectrum loading [5,6]. Efforts have been made to adapt Miner's rule to composite materials by including non-linear damage parameters.

A damage model of notched laminates under compressive cyclic loading has been developed by Ratwani and Kan [13]. They used a macro-mechanics delamination propagation model to predict the compressive fatigue life and residual strength of a notched composite laminate. Their model is based upon a delamination growth rate equation involving the interlaminar stresses and several resin system dependent constants. Delamination growth was obtained in a manner similar to that used in calculating crack growth in metals. They assumed the existence of initial interlaminar cracks and delaminations which propagate when the induced interlaminar stresses exceed a threshold value. The threshold value and the resin system constants were determined experimentally. Integration of the propagation rate equation yielded an expression for the fatigue life as a function of the maximum interlaminar stresses and the critical delamination size (i.e. the minimum delamination size needed to cause buckling).

A three dimensional finite element analysis was used to obtain the interlaminar stresses in terms of the applied compressive stress. Interfaces having the largest stresses in excess of the threshold values are locations of dominant delaminations. These dominant delaminations propagate to critical size while other interfaces, having smaller stresses above the threshold value, experience smaller delaminations.

The critical delamination size was found in terms of the applied maximum compressive stress by incorporating the delamination geometry in the Euler buckling equation.

The residual strength prediction was also based upon the delamination propagation model. Ratwani and Kan assumed residual strength to be a product of the initial static strength and a function of the delamination growth size. Fatigue life and residual strength predictions were developed for constant amplitude and spectrum loadings.

Fatigue life and residual strength results were compiled from laminates tested during their investigation and data obtained from other studies. The interlaminar stress analysis of laminates they tested showed large shear stresses with relatively small normal tensile stresses. This justified considering only interlaminar shear stresses in the delamination propagation model. Good agreement was found between theoretical life predictions and experimental results for laminates dominated by delamination growth under constant amplitude loading. However, during spectrum loading low stress level cycles produced significant intralaminar matrix damage. This intralaminar matrix degradation brought about fiber buckling at the higher spectrum loads which led to failures not accounted for by the delamination model.

Ratwani and Kan also investigated compressive residual strength degradation for laminates tested under spectrum loading. In these laminates the interlaminar stresses were not large enough to produce significant delamination and, hence, very little compressive residual strength degradation was observed experimentally and predicted analytically.

The general types of Nondestructive Inspection (NDI) techniques currently used for damage detection in graphite epoxy laminates are described by Saff [7]. Ryder has discussed in detail and has recommended those techniques applicable for studying damage mechanisms in graphite epoxy laminates [10]. References pertaining to the specific types of NDI used in this investigation are mentioned briefly in the experimental investigation section.

1.3 Objectives

The objectives of this study are to determine the damage mechanisms in notched graphite epoxy laminates under compressive cyclic loading and to ascertain the effects of such damage on the life, strength, and stiffness of the laminate. Quasi-static compression tests are performed to observe the static behavior of the notched laminate and to compare damage development in static and cyclic loadings. Extensive study of a 48 ply laminate with Nondestructive Inspection and other methods are made to detect, quantify the extent of, and monitor the development of compressive fatigue damage. Those methods which are most informative in reporting the damage of the 48 ply laminate are used in a similar test program on a 42 ply laminate. Conclusions are made concerning damage within each laminate. Both laminates are compared, on the basis of ply orientation, to note the differences and/or similarities of the developed damage. A finite element stress analysis of the 48 ply laminate, developed by Ratwani and Kan [18] is used in correlating the observed damage with the calculated stress field.

II. EXPERIMENTAL INVESTIGATION

2.1 Specimen Description

This program was conducted using specimens of AS/3501-6 graphite epoxy cut from panels with two different stacking sequences. The first study was made on specimens with a Type A stacking sequence of $[\pm 45, 0_2, \pm 45, 0_2, \pm 45, 0, 90]_{2s}$. These specimens were approximately 5.5 in. long, 1.0 in. wide, 48 plies thick, and had a centered 0.25 in. diameter hole. A second study was made on specimens with a Type B stacking sequence of $[\pm 45, 90, -45, +22.5, -67.5, -22.5, +67.5, \pm 45, +67.5, +22.5, -67.5,$ $-22.5, \pm 67.5, \pm 22.5, 0_2, +22.5]_s$. These specimens were approximately 5.3 in. long, 1.0 in. wide, 42 plies thick, and had a centered 0.25 in. diameter hole. The stacking sequences of the laminate types are depicted in Figs. 1 and 2 along with a numerical code indicating relative ply position from the front face. The front face was arbitrarily chosen but maintained consistent for specimens from the same panel.

Two Type A panels and two Type B panels were used for specimen fabrication. A manufacturing defect in the first Type A panel, the absence of the 20th ply (0° ply) in the stacking sequence, yielded a 47 ply unsymmetric laminate. The first panel of each laminate type had large thickness variations and were replaced by the manufacturer with a second panel which had a more uniform thickness. Specimens from both panels of each laminate type were used in the test program, and where applicable, compared to note the effects of the initial defects on the response of the material.

The specimen naming scheme that was adopted to distinguish between the different laminate types and panels is listed in Table I. The first panel of each laminate type was cut at several locations to observe the initial defects and to determine optimum specimen length. The second panels were then cut, first into subpanels, with the relative specimen location being recorded, Fig. 3. The slenderness ratio, defined here as the ratio of the unsupported length of the specimen to the radius of gyration of the unnotched cross-sectional area, was maintained as close as possible to 50 for the 48 ply specimens and 60 for the 42 and 47 ply specimens by adjusting the specimen length. Because of the thickness variation in some specimens, differences as high as 10 percent from the nominal slenderness ratio could not be avoided without excessive time delays required during fabrication to recut the specimen length.

The hole in the notched specimens was drilled with a D series (0.246 in. in diameter) carbide drill. The specimen was clamped in a fixture so that an undersized hole could be drilled halfway through the specimen. The fixture was then turned over and located relative to the drilling axis to give a hole concentric with the original hole. A honing tool was then used to polish the hole to the final 0.25 in. diameter. Holes drilled in this manner and examined by sectioning several specimens and by borescopic inspection showed no steps due to nonconcentric holes and no surface flaws of the hole interior due to the drilling and honing process.

2.2 Mechanical Testing

All mechanical tests were run on a 50 kip servo-hydraulic MTS testing machine operated in load control with MTS hydraulic grips, Fig. 4. The mechanical tests were performed to obtain laminate properties and initiate damage.

The specimen was gripped in a clamped fashion 0.688 in. on each end. Alignment plates, machined to accommodate a specimen of 1.00 in. width and several thicknesses, were used to position the specimen and to take up the extra space in the grip housing, Figs. 5 and 6. A tight and square seating of the specimen in the alignment plate, facilitated by lightly sanding the edge of specimens with oversized widths, prevented the specimen from end "brooming." The specimen and alignment plates were placed in the testing machine and compressed with 500 lbs. to provide proper seating before the grips were closed.

The load cell, hydraulic ram, and grips were aligned when the grips were initially installed. Relative twist between the upper and lower grips was checked periodically with alignment bars, Fig. 7. Any relative twist was corrected by rotating the bottom grip, with the alignment bars in the grips, until the pointer and cross-marks on the alignment bars matched.

2.2.1 Static Testing

All specimens were quasi-statically loaded at a rate of -25 lbs./sec. with an inverse ramp signal provided by the MTS system function generator.

Notched specimens of different lengths were compressed to failure to determine the slenderness ratio required to prevent column buckling. Specimens were then statically loaded to failure while monitoring longitudinal strain, transverse strain, load, and acoustic emission. This data was used to obtain initial notched material constants, strain trends, failure modes, and compressive strengths. The compressive strength was used to calculate the maximum compressive fatigue loads.

The specimens were instrumented with an acoustic emission transducer and two, 0.125 in. gage length, double element, strain gages, Fig. 8. The gage located beside the hole, the nearfield gage, monitored local strains sensitive to damage induced by the high stresses near the hole, while the gage away from the hole, the farfield gage, provided indications of the strain field in the undamaged laminate.

After fatigue testing, damaged specimens were instrumented and compressed to failure to observe the effects of the damage on the static loading response. The compressive strength of the damaged specimens, or residual strength, was compared to the average strength value obtained from the virgin specimens to study the effect of load history and fatigue damage on strength.

2.2.2 Fatigue Testing

All fatigue tests were run in compression-compression using a 10 Hz sine wave loading function with a minimum to maximum load ratio of 10 (R = 10). Fatigue tests were performed at several maximum compressive stress values, and will be referred to as listed in Table II. Under these conditions, the local temperature increases at the hole were

measured using video thermography and were found to be approximately 2°C throughout the tests. Tests were typically run for a duration of 6×10^5 cycles, 10^6 cycles, or failure. Some tests were interrupted at selected intervals for nondestructive evaluation.

2.3 Nondestructive Inspection Methods

Several different Nondestructive Inspection (NDI) methods were used to characterize and monitor the damage that occurred during static and fatigue loadings. Some NDI methods were performed in real-time during the actual loading while others required removal of the specimen from the load frame. A description of the various NDI methods is provided in the following sections.

2.3.1 X-ray Radiography

X-ray radiographs were taken of specimens using a Hewlett-Packard 43805 N Faxitron X-ray system. All radiographs were taken with an X-ray tube voltage of 40 kV and current of 3.0 mA. The distance from the X-ray source tube to the specimen and film was approximately 21 in. Radiographs were taken with the specimen orientated parallel (flat radiographs) and perpendicular (edge radiographs) to the film allowing the X-ray beam to travel through the thickness and width, respectively. Exposure times were 0.5 minutes for the flat radiographs and 2.2 minutes for the edge radiographs. Kodak M-5 X-ray film was used and developed in Kodak X-ray film developer. The radiographs were enlarged and printed on high contrast printing paper to accentuate X-ray absorption detail.

Tetrabromoethane (Acetylene tetrabromide or TBE), an enhancement agent which is nearly opaque to X-rays, was required for detection of fatigue damage. The effect of TBE on the compressive fatigue life of graphite epoxy laminates is considered to be negligible [7]. TBE was applied inside the hole and along the specimen edge and allowed to soak in for 1 minute while the specimen was under 1000 lbs. compressive load. Prior to radiography excess TBE on the specimen surface or hole interior was removed. The sharpest and most detailed radiographs were produced by making the radiographs immediately after the TBE application. The presence of the TBE allowed delamination and ply cracking to be observed in both flat and edge radiographs, Fig. 9. The sectioning of several specimens after radiography added insight for discerning delamination and ply cracking in the radiographs.

Initial and final radiographs were taken of all fatigued specimens to observe the total accumulated damage. Several fatigue tests were interrupted periodically for radiography to monitor damage growth patterns.

2.3.2   Ultrasonic C-scan

The C-scan is particularly suited for detecting defects in the plane of a laminate plate and mapping regions of relative good and bad quality in the plate. However, the conventional C-scan does not quantify the severity of a defective region on an absolute scale, and the data is most accurately interpreted when it is compared to a C-scan of a calibrated test standard. In the present investigation the C-scan was used to determine the relative initial condition of the specimens

and the extent of delamination and dense ply cracking around the hole as a function of the loading history.

The scanning device consisted of a Sperry S80 Reflectoscope with an Automation Industries, Inc., US-450 Scanner. The specimens, along with a calibration and control specimen, were submerged in a tank of tap water acting as a coupling medium and scanned with an ultrasonic pulse generated from a 10 MHz, 0.25 inch diameter transducer. The reflecto-scope processed the series of returning echoes produced by the ultra-sonic pulse. The echoes were, in chronological order, reflected off the top surface, reflected off the bottom internal surface, and returned through the specimen after being reflected by an aluminum support plate. The specimen thickness allowed sufficient time separation of the returning echoes for an alarm gate to be positioned over the echo that reflected off the bottom internal surface. If the amplitude of the echo within the alarm gate was greater than a preset trigger level, a dark spot would be made on the recording paper. Whenever the amplitude was below the trigger level, the recording paper would not be marked, indi-cating a relatively poor region.

Specimens of the same subpanel were C-scanned together prior to being tested to compare the initial material state and drilling damage. Several fatigue tests were interrupted at selected points for C-scanning. This sequence of C-scans was compared for relative changes, an indication of fatigue damage. This required a reliable means of recalibrating the system to the levels used in producing the initial C-scan. The calibration specimen used for this purpose consisted of a

sheet of aluminum shim stock containing three small holes attached to a virgin specimen with an epoxy bonding agent, Fig. 10.

During the initial C-scan several system parameters were recorded, including: the transducer position, dB gain, pulse length, signal reject level, filter modes, and the amplitude of the echo off the bottom internal surface (recorded from the CRT screen) at each of the holes in the aluminum sheet on the calibration specimen. The aluminum sheet completely disperses the ultrasonic signal, allowing the operator to locate each of the holes. This effectively produces consistent material points from which the system can be recalibrated.

Recalibrating the system for subsequent C-scans is accomplished by first resetting the system parameters and matching the amplitude of the returning echo, mentioned above, at each of the holes in the sheathing on the calibration specimen to the initially recorded values by adjusting the pulse length and reject level. The final step is to produce a C-scan of the control specimen within acceptable agreement of the initial C-scan, again by adjusting the pulse length and reject level.

2.3.3 Ultrasonic Attenuation

It has been shown by Hayford and Henneke [14] that delamination and matrix cracking in graphite-epoxy specimens can be detected by measuring the amplitude attenuation of an ultrasonic pulse propagated through the laminate thickness using the pulse-echo method. The pulse-echo method measures attenuation in composite laminates with the use of a delay block for time resolution of the echoes. An analysis of the path

followed by the echoes in the specimen and delay block indicates that
the measured changes in ultrasonic attenuation can be accounted for by
diffraction or scattering effects caused by the developing damage state
in the material. This method is useful during fatigue testing where
there is emphasis on determining damage initiation and rate of
propagation.

Ultrasonic attenuation in the pulse-echo mode was monitored during
fatigue testing of several specimens using the equipment shown in
Fig. 11. A Matec Model 6000 R.F. Pulse Generator and Receiver was used
to operate a Panametrics M109 transducer at a frequency of 4.7 MHz. The
transducer and delay block were centered over the hole and attached with
a C-clamp using stopcock grease as a coupling agent. A Matec Model 2470A
Attenuation Recorder measured the amplitude attenuation between a pair
of multiply reflected echoes between the transducer and back surface of
the delay block. The amplitude attenuation was plotted on a stripchart
recorder.

The entire system was triggered once during every loading cycle at
95 percent of the maximum compressive load. A Schmitt Trigger Circuit,
monitoring the ± 10 V sine wave from the MTS signal generator, would
trigger the pulser at the desired load level. Selectively firing the
system eliminated any influence the load had on the amplitude atten-
uation value. Since the attenuation recorder requires several seconds
to respond to signal changes, the amplitude attenuation values are
slightly distorted.

2.3.4   Acoustic Emission

During the quasi-static tests, acoustic emission was monitored to detect the initiation of damage in the laminates. Although acoustic emission data is difficult to interpret in terms of discrete damage events (matrix cracks, fiber fracture, delamination, etc.) for the laminates tested in this investigation, the data was consistent with observations made using the strain trends for detecting damage initiation.

The acoustic emission transducer was attached to the specimen with rubber bands wrapped with masking tape centered at 0.75 in. from the hole, Fig. 8. Stopcock grease was used as the coupling medium. The transducer signal was passed through a preamplifier, a differential amplifier, and then a digital counter. The digital counter recorded the number of events occurring in one second within a frequency band of 10-100 kHz. Only voltages above a preset gate level of 0.1 V were counted to eliminate the influence of noise. The counter output was converted to an analog signal and recorded as counts per second on a x-y plotter. A final plot of load vs. counts per second was made.

2.3.5   Stiffness Monitoring

O'Brien and Reifsnider [15], and Camponeschi and Stinchcomb [16] have shown that stiffness change is an indication of tensile fatigue damage in thin composite laminates and, in some instances, may be used to predict damage growth. Changes in stiffness data in previous studies have correlated very well with data from other NDI techniques which monitor damage, such as, acoustic emission and ultrasonic attenuation [17].

In addition to stiffness change, the growth of damage in a compressively loaded laminate may induce local out-of-plane deflections, or microbuckling. The presence of microbuckling will further change the measured stiffness values. Unlike the tensile case, where the loading does not produce a stability problem, the compressively loaded laminate experiences microbuckling which will quickly propagate until total failure, with little prior stiffness change in the direction of loading. However, once instability occurs, axial stiffness values measured in the vicinity of any microbuckling will change drastically.

The anisotropic behavior of composite laminates renders damage directionally dependent. Therefore, changes in the stiffness values would also be expected to show directional dependence. The effect of direction on stiffness was investigated by monitoring longitudinal stiffness (E_L) and a contrived transverse stiffness (E_{LT}), defined here as the ratio of the longitudinal compressive stress to the resulting transverse strain. The change in contrived transverse stiffness is a measure of the change in Poisson's ratio (ν_{LT}), and therefore, the contrived transverse stiffness is a Poisson stiffness.

During static loading, longitudinal and transverse strain, measured with the nearfield and farfield strain gages, and load, measured by the MTS load cell, were used to plot a load-strain curve. Abrupt changes and nonlinearities in these curves were possible damage indications. Changes between initial longitudinal modulus and final secant modulus were calculated for possible trends indicating final failure.

During cyclic loading a programmable calculator was interfaced with a digital processing oscilloscope to monitor changes in either the longitudinal secant modulus or contrived transverse secant modulus, computed between the minimum and maximum compressive loads. A discrete curve of percentage modulus change vs. fatigue cycles was plotted. The longitudinal and transverse strains were measured with 1.00 in. and 0.50 in. gage length MTS clip-on extensometers, respectively. The extensometers were centered about the hole in the direction of the desired strain measurement, as shown in Figs. 12A and 12B. Epoxy tabs, formed out of an epoxy two-part adhesive, were initially used to anchor the extensometer knife edges to the specimen surface. The extensometer was held fixed to the specimen with rubber bands, and grooves were cut into the epoxy tabs to accomodate the knife edges. The knife edges were found to cut into the epoxy grooves during cycling, resulting in a significant amount of strain drift. To increase the reliability of strain data, the epoxy tabs were replaced with aluminum tabs with shallow slots which were bonded to the specimens with the epoxy two-part adhesive. Strain drift during cyclic loading was greatly reduced by this technique. X-ray radiographs and visual inspection after each test did not detect any disbonding between the tabs and specimen surface.

2.4 Replication and Sectioning

Specimens were sectioned to observe the type, extent, and location of fatigue damage present. This information helped in clarifying damage patterns appearing on the X-ray radiographs. Replication, the process of making impressions of surface material microstructure on

acetone-softened acetate film, was used to view the sectioned edges for damage. Microphotographs, using standard light microscopy, were also taken of selected regions of the sectioned edges.

Sections were made transversely and longitudinally to the specimen loading axis at several locations with a diamond saw. The first section was made just outside the damage region as viewed on the radiograph. Subsequent sections were cut parallel to the initial section at distances closer to the hole edge. The last section was made as close to the hole edge as possible without cutting into the hole.

The sections were polished on a polishing wheel using, first, 5 micron, and then, 3 micron, aluminum oxide powder for 5 minutes each. Replicas of the polished surfaces were made using 5 mils thick replicating tape. The tapes were mounted in glass slides and viewed in a microfiche reader at 48X.

2.5 Summary of Test Program

The purpose of the multi-phase test program was to determine the nature of damage induced in graphite epoxy composite laminates with center holes under cyclic compressive loading and to establish the influence of such damage on the life, residual strength, and stiffness of the laminate under uniform environmental conditions. The interactions of the various parts of the program are summarized in Fig. 13 and the test matrices are shown in Tables III, IV and V.

III. RESULTS

3.1 Static Tests

The relationship between the nominal compressive stress (defined as the applied compressive load divided by the unnotched cross-sectional area) and strain was observed for each of the laminate types. Plotted in Figs. 14 and 15 are the stress-strain curves of a 47 and 42 ply specimen, respectively. The plot of compressive stress vs. farfield longitudinal strain in the 47 ply specimen is linear to a stress less than 50 ksi where a 'knee' is evident. The transverse strain measured at this location also increases linearly with stress to a 'knee' greater than 40 ksi. The nearfield longitudinal and transverse stress-strain curves became nonlinear at a stress less than 20 ksi, and the nearfield strains were larger than the corresponding farfield strain components throughout the loading due to the stress concentrations occurring around the hole. The stress-nearfield transverse strain curve also shows a flat region prior to failure. The nominal compressive stress at failure was 50.2 ksi. Acoustic emission was found to greatly increase at 47 ksi, noted by an asterisk in Fig. 16, which corresponded with the flattening of the stress-nearfield transverse strain curve. The acoustic emission plot also shows nearly all of the detected events occurred at stresses greater than 20 ksi, where the stress-nearfield strain curves became nonlinear.

The static response of specimen 1-1 is representative of all the 47 and 48 ply specimens. Static data for the 47 and 48 ply specimens are recorded in Tables VII and VIII, respectively. In all cases the

26

stress-nearfield strain curves became nonlinear early in the loading.
The nearfield transverse strain was very sensitive to microbuckling and
gave strong indications of ensuing failure prior to specimen rupture.
The nearfield longitudinal strain was, in most cases, much greater than
the corresponding farfield strain at failure while both transverse
strains were nearly equal at failure. In several 47 ply specimens,
microbuckling at the nearfield strain gage resulted in rapid strain
decay or growth at failure. A comparison of the initial longitudinal
modulus to the final secant modulus, a measure of the amount of local
material yielding and microbuckling, shows increases or decreases
depending upon the sign of the local curvature at the strain gage.
Usually the nearfield gage detected a much greater longitudinal modulus
change at failure than the farfield gage, although in some cases they
were nearly equal. No significant amounts of acoustic emissions
occurred before the stress-nearfield strain curves became nonlinear.
It appears from this data that local damage begins at a nominal stress
of 20 ksi, or approximately 40 percent of the static strength, and that
cyclic compressive stresses greater than 20 ksi should produce fatigue
damage.

The response of the 42 ply laminates shows greater amounts of
microbuckling at the nearfield strain gage than was shown in the 47 and
48 ply laminates. The nearfield longitudinal strain of specimen 2-7
decayed to zero strain and the nearfield transverse strain (not shown in
Fig. 15) changed sign. The opposite is true for specimen 2-10 where the
nearfield longitudinal and transverse (not shown in Fig. 15) strain

rapidly increased in compressive and tensile values, respectively, prior to failure. The differences in behavior between the two specimens is due to the local out-of-plane deformation around the hole. In the case of specimen 2-7, the local curvature at the strain gage decreased the absolute value of the strains, whereas the local curvature in specimen 2-10 caused increases in the absolute values of the two strains. The farfield stress-strain curves were similar to those of the 47 and 48 ply specimens but in some cases the curves had flat regions prior to failure, as in the stress-longitudinal strain curve of specimen 2-7.

The static data for the 42 ply specimens are recorded in Table VI. Differences between the initial longitudinal modulus and final secant modulus, at failure, at the farfield gage varied from +14.3 to -36.5 percent. Because of the large amount of surface curvature at failure, at the nearfield gage, change in modulus values were of no practical interest and were not recorded. Acoustic emission was not monitored for the 42 ply specimens. From the nearfield strain data, nonlinearities in the stress-strain curves suggest that damage starts in the 42 ply specimens at a stress between 40 and 50 percent of the static strength and cyclic compressive stresses greater than this level should produce fatigue damage.

The 42 ply laminate, having only ten percent zero deg. fibers is not as strong as the 47 and 48 ply laminates, having approximately 40 percent zero deg. fibers. The average virgin compressive strengths of the 42, 47 and 48 ply specimens were 27.6, 46.0, and 49.8 ksi,

respectively. The strengths were used as references to determine the cyclic stress levels used in the fatigue tests and to study the effect of fatigue load history on residual strength. In all cases, the specimens failed in a crushing mode. Although global buckling with visual out-of-plane deformation was not evident, the stress-strain data does suggest some local out-of-plane deformation at the hole occurred in some cases.

3.2 Fatigue Tests

Fatigue tests of the 42, 47 and 48 ply laminates were run at several stress levels (recorded in Table II) to observe the effects of cyclic loading on damage development and subsequent life, stiffness, and strength of the laminates. Several specimens of each type were run to failure to obtain the fatigue lifetime, and the remaining specimens were monitored using NDI to observe the fatigue damage. Specimens that survived the cyclic loading were either sectioned to observe the internal damage or monotonically loaded in compression to obtain the residual strength.

3.2.1   Life Data

The S-N data for the 42, 47 and 48 ply laminates are plotted in Figs. 17 and 18, respectively. At an applied maximum cyclic compressive stress of 40 ksi (80 percent of the compressive strength of the 48 ply laminate), several 47 and 48 ply laminates failed in fatigue before 5×10^5 cycles. Three other tests were terminated after approximately 4×10^5 cycles. Specimens run at stresses of 30 and 35 ksi survived 10^6 cycles with no fatigue failures.

The 42 ply laminates did not fail during cyclic loading unless the maximum cyclic compressive stress approached the average static strength of the laminate. Six specimens were cycled at a maximum compressive stress of 26 ksi (94 percent of the average static strength), four survived 10^6 cycles. The 26 ksi stress level is slightly lower than the lowest value of virgin static strength, recorded in Table VI, and it is possible that the two specimens that failed in fatigue had static strengths on the low side of the strength distribution.

Figures 17 and 18 indicate the presence of a threshold stress or fatigue limit at approximately 26 ksi for the 42 ply laminates and 40 ksi for the 47 and 48 ply laminates. Cyclic compressive stresses greater than the threshold values will cause fatigue failure; and cyclic compressive stresses less than the threshold value will not cause failure before 10^6 cycles, although such stresses may cause damage in the specimens.

3.2.2 Stiffness Monitoring Data

The longitudinal and contrived transverse secant moduli (defined in section 2.3.5) were monitored during cyclic loading, and in some cases, the static secant modulus was recorded before and after cycling for comparison. The static and dynamic secant moduli were calculated between zero and a stress equal to 80 percent of the static compressive strength, and between minimum and maximum cyclic compressive loads, respectively. The dynamic modulus data are plotted vs. cycles in Figs. 19 and 20 and the final changes in the static and dynamic moduli are listed in Table IX.

The longitudinal secant modulus of the 47 and 48 ply specimens was monitored in three tests, showing no change at the low stress level, increasing by 7 percent at the medium stress level, and decreasing by 4 percent at the high stress level. The low and medium stress level tests were run for 10^5 cycles and the high stress level test was run to approximately 4×10^5 cycles. The corresponding static modulus values were not recorded in these tests. The decrease in the longitudinal secant modulus observed in the high stress level fatigue test is a combination of fatigue damage and wear of the epoxy tabs by the extensometer knife blades. Most of the decrease occurred within the first 2.5×10^4 cycles. The change in longitudinal secant modulus was similar in trend during the low stress level fatigue test. The modulus decreased 2 percent early in the test and then increased back to the initial value. The low stress level fatigue test was also run with epoxy tabs. In general, variations of about 2 percent in moduli values were observed to be the sensitivity limit of the calculating system. All other fatigue tests in which stiffness was monitored were run using aluminum tabs, described in section 2.3.5, to prevent tab wear by the extensometer knife blades.

The sign of the modulus value change is dependent upon the curvature of the specimen in the extensometer gage length. Initially, if the curvature produces a secant modulus less than the tangent modulus, changes resulting from fatigue damage will decrease the secant modulus. The opposite is true if, in the undamaged specimen, the secant modulus is greater than the tangent modulus.

The contrived transverse secant modulus was monitored in three tests of the 48 ply specimens. An increase of 3 percent after 10^6 cycles at the low stress level, and decreases by 5 and 15 percent after 9.8×10^6 and 6×10^6 cycles, respectively, at the medium stress level were observed. The corresponding static contrived transverse modulus of the specimens cycled at the medium stress level decreased by 17 and 18 percent.

Two 42 ply specimens were monitored for secant modulus changes during cycling at the 26 ksi stress level, which was the only stress level to produce significant amounts of damage. The dynamic and static longitudinal secant modulus increased 3 percent and decreased 2 percent, respectively, after approximately 10^6 cycles. The dynamic and static contrived transverse secant modulus, monitored in the second fatigue test, decreased 25 and 14 percent, respectively, after more than 10^6 cycles. Figure 19 shows very large variations in the dynamic contrived transverse secant modulus throughout the test. These variations are caused by out-of-plane deformations which were observed in the static tests of the 42 ply specimens.

To summarize the stiffness data, the longitudinal secant modulus of the 42, 47 and 48 ply specimens does not undergo large changes in value during cyclic loading at any of the tested stress levels. The contrived transverse secant modulus does experience large changes and, by comparison, is more sensitive to damage than the longitudinal secant modulus. The discrepancies between the static and dynamic modulus changes can be attributed to the differences in response of the laminate to static and

dynamic loadings. It must be recognized that compression testing poses
a stability problem which will produce scatter in stiffness data.
Aluminum tabs, used instead of epoxy tabs, resisted wear by the
extensometer knife blades and therefore increased the reliability of the
strain data.

3.2.3 Compressive Residual Strength Data

Specimens of each laminate type were quasi-statically loaded to
failure after cyclic loading to compare the residual strength to the
strengths of undamaged specimens (virgin specimens). All strength data
were generated under compressive load and will be discussed as absolute
values for simplicity. The residual strength data are presented in
Figs. 21 and 22, and the data are listed in Tables VI, VII and VIII.

All 47 ply specimens cycled at the low and medium stress levels had
residual strengths slightly greater than the average virgin strength for
the laminate, although four of the five values fell within the scatter
band of the virgin strength distribution. The low virgin strength value
obtained from specimen 1-11 is questionable due to an operator error
resulting in a rapid loading. Similar observations can be made about
the 48 ply specimens cycled at the low and medium stress levels. One
specimen was cycled at the medium stress level for 2.2×10^6 cycles, and
the residual strength was within the scatter band of virgin strength.
The specimen cycled at the high stress level, or fatigue threshold, did
suffer a 13 percent strength degradation after 4×10^5 cycles.

With one exception, the 42 ply specimens had residual strengths
greater than the virgin strength and these values were outside the

scatter band of initial strength. One specimen, cycled at the threshold level for 10^6 cycles, showed strength degradation. The residual strength results for the 42 ply specimens suggest that fatigue damage at the 16, 21, and 24 ksi stress levels improves the compressive strength of the notched laminates.

3.3 Fatigue Damage

X-ray radiography, ultrasonic C-scanning, edge replication of sectioned laminates, and ultrasonic attenuation were used to directly monitor fatigue damage. X-ray radiographs were compared with ultrasonic C-scans and replicas of sectioned laminates to note similarities and/or differences in damage detail. The following sections describe the results of each of these techniques.

3.3.1 X-ray Radiography

X-ray radiographs were taken before and after cyclic loading to observe the drilling and total accumulated fatigue damage, respectively. Several fatigue tests were interrupted at selected intervals for X-raying so that in-plane and through-the-thickness damage growth patterns could be studied. The radiographs have been printed on high contrast paper. Descriptions of the damage detail are made according to its appearance on the printing paper.

Flat radiographs of 42 and, 47 and 48 ply specimens taken after cyclic loading are shown in Figs. 23 and 24, respectively. The radiograph of specimen 1-7 shows a representative damage pattern for type A laminates cycled at the low stress level to 10^6 cycles. No delaminations

and relatively few matrix cracks develop. The damage consists of long longitudinal cracks tangent to the hole in the zero deg. plies and very short cracks initiating at the hole and running outward in the fiber direction in the ±45 deg. plies. The thick, dark, circular band around the hole, present in the initial radiograph, is a combination of minor drilling damage and TBE residue on the hole interior. Edge radiographs (not shown in Fig. 24) taken from specimens with a similar fatigue history as specimen 1-7 revealed most cracking occurred in the ply group (12 plies) nearest the surface.

The damage shown in the flat radiographs of specimens 8B1 (48 ply) and 1-6 (47 ply), cycled at the medium and high stress levels, respectively, consists of delaminations and matrix cracks. Delaminations appear as dark shaded regions in the flat radiographs. The superposition of several delaminations through-the-thickness produces nonuniformly shaded regions. Specimen 8B1, cycled for approximately the same duration and at a lesser maximum compressive stress than specimen 1-6, developed greater amounts of matrix cracks than specimen 1-6. The delaminated regions in specimen 1-6 were not symmetric about, or continuous around, the hole. The opposite was true in specimen 8B1, the delaminated regions were fairly symmetric about the hole and appeared to form a continuous band. In general, the radiographs indicate that specimens from the 47 ply laminate sheet are more resistant to damage induced by cyclic loading than specimens from the 48 ply laminate sheet.

The matrix cracking in specimen 8B1 was fairly symmetric and consisted of longitudinal cracks in the zero deg. plies and off-axis cracks

aligned with the fibers in the ±45 deg. plies. Longitudinal cracks, tangent to the hole, formed bounds across the width for longitudinal cracks that initiated on the hole. A band of delaminations and short, closely spaced longitudinal and off-axis cracks developed around the hole and along the longitudinal cracks tangent to the hole. One longitudinal crack that initiated on the hole was longer than the longitudinal cracks tangent to the hole, but in general, the longitudinal cracks tangent to the hole were greatest in length. Longitudinal cracks tangent to the hole are superimposed through-the-thickness in the flat radiograph, appearing as a single, thick crack. Several off-axis cracks, initiating on the hole or tangent to the hole, ran in the ±45 deg. plies toward the specimen edge, and in some cases, reached the edge. The presence of a matrix crack at an angle of about 60 deg. was also detected. This crack may be in a 45 deg. ply that was improperly positioned. The edge radiograph (not shown) shows most of the damage occurring in the ply group (12 plies) nearest the surface, but some damage was evident in the center 24 plies. Matrix cracks and delaminations were not distinguishable in the edge radiographs.

The matrix cracking in specimen 1-6 was not symmetric about the hole. Several longitudinal cracks developed toward the specimen edge outside the longitudinal cracks tangent to the hole. Off-axis cracks did not run outside the heavily damaged region surrounding the hole. Edge radiographs were not taken of the 47 ply specimens after cycling at the high stress level.

Flat and edge (not shown) radiographs were .aken of two 42 ply
specimens, 2-10 and 10B2, cycled with a maximum compressive stress of 24
and 26 ksi, respectively, after 10^6 cycles. Both specimens developed
delaminations along the side of the hole extending toward the specimen
edge, or perpendicular to the loading direction. The delaminations were
greatest in specimen 10B2. Matrix cracks in specimen 2-10 were confined
to off-axis plies at regions along the side of the hole. Matrix
cracking was much greater in specimen 10B2, containing longitudinal and
off-axis cracks tangent to and intersecting the hole. Some regions,
away from the hole, of specimen 10B2 developed many closely spaced off-
axis cracks. In both specimens off-axis cracks, appearing to develop in
the 67.5 deg. plies outlined the delaminated regions. This suggests
that the delaminations develop on interfaces of 67.5 deg. plies and are
initiated or arrested by matrix cracks in these plies. The edge radio-
graphs show most of the damage occurring in the center plies.

One 48 ply and two 42 ply specimens, cycled at the medium and
26 ksi stress level, respectively, were interrupted at selected inter-
vals for radiography. The sequence of flat and edge radiographs show
damage growth superimposed in-plane and through-the-thickness,
respectively.

The damage sequence for the 48 ply specimen is shown in Figs. 25A,
B and C. By 4.0×10^4 cycles, most of the longitudinal matrix cracks and
a thin circular delamination around the hole have developed. Many
small, off-axis cracks exist along longitudinal cracks tangent to the
hole. The edge radiograph shows damage confined to the plies near the

surface. The spotted pattern in the edge radiograph was caused by TBE deposits on the hole interior during radiography. This was prevented in subsequent edge radiographs by cleaning the hole thoroughly with acetone prior to radiography. By 4×10^5 cycles, single off-axis cracks have grown outside the damage region surrounding the hole. The small off-axis cracks that developed along the longitudinal cracks tangent to the hole have begun to grow considerably. The delaminated region between the longitudinal cracks tangent to the hole grew in the longitudinal direction. The edge radiograph shows the damage intensifying at the plies near the surface, which may be the delaminations observed in the flat radiographs, and the spread of damage to the center plies. At 1.3×10^6 cycles, off-axis cracks continue to grow toward the specimen edge, no longer an isolated occurrence. The delaminated region toward the top of the specimen, between the longitudinal cracks tangent to the hole, continued to grow, the more recent growth appearing darker than the earlier growth. The edge radiograph shows slowed but continued damage growth in the center plies and some increases in length but little new damage in the outer plies. At 2.2×10^6 cycles the delaminated region towards the top of the specimen has increased. Off-axis cracks not intersecting the hole continue to grow and, for the first time, longitudinal cracks appear to the side of the hole outside the longitudinal cracks tangent to the hole. The edge radiograph does not show a significant increase in damage.

The flat and edge radiographs of specimens 1C2 and 10B2 are shown in Figs. 26A, B and 27, respectively. The edge radiographs of specimen

1C2 did not clearly show the through-the-thickness damage, which was not uncommon. Since the X-ray beam traveled through approximately four times as much material in the edge radiograph than in the flat radiograph, greater variations in the amount of X-ray absorption exist. Therefore, the exposure time and amount of TBE absorption were more critical in producing damage detail in the edge radiographs than in the flat radiographs.

The in-plane damage development of specimen 1C2 is clearly shown in the flat radiographs. Shown at 2.5×10^4 cycles are longitudinal cracks intersecting the hole with many small off-axis cracks in the fiber direction of the 27.5 deg. plies being superimposed. Along the side of the hole were lesser amounts of longitudinal and off-axis cracks. By 2.5×10^5 cycles most crack increases occurred alongside the hole with delaminations forming. The cracks at the top and bottom of the hole have increased slightly. Shown at 10^6 cycles, the most heavily damaged region is alongside the hole having long longitudinal and off-axis cracks tangent to the hole and several small cracks of each type not intersecting the hole. The edge radiograph at 10^6 cycles shows all the damage occurring within the center plies.

The edge radiograph of specimen 10B2 at 10^6 cycles clearly shows most of the damage occurring in the center plies. The small amounts of damage near the specimen edge is a result of drilling and cyclic loading. Specimen 10B2 developed more and longer cracks, and larger delaminated regions by 10^6 cycles than specimen 1C2. Long, off-axis cracks, tangent to the hole in the fiber direction of the 22.5 deg. plies, in specimen 10B2 were not seen in specimen 1C2.

3.3.2   Ultrasonic C-scan

A comparison of C-scans and flat radiographs of two 47 ply specimens cycled at the low and high stress levels are shown in Figs. 28 and 29, respectively. In these figures the regions across the width of the specimens above and below the hole are tabs used in mounting an extensometer. The initial and final (10^6 cycles) C-scans in Fig. 28 do not reveal any delaminations. The flat radiograph at 10^6 cycles confirms the C-scan results and also shows matrix cracks parallel to the zero and 45 deg. fibers. The history of damage growth at the high stress level is shown in Fig. 29. The C-scan at 10^5 cycles reveals damage along the side of the hole. At $2x10^5$ cycles the radiograph shows delamination and cracking around the hole matching the pattern on the C-scan. C-scans at $3x10^5$ and $3.5x10^5$ cycles show the damage area growing in width and length, and the corresponding radiographs show increases in cracking and delamination.

3.3.3   Ultrasonic Attenuation

Changes in ultrasonic attenuation, Figs. 30 and 31, were observed during fatigue tests of the 42 and 47 ply specimens, respectively. The ultrasonic attenuation data for the 42 ply specimen showed steady increases throughout the test with a sudden rise and drop prior to final failure. Attenuation in the 47 ply specimens at both fatigue levels showed an initial decrease trend followed by sporadic increases at the medium stress level, and small changes at the low stress level fatigue tests.

Initial decreases in attenuation data might be attributed to settling of the coupling medium between the transducer and specimen or reseating of the transducer. Attenuation changes in the 47 ply laminate show correlation to the damage growth shown in the X-ray radiographs in that specimens cycled at the low stress level showed little damage while those cycled at the medium stress level showed more matrix cracks and some delamination.

3.3.4 Sectioning Study

Two 47 ply specimens (1-6 and 1-9) cycled at the high stress level and one 42 ply specimen (1C2) cycled at the 26 ksi level were sectioned after 4×10^5, 3.6×10^5, and 10^6 cycles, respectively. The sectioning schedule shown in Table X refers to the cut locations shown in Fig. 32. Cuts were made perpendicular to and parallel to the load axis, i.e. transverse and longitudinal sections, respectively. The sections were polished and replicated, as described in section 2.4, and the replicas were viewed in a microfiche reader at 48X. The damage was first sketched onto a worksheet and then redrawn on the final figures of the sectioned surface. Edge surfaces of virgin specimens were replicated to note the appearance of the initial state of the material, including ply interfaces, resin rich regions, and ply thickness variations. Only damage that was obviously load induced was recorded. This information was used to interpret the damage modes shown by the X-ray radiographs and to verify the extent of the damage zone.

The possibility of damage initiating in regions remote to the hole and going undetected in the X-ray radiographs was investigated during

sectioning. Radiographs were made after applying TBE to the sectioned surfaces and hole interior. In most cases, radiographs made during sectioning showed considerably less detail of the damage than radiographs made prior to sectioning, where TBE was applied under compressive load. This suggests that some delaminations and matrix cracks require compressive load for TBE penetration.

Figure 33 shows a flat radiograph of specimen 1-6 made during sectioning by applying TBE to the hole interior and surface of the first transverse section. Locations of the sectioned surfaces are indicated on the radiograph. It is apparent from Fig. 33 that damage does not extend to, or develop independently at, the first transverse section.

Figures 34A and B, 35A and B, and 36A and B show the damage observed internally in specimen 1-6 at the fourth transverse section and the third and fourth longitudinal sections, respectively. Delaminations and matrix cracks at the right side of the projected hole diameter on the fourth transverse section agree with the damage seen in the radiograph of Fig. 33. Delaminations at the left side, and matrix cracks at the middle of the projected hole diameter, did not appear in the radiograph. However, a flat radiograph (not shown) made after applying TBE along the surface of the third transverse section did show delaminations and matrix cracks in this region. Figures 37 and 38 show delamination and matrix cracking, respectively, at the fourth transverse section in pairs of zero deg. plies. Matrix cracks and fewer delaminations were found at the second and third transverse sections (not shown). No damage was found at the first transverse section, nor at the first and second longitudinal sections.

The radiograph of Fig. 33 shows matrix cracks and delaminations located at the third and fourth longitudinal sections, which were observed in the replicas. Figures 39 and 40 are portions of the replicas, copied from the microfiche viewer, of the third and fourth longitudinal sections, respectively, showing matrix cracks and delaminations of the 45/0 interfaces. Fiber damage in two neighboring zero deg. plies (plies 41 and 42), observed on both longitudinal surfaces in Figs. 39 and 40, suggests that in-plane shearing has occurred. However, the radiograph of Fig. 33 and other radiographs taken during sectioning do not reveal these failure surfaces in the zero deg. plies.

Figure 41 shows a flat radiograph of specimen 1C2 made after cycling and prior to sectioning. The location of the sectioned surfaces are indicated on the radiograph. Figures 42A and B, 43A and B, and 44A and B show the damage observed internally at the first and second transverse sections and second longitudinal section, respectively. Matrix cracks were found on both sides of the projected hole diameter at the first transverse section. The radiograph shows matrix cracks intersecting the first transverse section only at the left side of the projected hole diameter. Matrix cracks were found on both sides and middle of the projected hole diameter at the second transverse section. A light micrograph of matrix cracks observed at the second transverse section is shown in Fig. 45. No damage was detected at the first longitudinal section and only one matrix crack, shown photographed in Fig. 46, was found at the second longitudinal section. The delamination intersecting the second longitudinal section in the radiograph of Fig. 41

could not be located in the replicas or by microscopic examination of the sectioned surface.

The types and characteristics of the observed damage during sectioning of specimens 1-6 and 1C2, mentioned above, and specimen 1-9 are summarized as follows.

47 ply laminate

1. transverse sections--matrix cracks in the zero deg. plies with highest crack density in the double zero deg. plies...some cracks in the 45 deg. plies...delamination of the 45/0 interfaces in the repeated ply group (12 plies) closest to the surface of the specimen...region of delamination and severe matrix cracking in the zero deg. plies three and four of specimen 1-6.

2. longitudinal sections--matrix cracks in the 45 deg. plies... region of fiber damage in the zero deg. plies 41 and 42 of specimen 1-6...delamination of the 45/0 interfaces in the repeated ply group (12 plies) closest to the surface of the specimen.

42 ply laminate

1. transverse sections-matrix cracks in the center ten plies (the ±22.5, 0_2, +22.5 deg. plies on each side of the midplane).

2. longitudinal sections--matrix cracks in the center two 22.5 deg. plies.

The matrix cracks in all plies ran perpendicular to the plane of the specimen. Some matrix cracks in the 0 and 22.5 deg. plies of the 42 ply laminate did not go entirely through the ply thickness.

3.4 Finite Element Stress Analysis

Ratwani and Kan [18] have performed a finite element interlaminar stress analysis on the type A, 48 ply, laminate and on a 42 ply laminate similar to the type B, 42 ply, laminate. They used a NASTRAN finite element code with three dimensional 8-node elements (HEXA). The analyzed specimen was a 1.5 in. square plate containing a 0.25 in. diameter centered hole. Due to the symmetry of the laminate only one-eighth of the specimen was modeled, i.e. from the specimen surface to the laminate midplane and one-quarter of the in-plane dimension around the hole.

The 48 ply laminate was represented by 12 layers of elements. The first 10 layers modeled the 12 plies near the surface with neighboring zero deg. plies coupled together to form single layers. The interior plies were grouped together to form two layers. Layers 11 and 12 modeled plies 13 to 18 and 19 to 24, respectively. Coupling of the interior plies resulted in large interlaminar normal stresses on interfaces of layers 10, 11, and 12. Thus, the interlaminar stresses obtained at these locations were not very accurate. The interlaminar stresses obtained between the plies near the surface were more accurate since these plies were modeled as individual layers. The coupling of the interior plies was considered to not have any significant influence on the interlaminar stresses between the plies near the surface. A similar model was used for their 42 ply laminate.

Figures 47, 48, and 49 show the interlaminar stresses, normalized with respect to the applied stress, at the first, second and fourth interfaces of the 48 ply laminates, respectively. Also shown in the

figures are the element mesh and loading used in the analysis. The stresses were obtained at the centroid, in the radial direction, of the elements bordering the hole, and plotted between $0° \leqslant \theta \leqslant 90°$. The interlaminar shear stresses, τ_{rz} and $\tau_{\theta z}$, at each of the three interfaces shown are largest in the polar region $25° < \theta < 67.5°$. Also, the interlaminar normal stresses are tensile and compressive in the polar regions, $0° \leqslant \theta \leqslant 45°$ and $75° \leqslant \theta \leqslant 90°$, respectively, for compressive applied loads.

X-ray radiography, ultrasonic C-scanning, and sectioning of the damaged laminates in the present investigation showed most delaminations occurred in the polar region $0° \leqslant \theta \leqslant 45°$ and, of the interfaces mentioned above, at the second and fourth interfaces. In general, the observed delaminations developed at locations of large interlaminar shear and tensile normal stresses. However, a similar stress state existed at the first interface, and at other interfaces not mentioned above, and did not cause any delamination. Therefore, as would be expected, it is not possible to "predict" the occurrence of delamination from considering only the individual interlaminar stress components. Interlaminar damage predictions would require a micromechanics failure theory, which would consider the combined state of stress at the interface and the local material properties.

IV DISCUSSION AND SUMMARY

This study has investigated the damage development mechanisms in notched graphite epoxy composite laminates during constant amplitude compressive fatigue loading. Laminates of two different stacking sequences were tested. The effect of the center notch on local stress-strain behavior during static loading, and the relationship between fatigue damage and the resulting life, stiffness, and strength of the laminates have been observed. Several different Nondestructive Inspection (NDI) methods were used to characterize and monitor the damage that occurred during static and fatigue loadings. The NDI methods included X-ray radiography, stiffness monitoring, ultrasonic C-scanning, ultrasonic attenuation measurement, and acoustic emission monitoring. Sectioning of the damaged laminates was performed to verify the extent of the observed damage in the X-ray radiographs and ultra-sonic C-scans. Some correlations were found between locations of maxi-mum interlaminar shear stresses, obtained from the finite element stress analysis of Ratwani and Kan [18], and the initial delaminations observed during cyclic loading.

The two laminate types in this investigation had considerably dif-ferent stacking sequences. Laminate type A, 47 and 48 ply specimens (the 47 ply specimens were missing a zero deg. ply), consisted of approximately 42 percent zero deg. plies, 8 percent 90 deg. plies, and 50 percent $\pm$45 deg. plies. Laminate type B, 42 ply specimens, had approximately 10 percent zero deg. plies, 5 percent 90 deg. plies, and 85 percent off-axis (22.5, 45, and 67.5 deg.) plies. One obvious result

47

of the different stacking sequences was that the 47 and 48 ply speci-
mens, having a greater percentage of zero deg. plies, were stronger than
the 42 ply specimens. It was also observed during quasi-static compres-
sive loading that the farfield longitudinal and transverse strains,
which are not directly influenced by the stress concentrations around
the hole, were greater in absolute value at failure in the 48 ply
specimens than in the 42 ply specimens.

Stiffness changes were observed during cycling of the 42, 47, and
48 ply specimens. The dynamic longitudinal secant modulus changed
slightly, 3 to 7 percent, in the 42, 47, and 48 ply specimens. The
static and dynamic contrived transverse secant moduli showed greater
changes, 5 to 25 percent, and, therefore, are more sensitive to fatigue
damage than the longitudinal secant modulus. In one 42 ply specimen,
fatigue damage caused out-of-plane deformations resulting in a large
change in the contrived transverse secant modulus. The stiffness data
show correlation with the damage observed in the X-ray radiographs in
that specimens developing greater amounts of damage showed larger
changes in stiffness. A more descriptive relationship between the
observed damage and stiffness changes could not be determined.

The 42 ply specimens were much less sensitive to fatigue damage and
hence were more fatigue resistant than the 48 ply specimens. This is
seen by comparing the maximum cyclic compressive stress, normalized with
respect to the virgin static strength, which causes fatigue failure.
Fatigue failures did not occur in the 42 ply specimens unless the maxi-
mum cyclic compressive stress level was close to the virgin static

strength. However, the 48 ply specimens failed in fatigue when cycled with a maximum compressive stress corresponding to 80 percent of the static strength.

Some small differences between the 47 and 48 ply specimens in strength, life and cyclic damage were observed. The missing zero deg. ply in the 47 ply specimen produces an unsymmetric laminate having coupling of extension and bending. This coupling may contribute to the differences in response. However, material property variations between the 47 and 48 ply laminate panels may be the most significant factor in causing differences in the response of the laminates.

A schematic representation of the in-plane compressive fatigue damage of the 42 and 48 ply specimens is shown in Figs. 50 and 51, respectively. The 48 ply specimens developed a heavily damaged region containing many longitudinal and off-axis matrix cracks and a continuous band of delaminations completely around the hole. The 42 ply specimens developed delaminations and several, long, longitudinal and off-axis matrix cracks at the sides of the hole and a few, short, matrix cracks at the top and bottom of the hole. The 47 ply specimens had matrix cracking characteristics similar to those of the 48 ply specimens, as would be expected. However, large delaminations and matrix cracks, asymmetric about the hole, gave the 47 ply specimens a significantly different in-plane damage pattern than the 48 ply specimens.

The damage initiation begins in the 48 ply specimens after very few load cycles. Longitudinal and off-axis matrix cracks develop tangent to the hole in the zero deg. plies and alongside the hole in the 45 deg.

plies, respectively. The length of the longitudinal matrix cracks
tangent to the hole only increased slightly with additional cycles;
however they did become thicker and darker in the flat radiographs.
This suggests that the longitudinal matrix cracks tangent to the hole do
not develop simultaneously in each ply through-the-thickness. The edge
radiographs indicate that these longitudinal matrix cracks develop
initially in the outer zero deg. plies and then develop in interior
plies with additional cycles.

Following the initial cracking of the zero deg. plies in the 48 ply
specimens, longitudinal matrix cracks developed at the top and bottom of
the hole as the in-plane and interlaminar stresses were redistributed
near the hole. These longitudinal matrix cracks filled in the region
between the longitudinal matrix cracks tangent to the hole and gradually
increased in length but did not grow outside the heavily damaged region
around the hole. In one severely damaged 48 ply specimen, longitudinal
matrix cracks developed outside the longitudinal matrix cracks tangent
to the hole. However, in almost all 48 ply specimens, the in-plane
matrix cracks in the zero deg. plies reached a high density. With
additional cycles, very few new cracks initiated and only slight
lengthening of existing cracks occurred.

After the initial cracking of the 45 deg. plies in the 48 ply
specimens, off-axis matrix cracks continued to develop and grow through-
out the cyclic loading, and in some cases reached the specimen edge.

The damage growth through-the-thickness in the 48 ply specimens was
observed, using edge radiographs, to develop first in the outer plies

and progress toward the center plies. The location and type of damage
through-the-thickness was considered to be not significantly different
in the 47 and 48 ply specimens.

The 47 ply specimens were sectioned to observe the damage inter-
nally. Delaminations were found only at 45/0 interfaces of the outer
plies and, in one instance, between two zero deg. plies. Matrix cracks
were found throughout the thickness in double zero deg. plies and single
45 deg. plies. The matrix cracks were in a more uniform pattern across
the width in the center plies than in the outer plies. Delaminations
and matrix cracks formed links running through-the-thickness in the
outer plies.

Fiber damage in the zero deg. plies of the 47 ply specimen was
observed in the longitudinal sections made beside the hole. Longi-
tudinal compressive loading of the notched laminate produces a triaxial
state of stress near the hole. In addition, the stress concentration
created by the hole produces large compressive longitudinal normal
stresses in the zero deg. fibers. It appeared that the fibers collapsed
locally, evidenced by a fiber shear pattern, i.e., rotation of the fiber
ends along the damage surface.

The 42 ply specimens did not develop the severe amounts of damage
during cyclic loading that were observed in the 47 and 48 ply specimens.
Longitudinal and off-axis matrix cracks developed early in the cyclic
loading at the top, bottom and sides of the hole. As cycling continued,
additional matrix cracks developed in the same regions. The matrix

cracks gradually increased in length. Off-axis matrix cracks did not reach the specimen edge, as observed in the 48 ply specimens.

The through-the-thickness damage of the 42 ply specimens, observed in the edge radiographs and sectioned specimens, was confined to the middle plies. The sectioned surfaces showed matrix cracking in the ten middle plies. Matrix cracks ran through neighboring zero deg. plies and in some instances ran partially into the 22.5 deg. plies. Matrix cracks constrained in the 22.5 deg. plies were also observed. Delaminations observed in the flat radiographs could not be located in the sectioned surfaces.

To interpret the damage observed during the cyclic loading it is helpful to mention some qualitative descriptions of compressive damage and influences of damage formation, location and growth. Agarwal and Broutman [19] have listed failure modes for composite laminates subjected to compressive load as: (1) transverse tensile failure, (2) fiber microbuckling (a) with matrix still elastic, (b) preceded by matrix yielding, and (c) preceded by constituents debonding, and (3) shear failure.

When the fibers of the laminate are longitudinally loaded in compression the Poisson effect produces large tensile strains in the matrix (perpendicular to the fibers). As these strains exceed the ultimate tensile strain of the matrix, cracks develop near the fiber-matrix interface. Matrix cracks may also promote local fiber microbuckling. Laminates having low fiber volume fractions can experience fiber microbuckling during elastic straining of the matrix or upon matrix yielding,

prior to cracking. Fiber microbuckling can cause additional matrix cracking or shear failure of the fibers.

The initial matrix cracks seen in the 42, 47, and 48 ply laminates after a very few loading cycles were the result of fiber overload causing transverse tensile failure of the matrix in the zero deg. plies and a combination of transverse tensile and shear failure of the matrix in the off-axis plies. As these matrix cracks grew, and others formed nearby, the in-plane and interlaminar stresses were redistributed locally causing a combination of fiber microbuckling and further matrix cracking. The onset of fiber microbuckling also caused additional shearing of the matrix and, observed in one instance, fiber shear failure.

The damage modes that have been reported here, and which influence the macroscopic behavior of the laminates, are intralaminar matrix cracking and interlaminar delaminations. Several specific points can be made about the local stress field around the hole, the laminate stacking sequence, and interlaminar stresses to explain the observed damage mechanisms.

For the notched laminates used in this investigation, several factors influence the stress field, which in turn, governs the damage development. The center hole in the specimens is both a stress concentrator and a free edge. Interlaminar stresses develop from the free edge and from the large stress gradients in the region of the stress concentration. These interlaminar stresses produce delaminations in the vicinity of the hole. Also, in the vicinity of the hole is a strong

triaxial stress field. The triaxiality of the stress field produces a large amount of stress redistribution as damage develops in the matrix.

Three points about the stacking sequences of the two laminates can be noted to help understand the difference in fatigue response of the laminates. First, there is less grouping of like plies, specifically zero and 90 deg. plies, in the 42 ply laminate than in the 48 ply laminate. The poorly defined interface between two like plies does not arrest matrix cracks. However, a matrix crack in a single ply constrained on both sides by plies of different orientation will not grow directly into the adjacent plies. Usually, the interface between plies of dissimilar orientation and the different stress states in the adjacent plies either divert the matrix crack or arrest it.

Second, the 42 ply laminate contains a higher percentage of off-axis plies than the 48 ply laminate and, third, the distribution of the ply orientations in the 42 ply laminate is more uniform than in the 48 ply laminate. In addition to the 0, 45, and 90 deg. plies which make up the 48 ply laminate, the 42 ply laminate has a high percentage of 22.5 and 67.5 deg. plies. The combined effect of a higher percentage and more uniform orientation of off-axis plies in the 42 ply laminate is a more fatigue resistant laminate, although the lower percentage of zero deg. plies produces a laminate with less static compressive strength. The off-axis plies are effective in restricting the growth of cracks in the zero deg. plies and in preventing the spread of delamination between plies. Similar observations for $[90,0]_s$ and $[\pm45,0]_s$ graphite epoxy laminates with defects in the zero deg. plies have been reported for tension-tension fatigue [20].

Additional comparison of the two laminates can be made using the finite element analysis of Ratwani and Kan, described in section 3.4. The interlaminar stresses were calculated for the 48 ply laminate and a 42 ply laminate very similar to the one used in this investigation. The through-the-thickness ranges of maximum interlaminar shear stresses τ_{rz} and $\tau_{\theta z}$ at ply interfaces, normalized with respect to the applied stress, for the 42 ply laminate are greater than the corresponding ranges for the 48 ply laminate. Although matrix cracks develop in both laminates, the interlaminar stresses in the 42 ply laminate at 26 ksi loading and in the 48 ply laminate at 30 ksi loading are not great enough to produce large delaminations. Significant delaminations develop in the 48 ply laminate only at applied cyclic stresses much greater than the static strength of the 42 ply laminate. Thus, the apparent fatigue resistance of the 42 ply laminate is due to low interlaminar stresses even when the applied compressive stress is nearly equal to the compressive strength. These observations support the results of other work by Ratwani and Kan [13] who correlated the compressive fatigue life of laminates with interlaminar stresses.

V CONCLUSIONS

The conclusions of this work are grouped by category and listed below. Knowledge gained about the response of the type A (47 and 48 ply) and type B (42 ply) notched graphite epoxy composite laminates to compressive loading and the Nondestructive Inspection (NDI) and other methods used in detecting damage are presented.

1. Mechanical Behavior

   - The differences in the static properties of the 47 ply laminate (missing a zero deg. ply) and the 48 ply laminate were small.
   - The compressive strengths of the 47 and 48 ply laminates are greater than that of the 42 ply laminate due to the greater percentage of zero deg. plies in the type A laminates.
   - Type A and type B notched laminates have a fatigue limit for failure under compression-compression fatigue at R=10 and 10 Hz. The fatigue limits, or threshold compressive stresses, are 26 ksi for the 42 ply laminate and 40 ksi for the 47 and 48 ply laminates. The initial quasi-static strains (average values), recorded from the farfield strain gage, corresponding to these fatigue limits are 3900 $\mu\varepsilon$ and 4300 $\mu\varepsilon$, respectively. However, the tests reported in this study were run in load control, and the strains corresponding to the threshold compressive stresses changed during the tests due to fatigue damage.
   - At the high stress level, several 48 ply specimens failed early in fatigue. However, some 47 and 48 ply specimens failed at 10^6 cycles and other specimens of both types survived 10^6 cycles.

It is not possible to state with complete certainty whether the apparent longer fatigue life of the 47 ply specimens is due to the altered stacking sequence or is due to panel-to-panel variations and statistical scatter in the data.

• In nearly all measured cases, the residual compressive strength of the 42, 47, and 48 ply laminates was equal to, or greater than, the virgin static compressive strength. Cyclic loading of the 48 ply laminate at the fatigue threshold did cause a reduction in compressive strength.

2. Damage Mechanisms

• Damage in both laminate types consists of matrix cracking and delaminations, which develop early in the cyclic loading history. Much greater amounts of damage develop in the 47 and 48 ply laminates than in the 42 ply laminate.

• The apparent fatigue resistance of the 42 ply laminate can be explained (in part) by considering the interlaminar stresses. The interlaminar stresses in the 42 ply laminate, when the applied compressive stress is nearly equal to the compressive strength, are relatively low compared to the interlaminar stresses in the 48 ply laminate.

• Large delaminations develop in the 47 and 48 ply laminates at the medium and high (threshold) stress levels. Sectioning of the 47 ply laminate revealed these delaminations occur in the 45/0 ply interfaces closest to the surface.

- Small delaminations develop in the 42 ply laminates at the 24 and 26 (threshold) ksi stress levels.

- Matrix cracks in the zero deg. plies of the 48 ply laminate occur early in the loading history and increase in density until the hole region is heavily damaged. These cracks are confined to the region around the hole. Matrix cracks in the 45 deg. plies continue to increase in density throughout the loading history and grow outside of the heavily damaged region around the hole.

- Matrix cracks and large delaminations develop asymmetrically about the hole in the 47 ply laminate.

- The growth of damage in thick laminates has a three dimensional nature. Through-the-thickness damage growth was observed in both laminate types. Matrix cracks in the 48 ply laminate developed in the outer plies (mostly in the double zero deg. plies) early in the loading history, and progressed toward the center of the laminate. Matrix cracks in the 42 ply laminate initiated early in the center region and remained almost entirely in the center plies.

3. X-ray Radiography

- X-ray radiographs made using TBE, an enhancing agent, provide sharp detail of the damage in the notched laminates. X-ray radiography was the primary NDI technique used for observing damage in this investigation. Ultrasonic C-scans and replication of sectioned laminates were used to verify the extent of the damage observed in the radiographs.

- X-ray radiographs made after the application of TBE to the notched laminate under compressive load reveals more damage than radiographs made with TBE applied to the specimen under no load.

- Damage was observed during sectioning which was not linked to the hole and, therefore, was not penetrated by the TBE and went undetected in the radiographs.

- Radiographs made with the edge of the specimen oriented perpendicular to the X-ray beam, i.e. edge radiographs, shows through-the-thickness damage growth in thick laminates.

4. Ultrasonic C-scan

- C-scanning provided fair damage detail as compared with X-ray radiography. Delaminations and matrix cracked regions were detected in the C-scans.

5. Ultrasonic Attenuation

- Changes in ultrasonic attenuation during fatigue loading correlated qualitatively with the damage seen in the X-ray radiographs.

6. Changes in the contrived transverse modulus, due to changes in the transverse strain range, during axial load controlled cyclic tests, were reliable real-time indicators of fatigue damage growth.

7. Acoustic Emission

- Increases in acoustic emissions during static loading of the 47 and 48 ply specimens showed correlation with gross nonlinearities of the stress-nearfield strain curves.

- Acoustic emission monitoring gives useful real-time information on the occurrence of damage events during monotonic loading of the laminates.

8. Replication and Sectioning

● Sectioning of damaged laminates provided a reliable means of
verifying the type and extent to damage observed. Replication of
sectioned surfaces is a simple method which can be used to record
internal damage.

REFERENCES

1. "AV-8B, A Second Generation V/STOL," _Automotive Engineering_, Vol. 88, No. 1, Jan. 1980, pp. 61-67.

2. R. D. Jamison and N. F. Black, "Predicting the Critical Buckling Load for a Graphite/Epoxy Laminate," _Composites Technology Review_, Vol. 2, No. 2, Spring 1980, pp. 14-16.

3. R. K. Clark and W. B. Lisagor, "Effects of Method of Loading and Specimen Configuration on Compressive Strength of Graphite/Epoxy Composite Materials," NASA Langley Research Center, NASA-TM-81796, April 1980.

4. P. E. Sandorff, J. T. Ryder and K. N. Lauraitis, "Experimental Evaluation of Column Compression Properties of Graphite/Epoxy Composites," _Composites Technology Review_, Vol. 3, No. 1, Spring 1981, pp. 6-16.

5. M. S. Rosenfeld and L. W. Gause, "Compression Fatigue Behavior of Graphite/Epoxy in the Presence of Stress Raisers," _Fatigue of Fibrous Composite Materials_, ASTM STP 723, 1981, pp. 174-196.

6. E. P. Phillips, "Effects of Truncation of a Predominantly Compression Load Spectrum on the Life of a Notched Graphite/Epoxy Laminate," NASA Langley Research Center, NASA-TM-80114, June 1979.

7. C. R. Saff, "Compression Fatigue Life Prediction Methodology for Composite Structures," McDonnell Douglas Corp., St. Louis, MO, NADC-78203-60, June 1980.

8. J. D. Whitcomb, "Experimental and Analytical Study of Fatigue Damage in Notched Graphite/Epoxy Laminates," NASA Langley Research Center, NASA-TM-80121, June 1979.

9. K. N. Lauraitis and P. E. Sandorff, "Effect of Environment on the Compressive Strengths of Laminated Epoxy Matrix Composites," Lockheed-California Co., Burbank, CA, AFML-TR-79-4179, Dec. 1979.

10. J. T. Ryder, "Effect of Load History on Fatigue Life," Lockheed-California Co., Burbank, CA, AFML-TR-80-4044, Dec. 1979.

11. A. S. D. Wang, "Certification of Composite Aircraft Structures Under Impact, Fatigue and Environmental Conditions. Part III--Environmental Effects on Compressive Strength," Drexel University, NADC-78259-60, Jan. 1978.

12. J. T. Ryder and E. K. Walker, "The Effect of Compressive Loading on the Fatigue Lifetime of Graphite/Epoxy Laminates," Lockheed-California Co., Burbank, CA, AFML-TR-79-4128, Oct. 1979.

13. M. M. Ratwani and H. P. Kan, "Compression Fatigue Analysis of Fiber Composites," Northrop Corp., Hawthorne, CA, NADC-78049-60, Sept. 1979.

14. D. T. Hayford and E. G. Henneke, II, "A Model for Correlating Damage and Ultrasonic Attenuation in Composites," ASTM STP 647, 1979, pp. 184-200.

15. T. K. O'Brien and K. L. Reifsnider, "Fatigue Damage Evaluation Through Stiffness Measurements in Boron-Epoxy Laminates," J. of Composite Materials, Vol. 15, Jan. 1981.

16. E. T. Camponeschi and W. W. Stinchcomb, "Stiffness Reduction as an Indicator of Damage in Graphite Epoxy Composites," presented at the Sixth ASTM Composite Materials Testing and Design Conference, Phoenix, AZ, May 1981.

17. M. N. Gibbins and W. W. Stinchcomb, "Fatigue Response of Composite Laminates with Internal Flaws," presented at the Sixth ASTM Composite Materials Testing and Design Conference, Phoenix, AZ, May 1981.

18. M. M. Ratwani and H. P. Kan, "Develop Analytical Techniques for Predicting Compression Fatigue Life and Residual Strength of Composites," Engineering Progress Report No. 1, NADC Contract N62269-80-C-0265, Northrop Corp. Hawthorne, CA, Nov. 1980.

19. B. D. Agarwal and L. J. Broutman, Analysis and Performance of Fiber Composites, John Wiley & Sons, New York, 1980.

20. W. W. Stinchcomb, K. L. Reifsnider, P. Yeung, and J. Masters, "Effect of Ply Constraint on Fatigue Damage Development in Composite Laminates," ASTM STP 723, 1981, pp. 64-84.

Table I Specimen Identification Code

Designation	Description	Location	Example
#-1	47 ply specimen from the first Type A panel.	Not specified.	1-1
#-2	42 ply specimen from the first Type B panel.	Not specified.	1-2
# letter 1	48 ply specimen from the second Type A panel.	#th specimen from subpanel letter.	8C1-8th specimen from subpanel C.
# letter 2	42 ply specimen from the second Type B panel.	#th specimen from subpanel letter.	6A2-6th specimen from subpanel A.

Table II Fatigue Test Stress Levels

Laminate	Level	Minimum Applied Stress, (Ksi)
47 and 48 ply	High	-40
	Medium	-35
	Low	-30
42 ply	Level 1	-16
	Level 2	-21
	Level 3	-24
	Level 4	-26

Table III
TEST MATRIX FOR 42 PLY SPECIMENS

Specimen	Free Length* (in.)	Thickness** (in.)	Slenderness Ratio	Test Type***	Duration (10^3 cycles)
2-1[†]	3.63	0.226	55.6	Static No Failure	---
2-2	3.83	0.193	68.7	Static Failure	---
2-3	3.46	0.205	58.5	Static No Failure	---
2-4[†]	3.45	0.207	57.7	Static No Failure	---
2-5[†]	4.13	0.221	64.7	Static No Failure	---
2-6	3.92	0.221	61.4	Static Failure	---
2-7	3.93	0.222	61.3	Static Failure	---
2-8	3.92	0.222	61.2	Level 1 Fatigue Residual Strength	1020
2-9	3.94	0.222	61.5	Level 2 Fatigue Residual Strength	1004
2-10	3.93	0.211	64.5.	Level 3 Fatigue Residual Strength	1009
2-11	3.93	0.221	61.6	Static Failure	---

Table III continued
TEST MATRIX FOR 42 PLY SPECIMENS

Specimen	Free Length* (in.)	Thickness** (in.)	Slenderness Ratio	Test Type***	Duration (10^3 cycles)
1A2	3.94	0.207	65.9	Level 4 Fatigue Failure	78
1B2	3.94	0.209	65.3	Static Failure	---
10B2	4.14	0.236	60.8	Level 4 Fatigue Residual Strength	1000
1C2	3.94	0.207	65.9	Level 4 Fatigue Sectioned	1000
10C2	4.14	0.237	60.5	Level 4 Fatigue Failure	16
1D2	3.94	0.207	65.9	Level 4 Fatigue Residual Strength	1040
10D2	3.93	0.225	60.5	Level 4 Fatigue Residual Strength	962

* Total length = free length + 1.375 in.

** Half-length thickness

*** Level 1 Fatigue σ_{min} = -16 ksi

Level 2 Fatigue σ_{min} = -21 ksi

Level 3 Fatigue σ_{min} = -24 ksi

Level 4 Fatigue σ_{min} = -26 ksi

Table IV
TEST MATRIX FOR 47 PLY SPECIMENS

Specimen	Free Length* (in.)	Thickness** (in.)	Slenderness Ratio	Test Type***	Duration (10^3 cycles)
1-1	4.13	0.214	66.8	Static Failure	---
1-2†	4.13	0.221	64.7	Static No Failure	---
1-3	4.13	0.228	62.7	High Level Fatigue Failure	377
1-4	4.13	0.229	62.5	High Level Fatigue Failure	40††
1-5	4.13	0.232	61.7	High Level Fatigue Failure	417
1-6	4.10	0.231	61.5	High Level Fatigue Sectioned	400
1-7	4.14	0.236	60.8	Low Level Fatigue	1000
1-8	4.14	0.236	60.8	Low Level Fatigue Residual Strength	1000
1-9	4.14	0.236	60.8	High Level Fatigue Specimen Sectioned	362
1-10	4.15	0.233	61.7	Low Level Fatigue Residual Strength	1000
1-11	3.88	0.225	59.7	Static Failure	---
1-12	4.13	0.231	61.9	Medium Level Fatigue Residual Strength	652
1-13	4.25	0.239	61.6	Medium Level Fatigue Residual Strength	681

Table IV continued
TEST MATRIX FOR 47-PLY SPECIMENS

Specimen	Free Length* (in.)	Thickness** (in.)	Slenderness Ratio	Test Type***	Duration (10^3 cycles)
1-14	4.39	0.243	62.6	Low Level Fatigue Residual Strength	1000
1-15	4.50	0.247	63.1	Static Failure	---

* Total length = Free length + 1.375 in.

** Half-length thickness

*** High Level Fatigue σ_{min} = -40 ksi

     Medium Level Fatigue σ_{min} = -35 ksi

     Low Level Fatigue σ_{min} = -30 ksi

† Unnotched

†† Operator induced failure

Table V
TEST MATRIX FOR 48 PLY SPECIMENS

Specimen	Free Length* (in.)	Thickness (in.)	Slenderness Ratio	Test Type**	Duration (10^3 cycles)
1A1	4.16	0.276	52.2	Static No Failure	--
2A1	4.16	0.298	48.4	High Level Fatigue Failure	80
3A1	4.16	0.295	48.8	Static Failure	--
4A1	4.16	0.295	48.8	Static Failure	--
5A1	4.16	0.295	48.8	Low Level Fatigue No Failure	1700
6A1	4.16	0.295	48.8	High Level Fatigue Residual Strength	400
7A1	4.16	0.296	48.7	Static Failure	--
8A1	4.16	0.298	48.4	High Level Fatigue Failure	50
9A1	4.16	0.295	48.8	Medium Level Fatigue Residual Strength	1000
1B1	4.16	0.284	50.8	Medium Level Fatigue Residual Strength	980
2B1	4.16	0.293	49.2	Medium Level Fatigue Residual Strength	600
3B1	4.16	0.300	48.0	High Level Fatigue Failure	23

Table V continued
TEST MATRIX FOR 48 PLY SPECIMENS

Specimen	Free Length* (in.)	Thickness (in.)	Slenderness Ratio	Test Type**	Duration (10^3 cycles)
4B1	4.16	0.302	47.7	High Level Fatigue Failure	3
5B1	4.16	0.307	46.9	Medium Level Fatigue Residual Strength	600
6B1	4.16	0.310	46.5	Low Level Fatigue Residual Strength	1000
7B1	4.16	0.313	46.0	Medium Level Fatigue Residual Strength	2200
8B1	4.16	0.317	45.4	Medium Level Fatigue Residual Strength	600
9B1	4.15	0.315	45.6	Static No Failure	---
1C1	4.16	0.284	50.7	Medium Level Fatigue Residual Strength	320
9C1	4.15	0.315	45.6	Static No Failure	---
1D1	4.13	0.277	51.6	Static No Failure	---
9D1	4.12	0.294	48.5	Low Level Fatigue Residual Strength	1000

* Total length = free length + 1.375 in.

**
High Level Fatigue σ_{min} = -40 ksi

Medium Level Fatigue σ_{min} = -35 ksi

Low Level Fatigue σ_{min} = -29 ksi

Table VI 42 Ply Static Data

Specimen	Strength	σ_{ULT} (Ksi)	Ultimate Strain, (με)				Change in Longitudinal Modulus, (%)†	
			Farfield		Nearfield		Farfield	Nearfield
			ε_L	ε_T	ε_L	ε_T		
2-6	virgin	-26.7	-4100	+1400	*	*	-12.2	*
2-7	virgin	-26.8	-4250	+1380	*	*	-23.5	*
2-8	residual	-34.2	-5250	+1800	*	*	- 6.1	*
2-9	residual	-33.5	-5100	+1800	**	**	- 2.1	**
2-10	residual	-31.4	-4080	+1400	**	+1770	+ 5.5	**
2-11	virgin	-28.2	-350C	-1080	*	*	+14.3	*
1B2	virgin	-28.5	-6400	+2130	**	**	-36.5	**
10B2	residual	-31.9	-4000	+1310	*	*	+ 2.5	*
1D2	residual	-24.9	*	*	*	*	*	*
10D2	residual	-36.4	-4500	+1580	-12400	+2800	+ 1.1	-50.4

† Percentage change between initial longitudinal modulus and final secant modulus.

* Microbuckling caused strain to decrease.

** Microbuckling caused strain to increase.

72

Table VII - 47 Ply Static Data

Specimen	Strength	σ_{ULT} (Ksi)	Ultimate Strain, $(\mu\epsilon)$ Farfield ϵ_L	Farfield ϵ_T	Nearfield ϵ_L	Nearfield ϵ_T	Change in Longitudinal Modulus, (%)† Farfield	Nearfield
1-1	virgin	-50.2	-5200	+2000	- 8300	+2200	- 6.8	-37.0
1-8	residual	-50.1	---	---	- 9500	+3250	---	-29.4
1-10	residual	-48.1	---	---	-10750	+3550	---	-39.5
1-11	virgin	-42.5	-4000	+1480	*	*	+11.3	*
1-12	residual	-48.8	-4100	+1630	*	*	+18.4	*
1-13	residual	-47.3	-5050	+2000	*	*	0.0	*
1-14	residual	-52.1	-5900	+2700	- 8900	**	- 7.6	-32.6
1-15	virgin	-45.3	-5950	+2630	**	**	-15.1	**

† Percentage change between initial longitudinal modulus and final secant modulus.

* Microbuckling caused strain to decrease.

** Microbuckling caused strain to increase.

Table VIII 48 Ply Static Data

Specimen	Strength	σ_{ULT} (Ksi)	Ultimate Strain, (με)				Change in Longitudinal Modulus, (%)†	
			Farfield		Nearfield			
			ε_L	ε_T	ε_L	ε_T	Farfield	Nearfield
3A1	virgin	-46.1	---	---	-10000	+3500	---	-25.0
4A1	virgin	-50.8	---	---	-10500	+2400	---	-31.0
6A1	residual	-43.4	---	---	-6250	+2430	---	+ 4.0
7A1	virgin	-52.4	---	---	-3000	+4000	---	††
9A1	residual	-47.5	-6300	+2700	-6600	+2200	-4.0	- 4.5
1B1	residual	-53.5	-6650	+2700	-9300	+3650	-4.5	-18.3
2B1	residual	-50.3	-6700	+3150	-9800	+3800	-4.5	-13.7
5B1	residual	-50.0	-5900	+2550	-9500	†††	0.0	-15.8
6B1	residual	-53.0	-6400	+2800	-7200	+2600	-7.0	- 4.6
7B1	residual	-46.7	-5850	+2350	-8000	+3250	-3.4	-13.6
8B1	residual	-47.2	-6100	+2680	-6400	+2530	-5.7	+ 0.0
1C1	residual	-48.6	-6300	+2700	-9200	+3830	-4.0	-20.6
9D1	residual	-47.6	-5900	+2200	-6600	+2300	-4.2	- 3.0

† Percentage change between initial longitudinal modulus and final secant modulus.

†† Specimen slipped in grips.

††† Gage failure.

Table IX   STIFFNESS MONITORING DATA

Specimen	Laminate Type (plies)	Fatigue Level*	Duration (10^3 cycles)	Data**	Change in Secant Modulus, (%) Static	Dynamic
9D1	48	Low	1000	E_{LT}	--	+ 3
1B1	48	Medium	980	E_{LT}	-18	- 5
2B1	48	Medium	600	E_{LT}	-17	-15
1-8	47	Low	1000	E_L	--	0
9A1	48	Medium	1000	E_L	--	+ 7
1-9	47	High	362	E_L	--	- 4
1D2	42	4	1040	E_{LT}	-14	-25
10D2	42	4	962	E_L	- 2	+ 3

* The corresponding stresses are listed in Table II.

** E_L = longitudinal modulus.

$E_{LT} = \sigma_L/\varepsilon_T$

Table X
Sectioned Dimensions of Specimens 1-6, 1-9, and 1C2

Specimen 1-6 (47 ply)

Section	Distance from hole edge to cut surface (in.)
Transverse	
1	0.220
2	0.085
3	0.063
4	0.042
Longitudinal	
1'	0.171
2'	0.116
3'	0.055
4'	0.029

Specimen 1-9 (47 ply)

Transverse	
1	0.204
2	0.071
3	0.045
4	0.011
Longitudinal	
(none)	

Specimen 1C2 (42 ply)

Transverse	
1	0.080
2	0.040
Longitudinal	
1'	0.095
2'	0.039
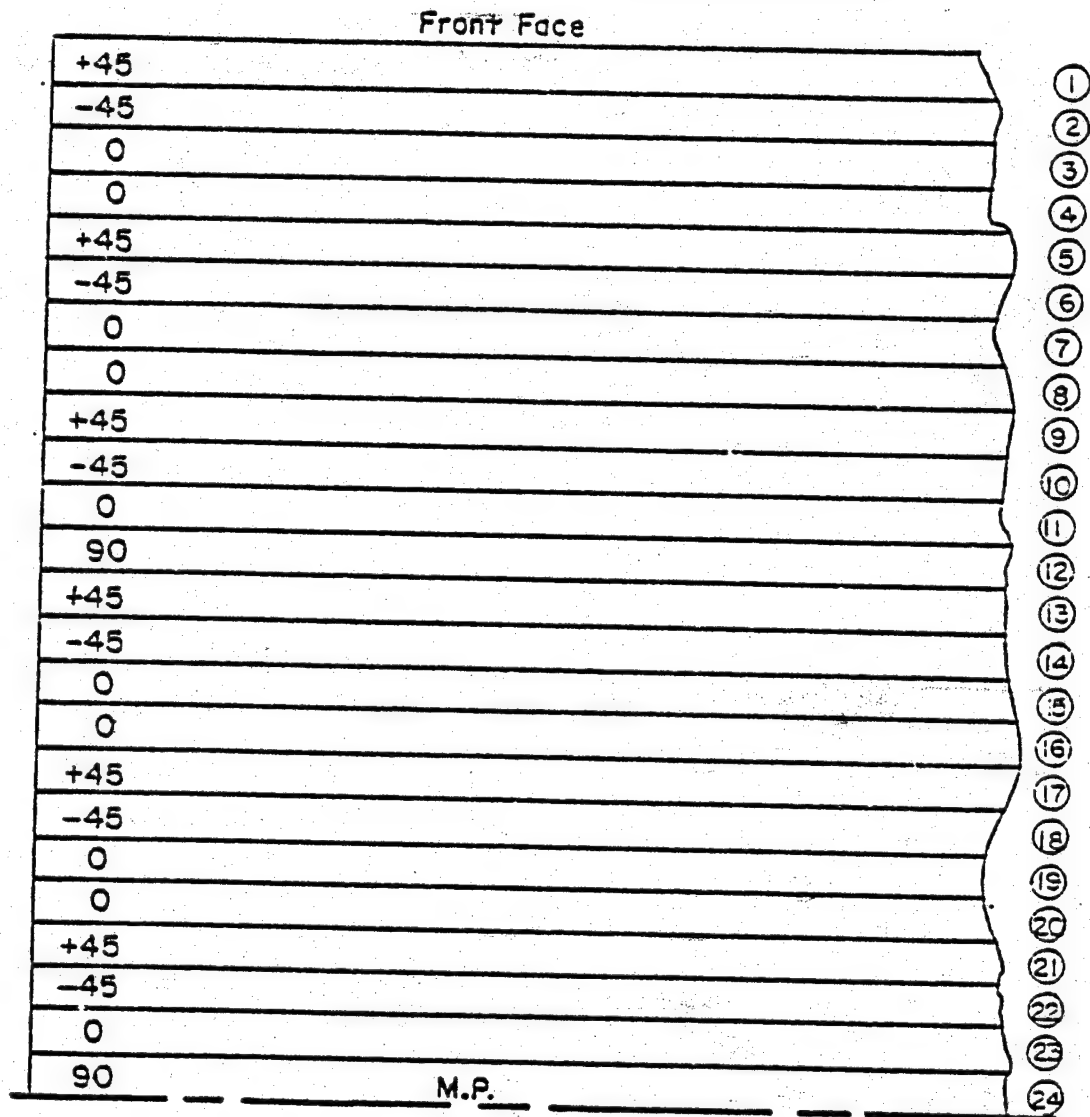
48 Ply Laminate

$$(\pm 45, 0_2, \pm 45, 0_2, \pm 45, 0, 90)_{2s}$$

Figure 1. Schematic of the 48 ply laminate.

Front Face

+45	①
−45	②
+90	③
−45	④
+22.5	⑤
−67.5	⑥
−22.5	⑦
+67.5	⑧
+45	⑨
−45	⑩
+67.5	⑪
+22.5	⑫
−67.5	⑬
−22.5	⑭
+67.5	⑮
−67.5	⑯
+22.5	⑰
−22.5	⑱
0	⑲
0	⑳
+22.5 M.P.	㉑

42 Ply Laminate

$$(\pm 45, 90, -45, +22.5, -67.5, -22.5, +67.5, \pm 45, +67.5,$$
$$+22.5, -67.5, -22.5, \pm 67.5 \pm 22.5, 0_2, +22.5)_s$$

Figure 2. Schematic of the 42 ply laminate.

48 Ply Specimen Sheet
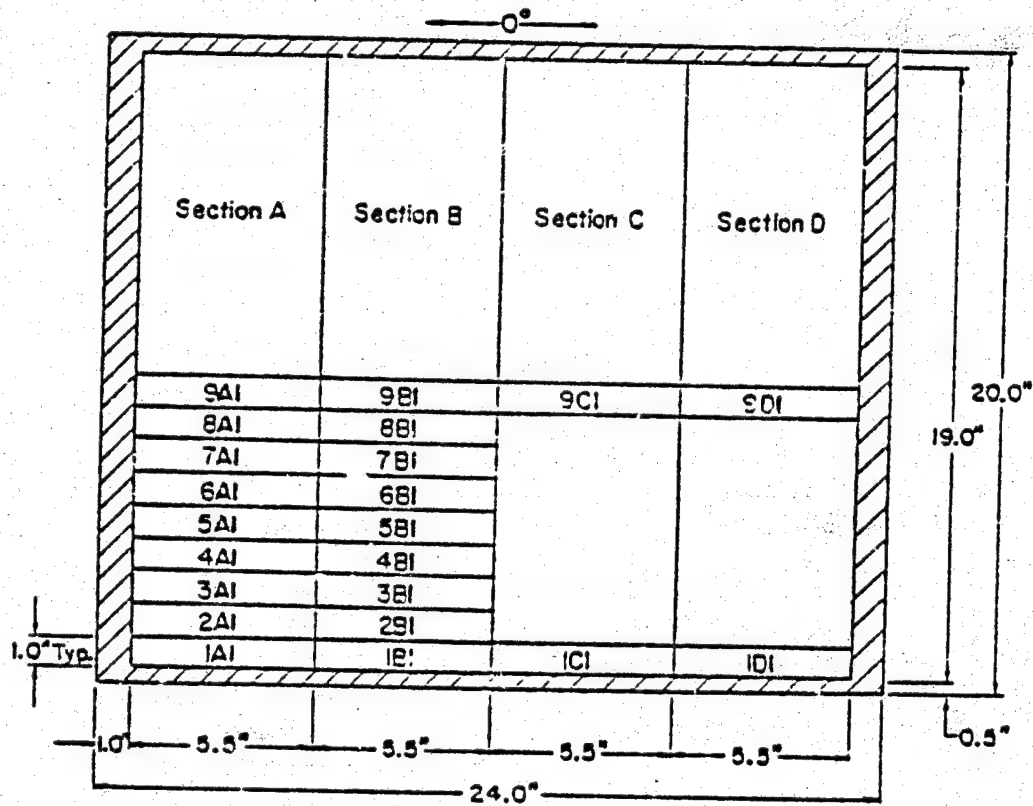
Figure 3. Location of specimens in the 48 ply panel.
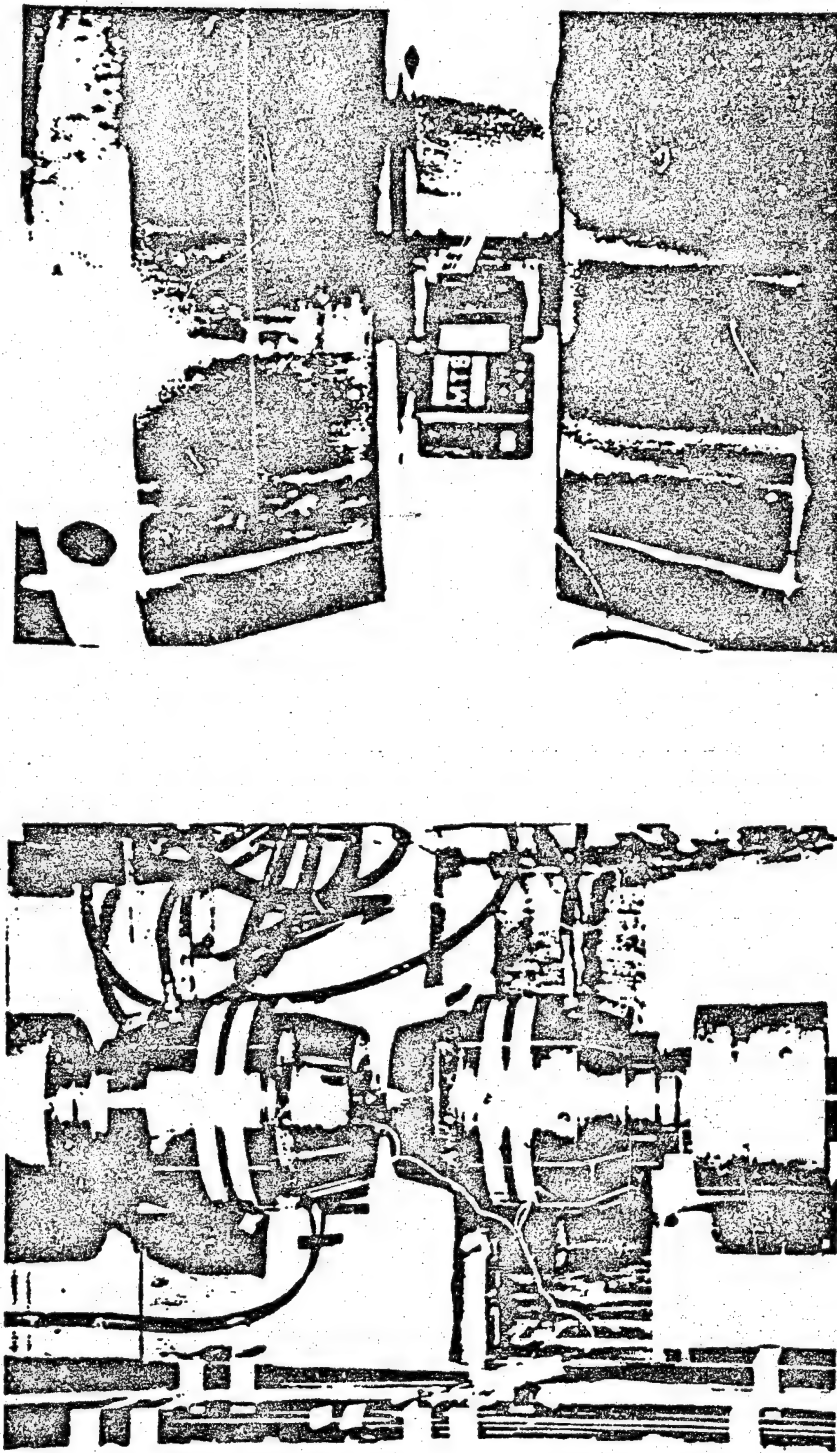
Figure 4. MTS load frame (left) and hydraulic grips with longitudinally mounted clip-gage attached to a specimen (right).

Housing

Gripped Portion
of Specimen

Alignment Plate

Specimen

$1\frac{1}{2}''$

$\frac{7}{16}''$

$17\frac{1}{16}''$

$1''$

FRONT VIEW
(Grips Not Shown)

Grips

$\frac{1}{8}''$

SIDE VIEW
(Housing Not Shown)
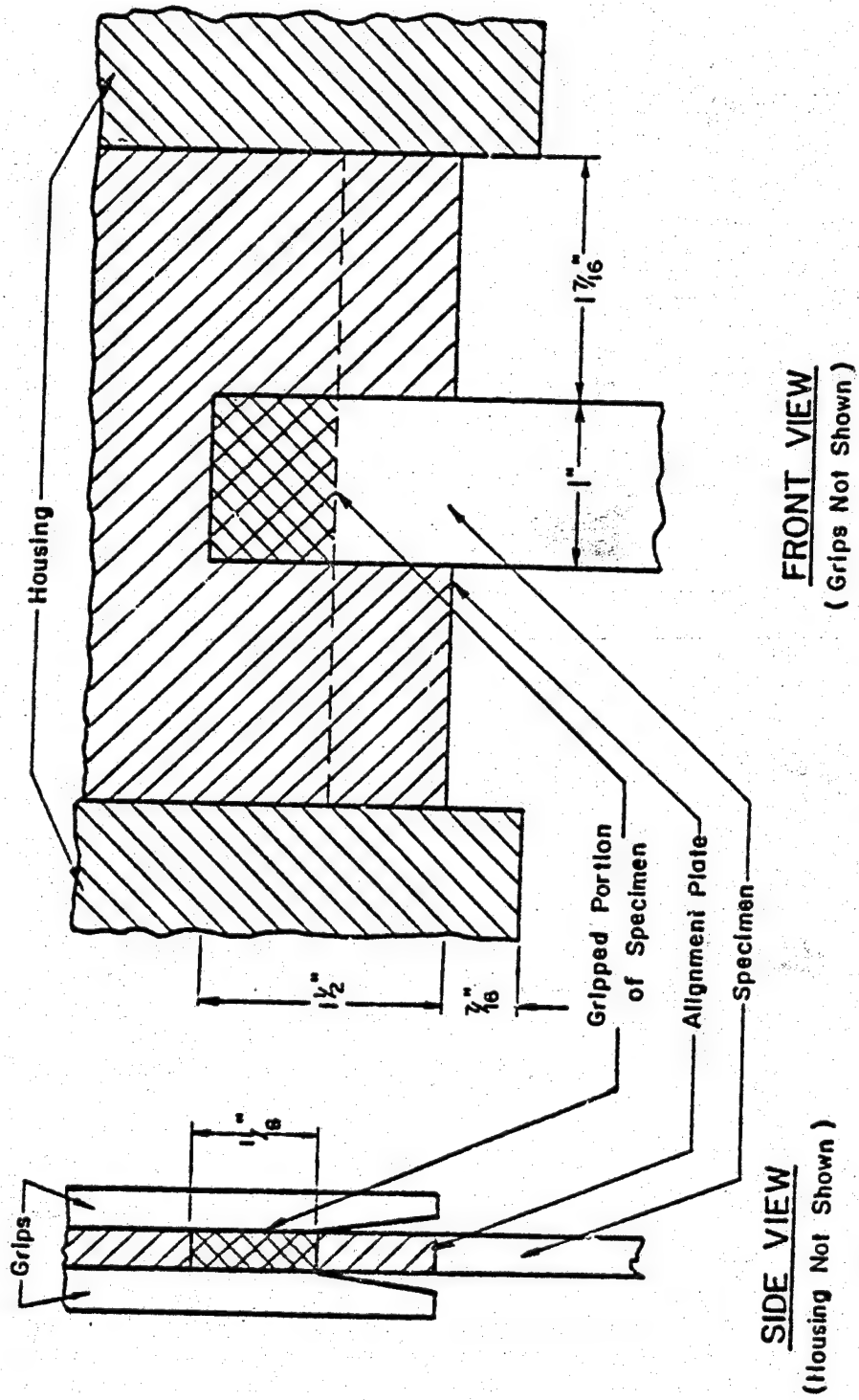
Figure 5.   Alignment and gripping arrangement for compression tests.
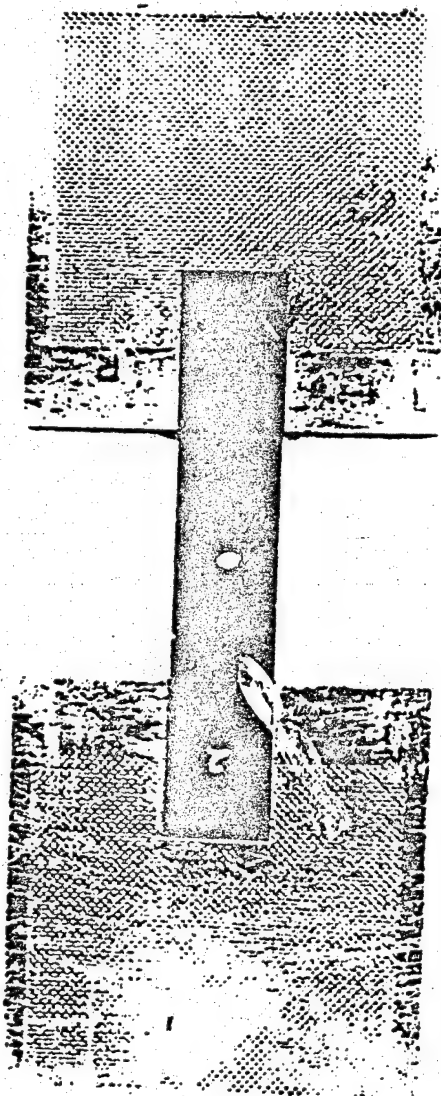
Figure 6. Alignment fixture used in mounting specimen in grips for compression testing.
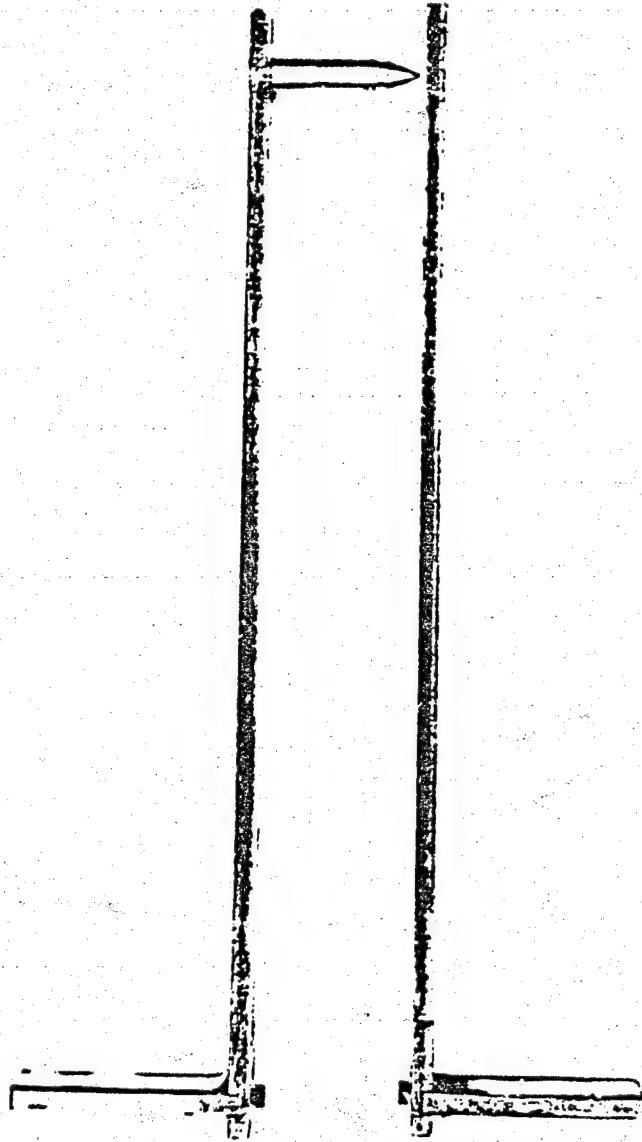
Figure 7. Alignment bars used for rotary positioning of grips.
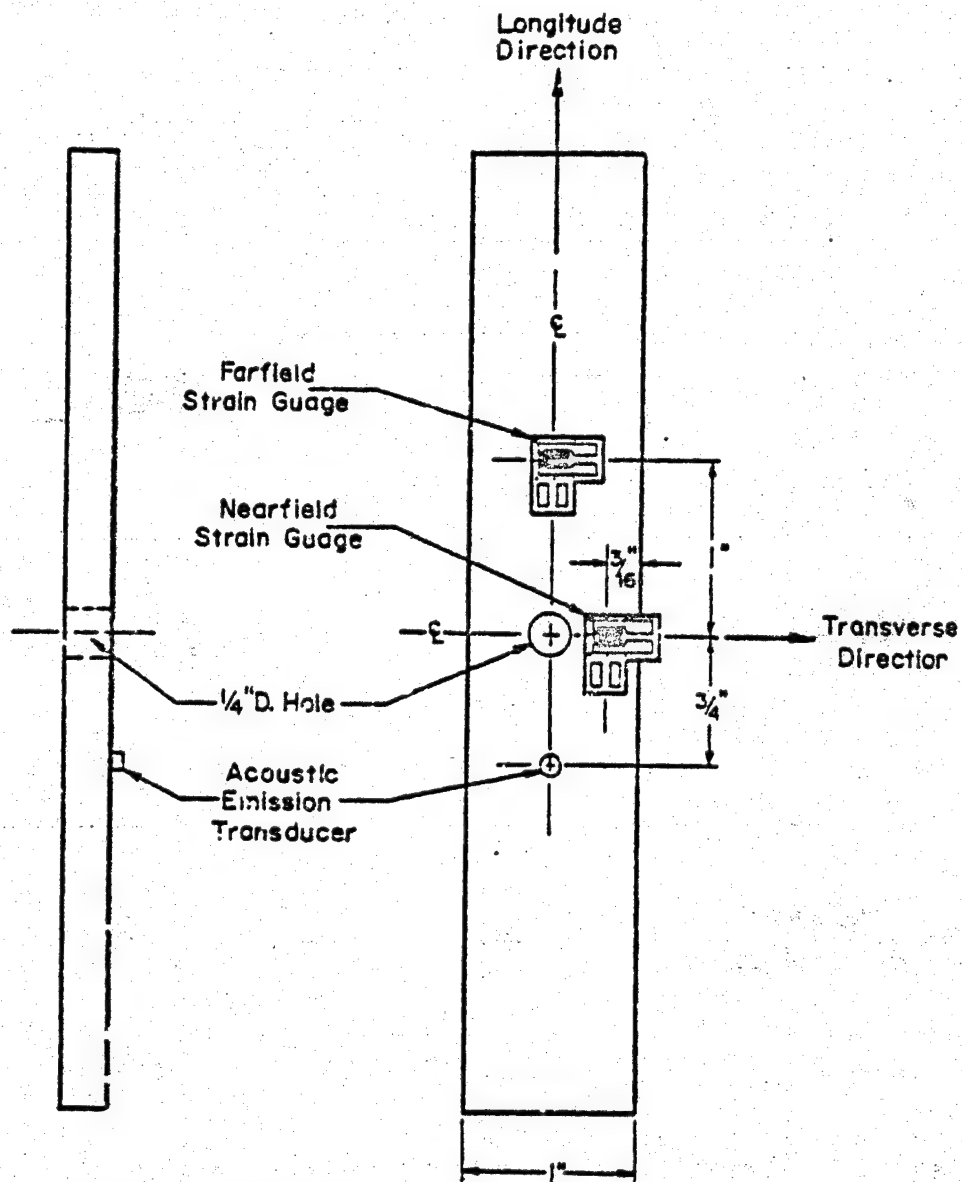
Figure 8. Instrumented specimen for static testing.

84

SCHEMATIC SHOWING DAMAGE TYPES
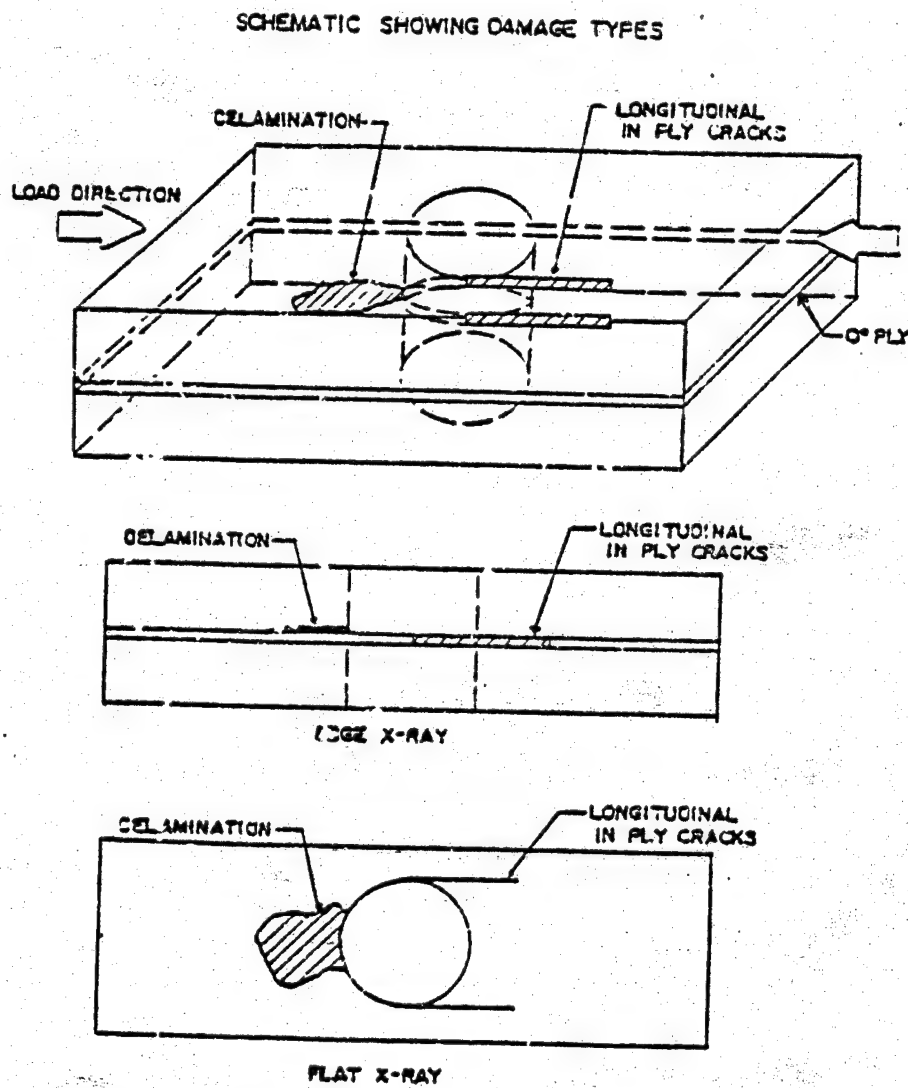
Figure 9. Schematic of damage modes revealed by X-rays
with TBE enhancement.

Figure 10. Calibration specimen used with ultrasonic C-scan apparatus.
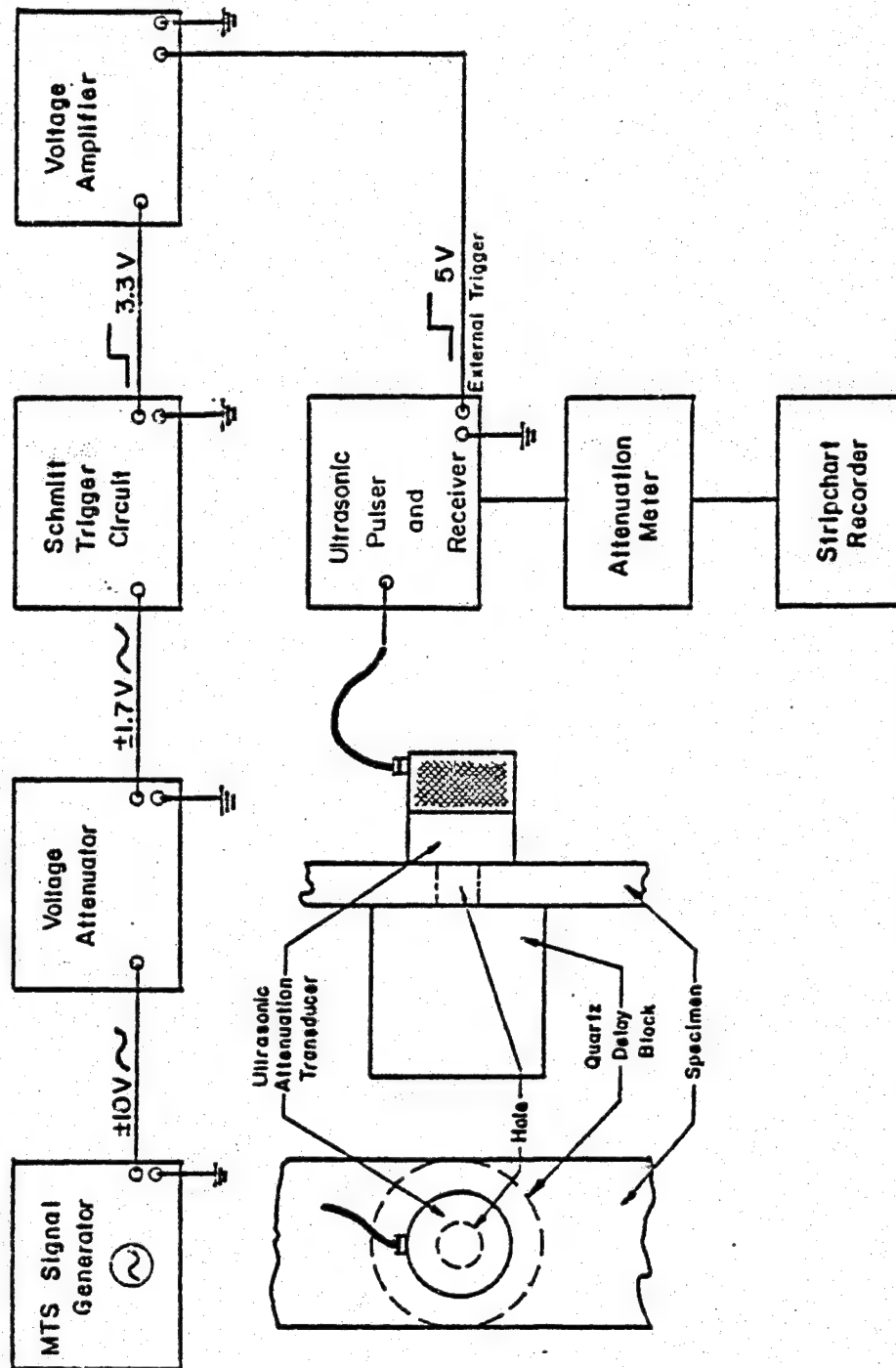
Figure 11. Schematic of system used to record ultrasonic attenuation during a fatigue test.
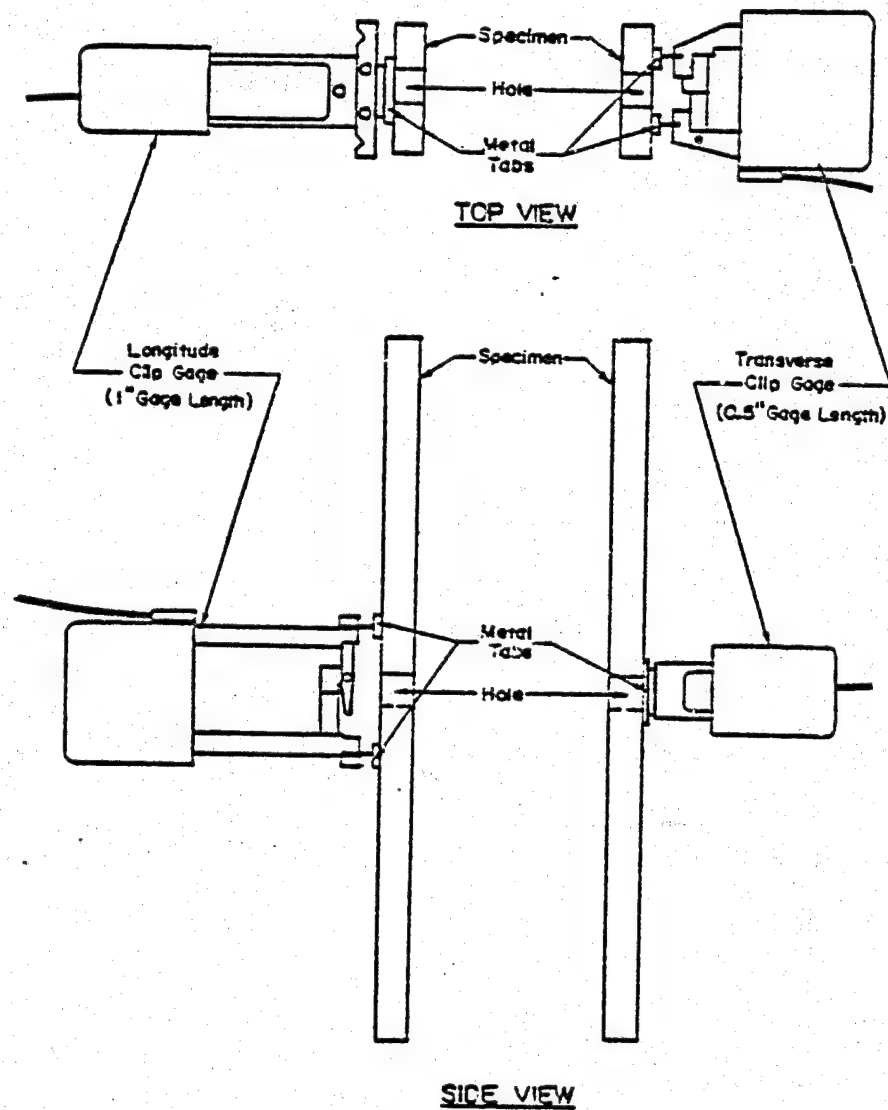
Figure 12A. Specimens instrumented to measure longitudinal and transverse strains during fatigue tests.
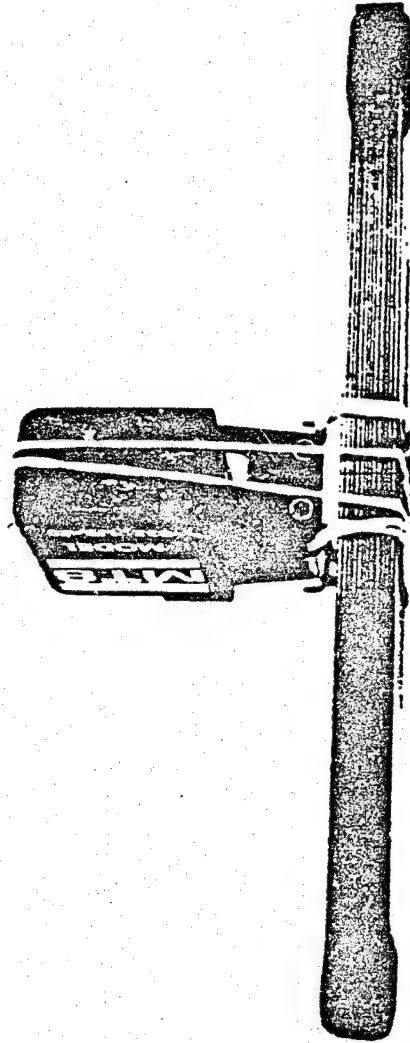
Figure 12B. Transverse extensometer mounted on a 48 ply specimen.
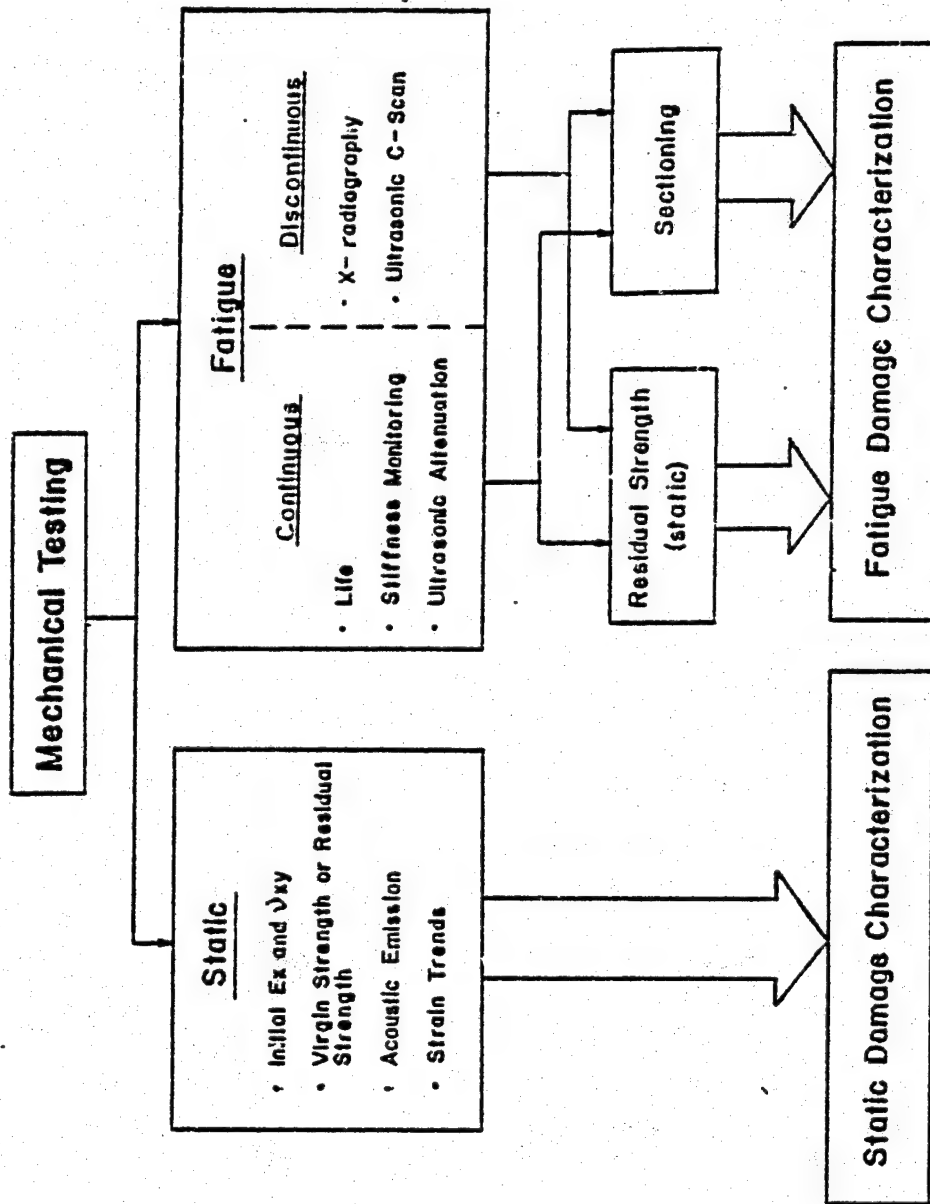
Figure 13. Flow chart of the experimental program.

SPECIMEN 1-1 (47 PLY)

SPECIMEN 1-1 (47 PLY)
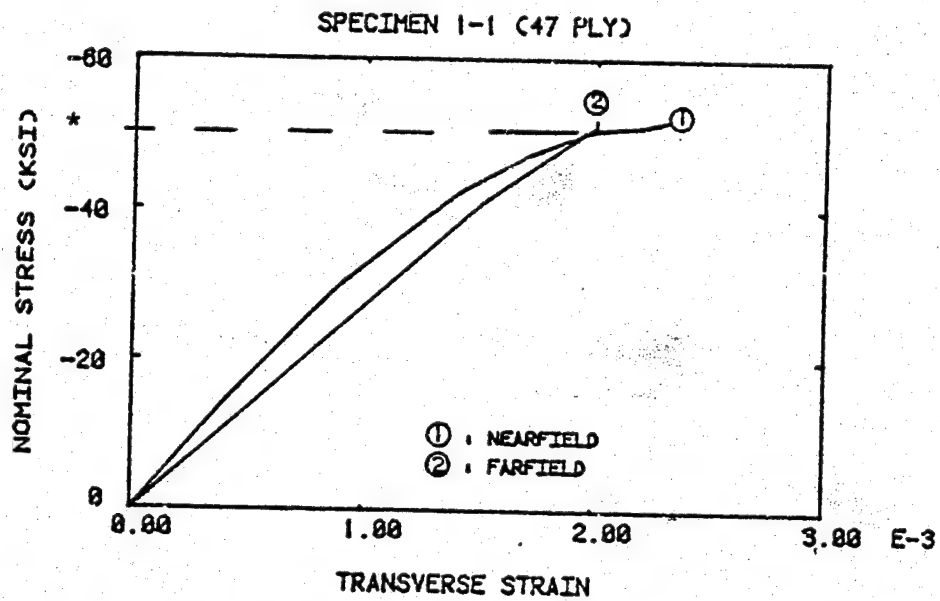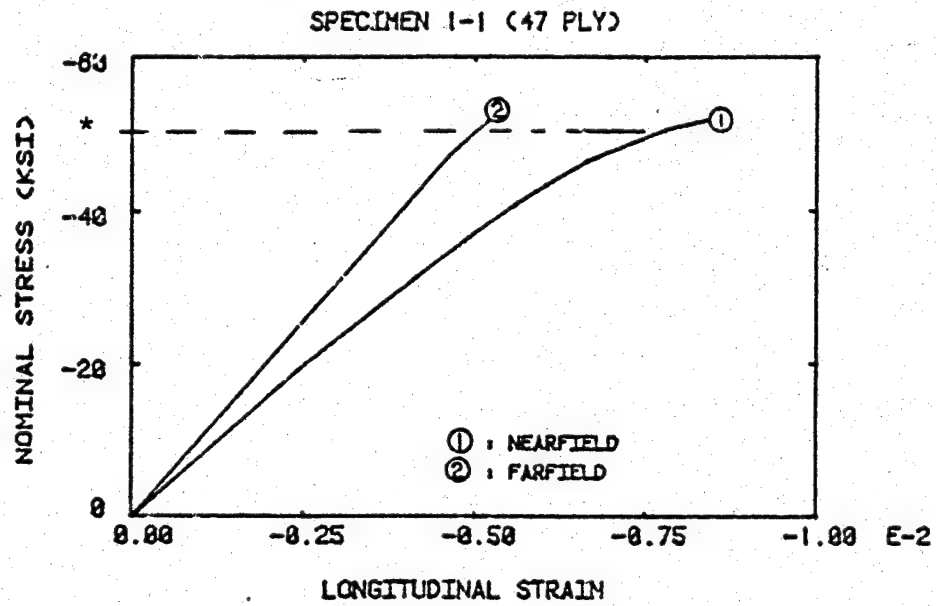
Figure 14. Nominal stress vs. longitudinal and transverse strain, nearfield and farfield locations, for specimen 1-1 (asterisk corresponding to a nominal stress of 47 ksi is also shown in Fig. 16).
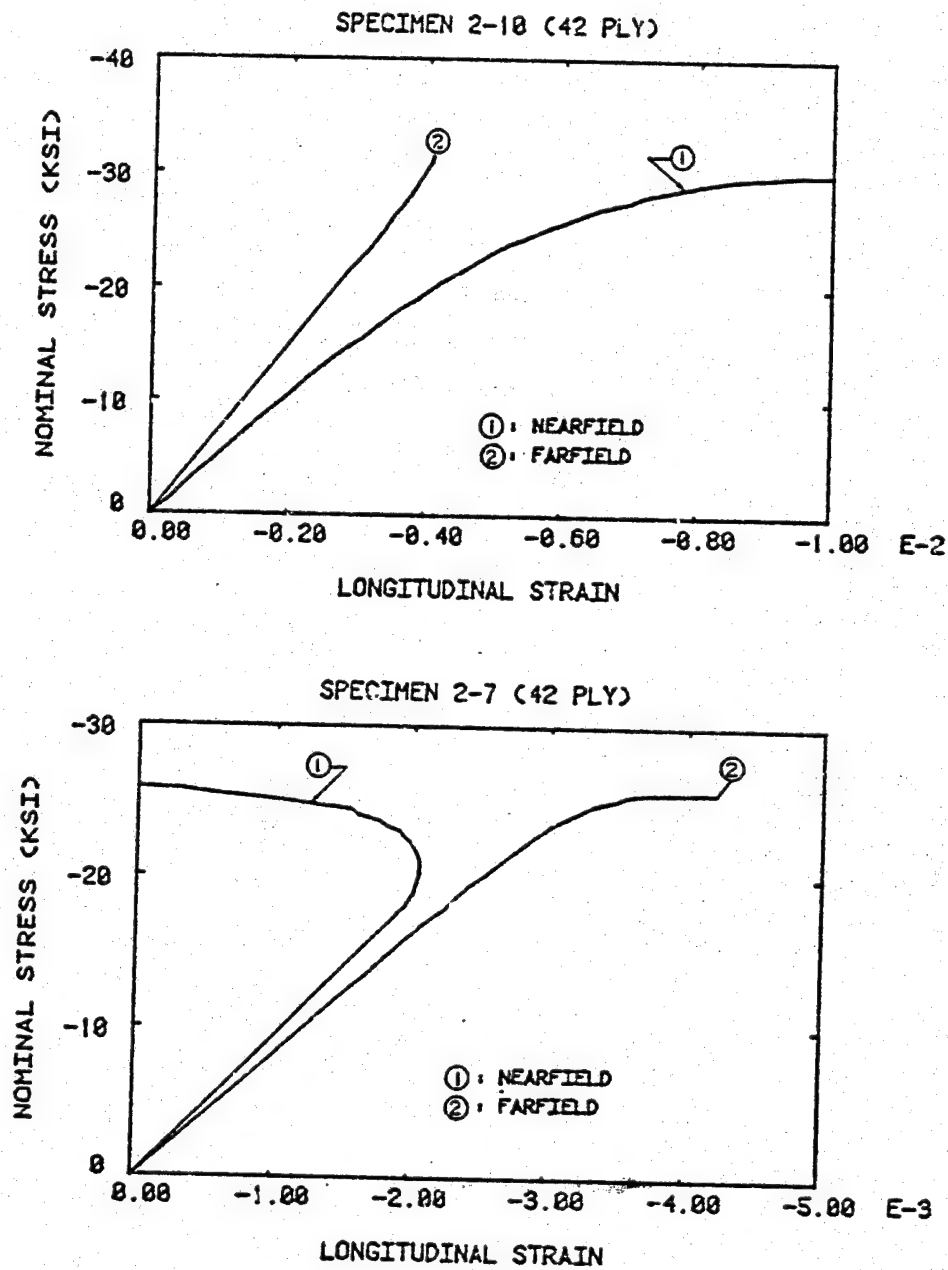
Figure 15. Nominal stress vs. nearfield and farfield longitudinal strain for specimens 2-7 and 2-10.
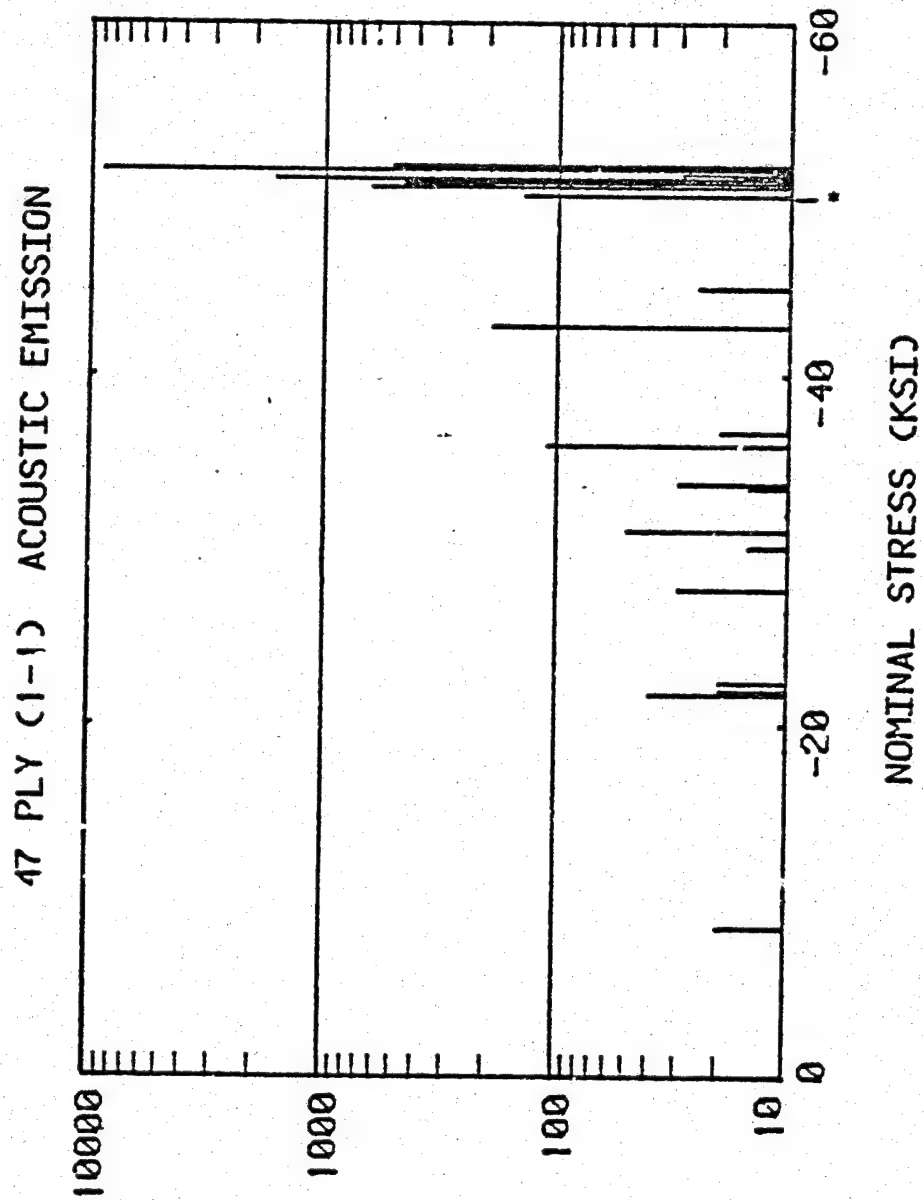
Figure 16. Acoustic emission vs. nominal stress for specimen 1-1.
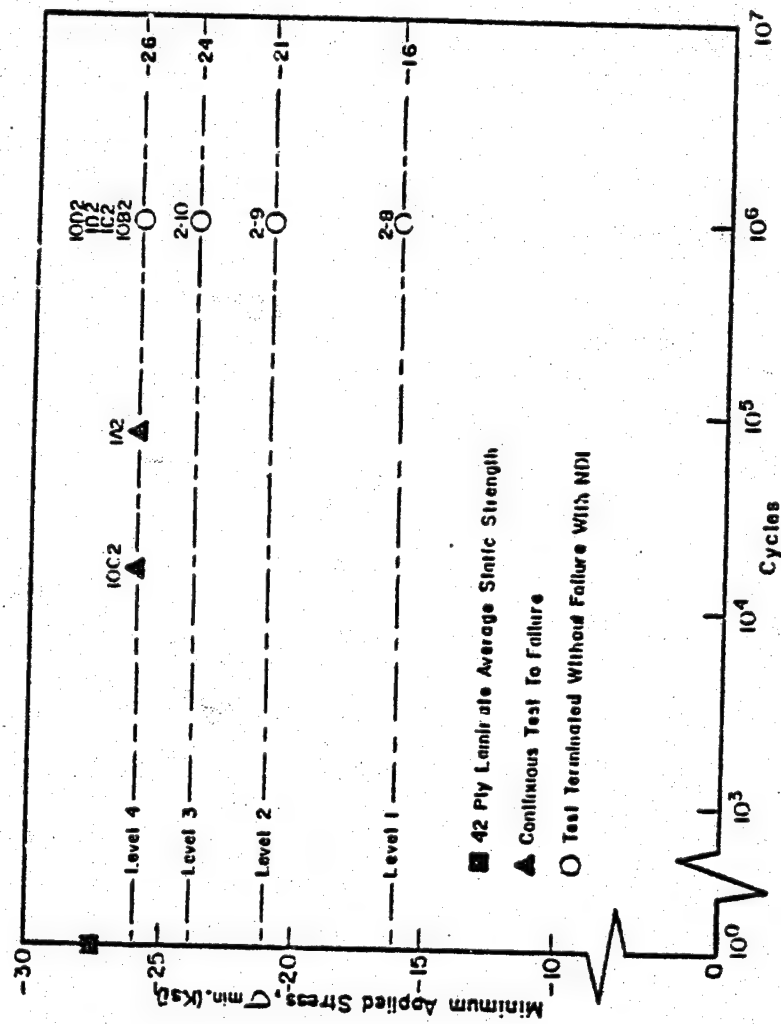
Figure 17. S-N data for 42 ply laminate.
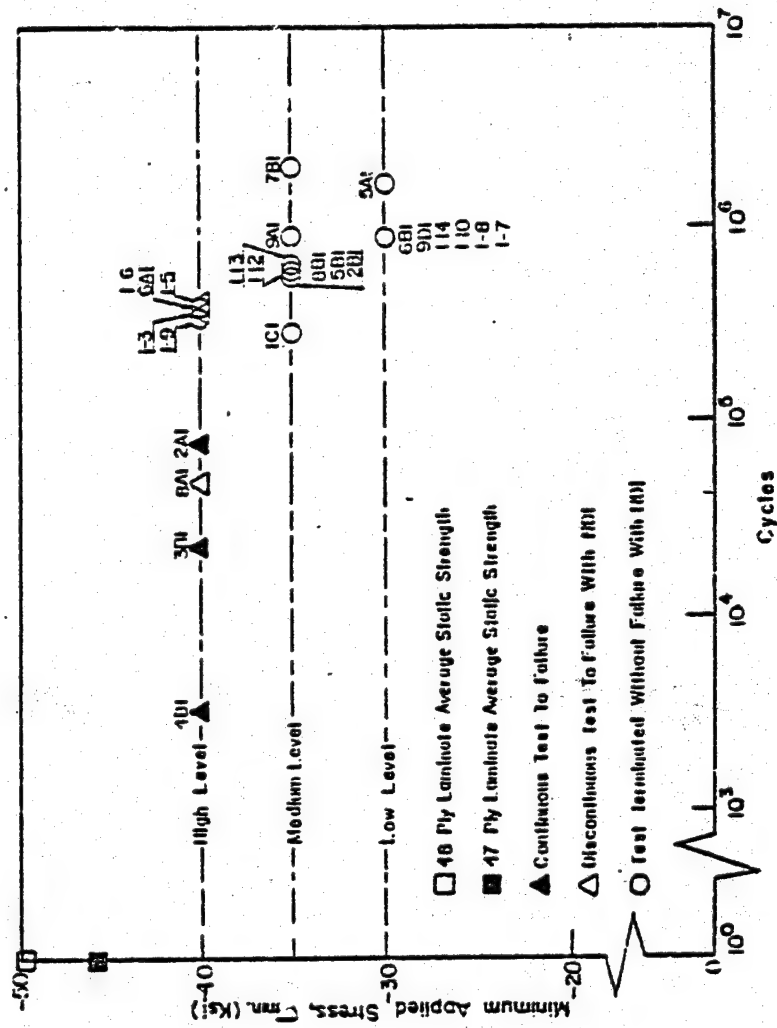
Figure 18. S-N data for 47 and 48 ply laminates.
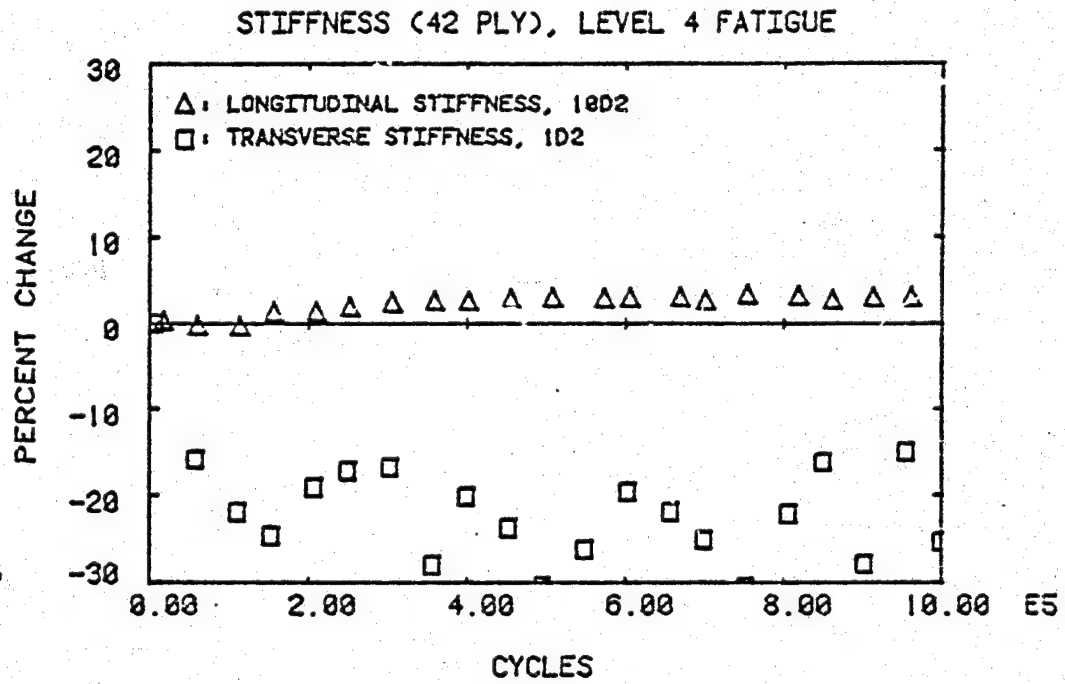
Figure 19. Stiffness change vs. cycles for 42 ply specimens at level 4 fatigue.

LONGITUDINAL STIFFNESS (48 & 47 PLY)

TRANSVERSE STIFFNESS (48 PLY)
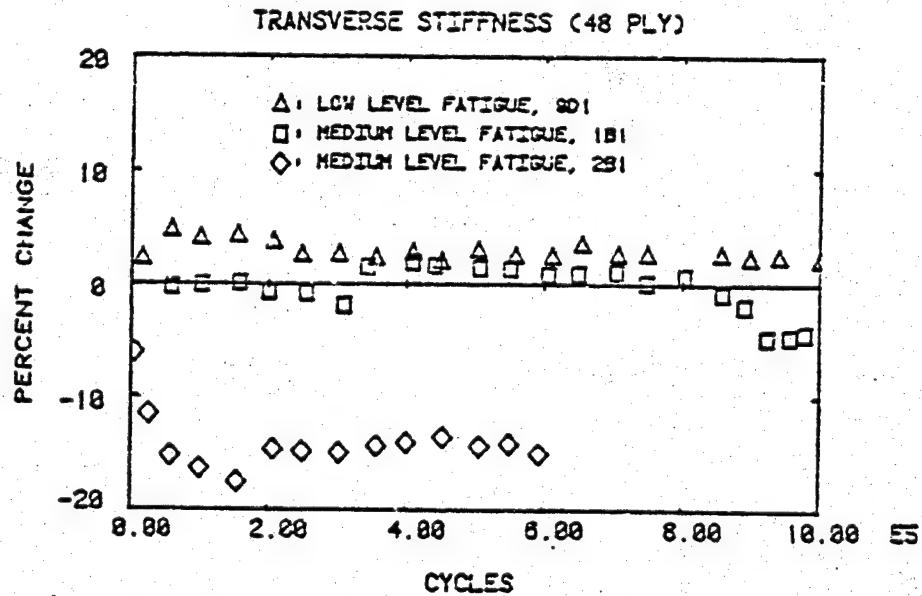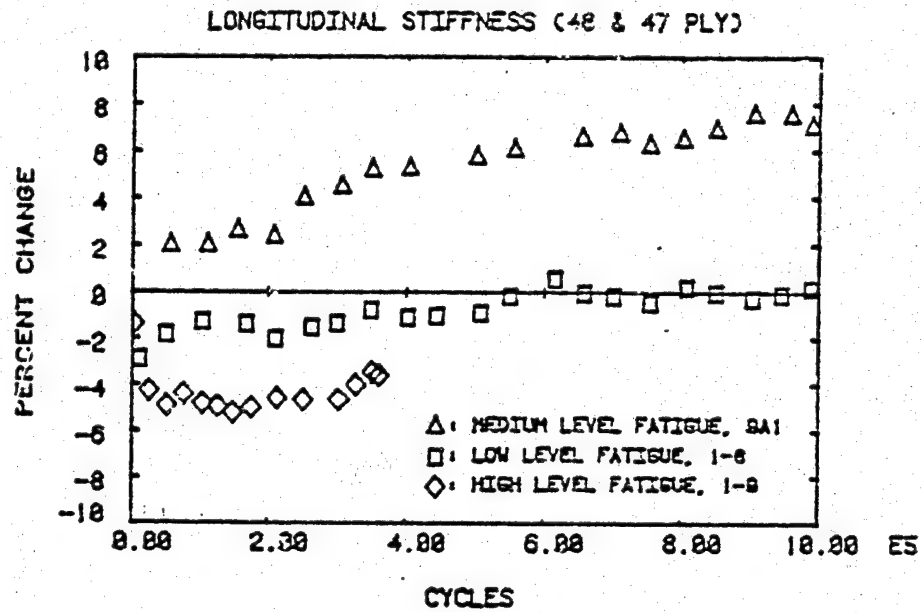
Figure 20. Stiffness change vs. cycles for 47 and 48 ply specimens at several stress levels.

Figure 21.   Bar plots of residual strength data for the 42 ply laminate.
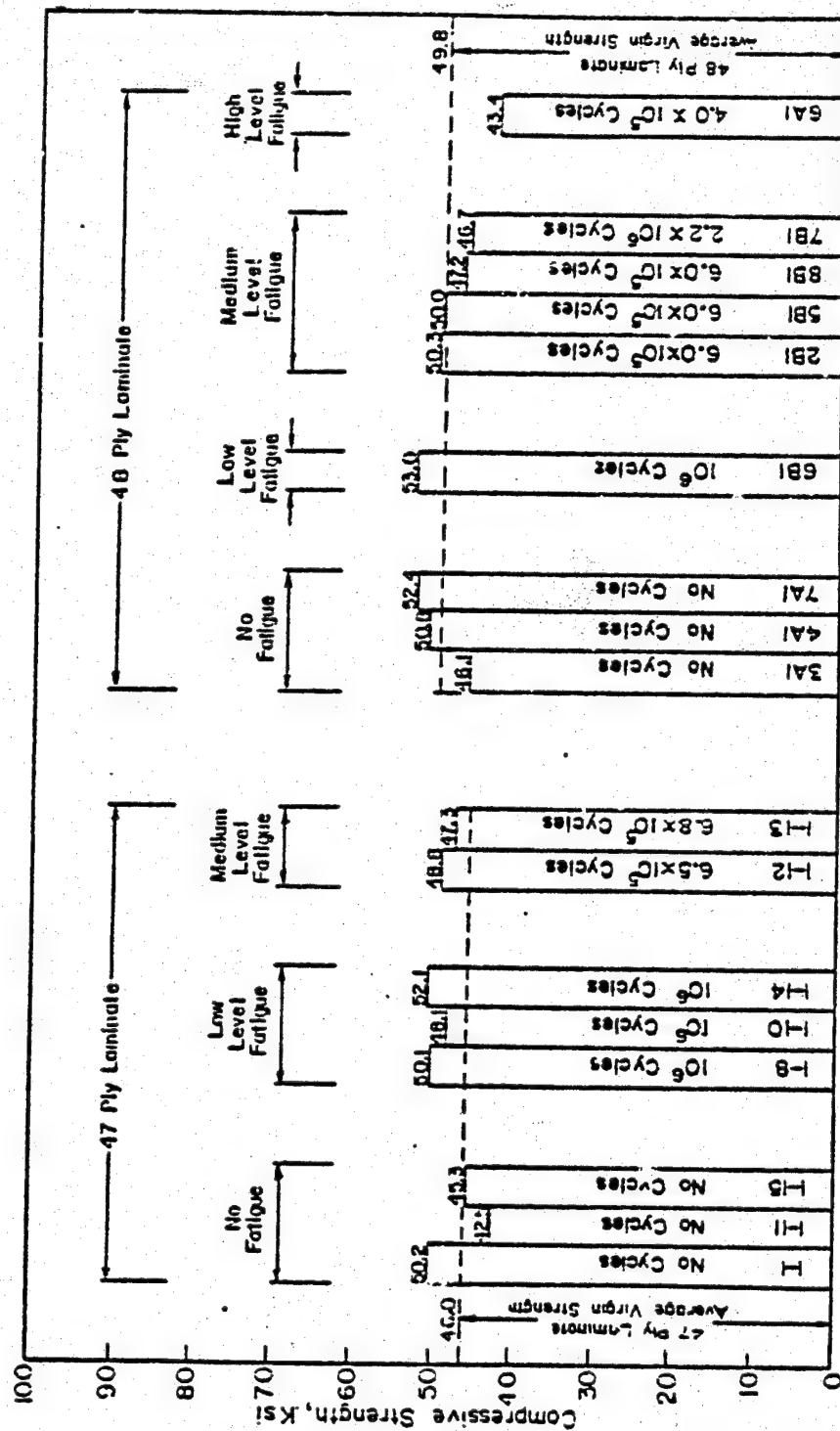
Figure 22. Bar plots of residual strength data for the 47 and 48 ply laminates.

IOB2
26KSI (4th) STRESS LEVEL
IM cycles

2-IO
24KSI (3rd) STRESS LEVEL
IM cycles

←———— LOADING DIRECTION ————→
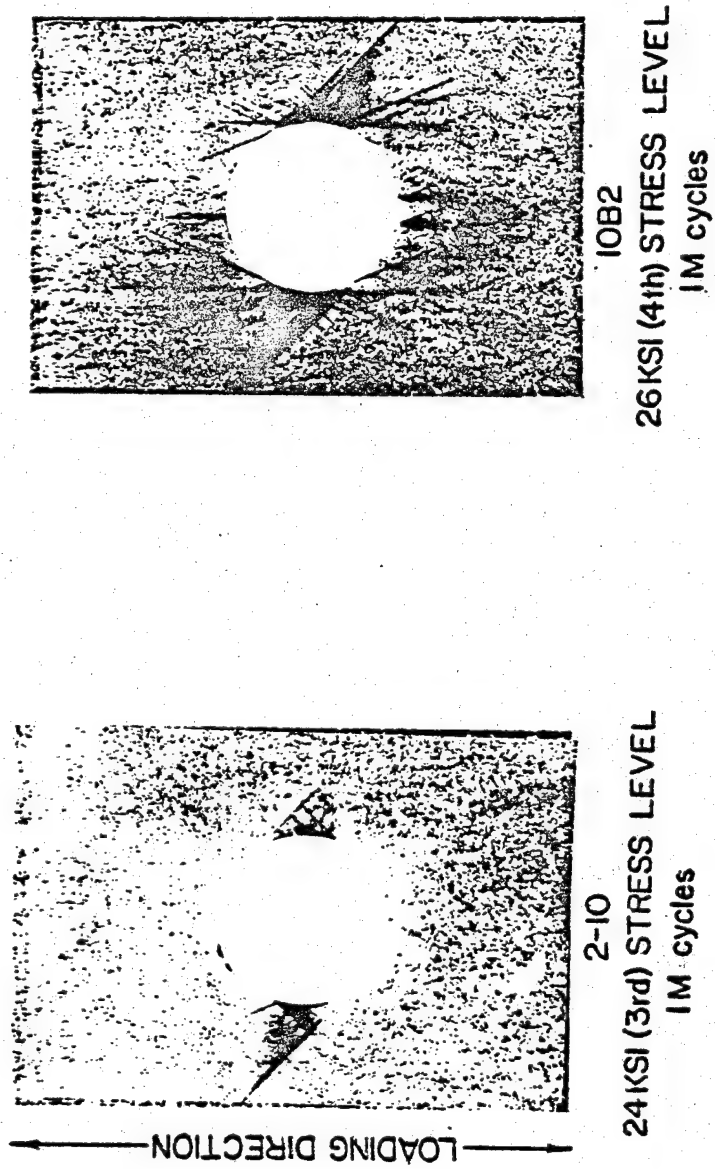
Figure 23. Flat X-ray radiographs (4X) of the 42 ply specimens after cyclic loading at the 24 and 26 ksi stress levels.

100
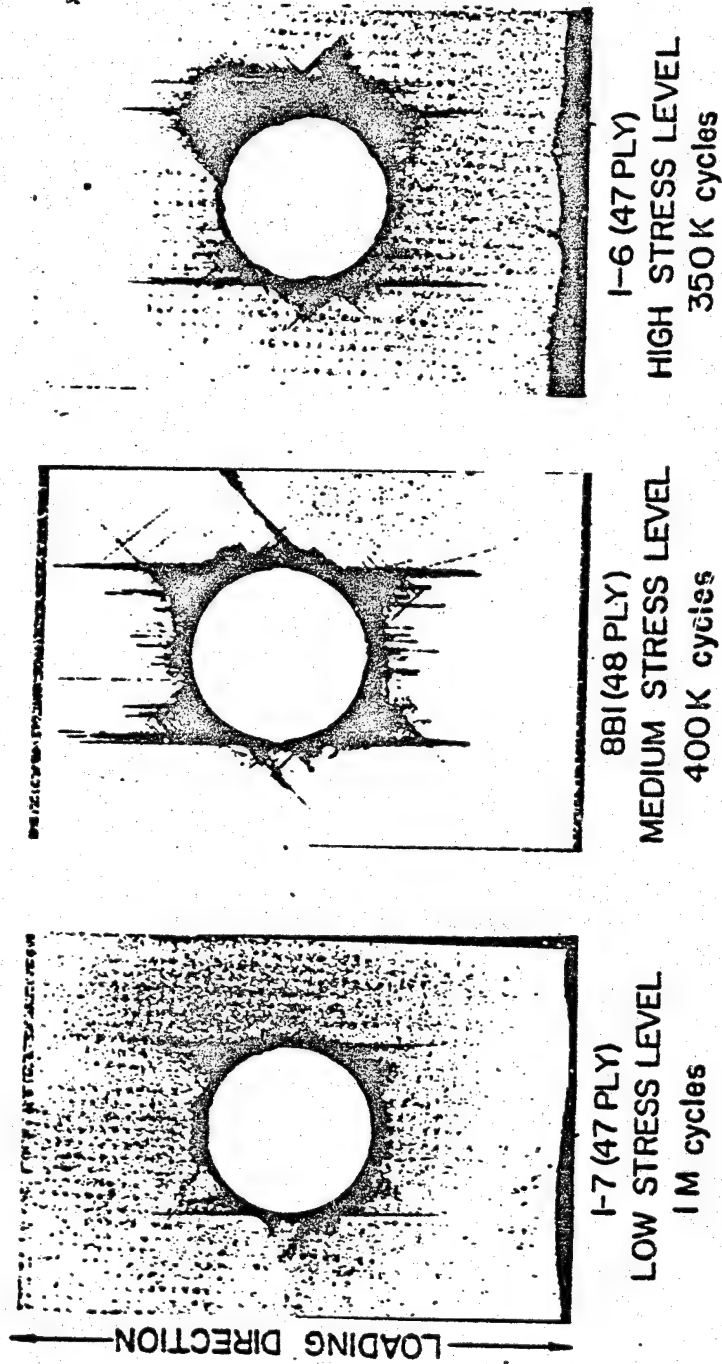
Figure 24. Flat X-ray radiographs (4X) of the 47 and 48 ply specimens after cyclic loading at the low, medium, and high stress levels.

LOADING DIRECTION

40K cycles

100K cycles
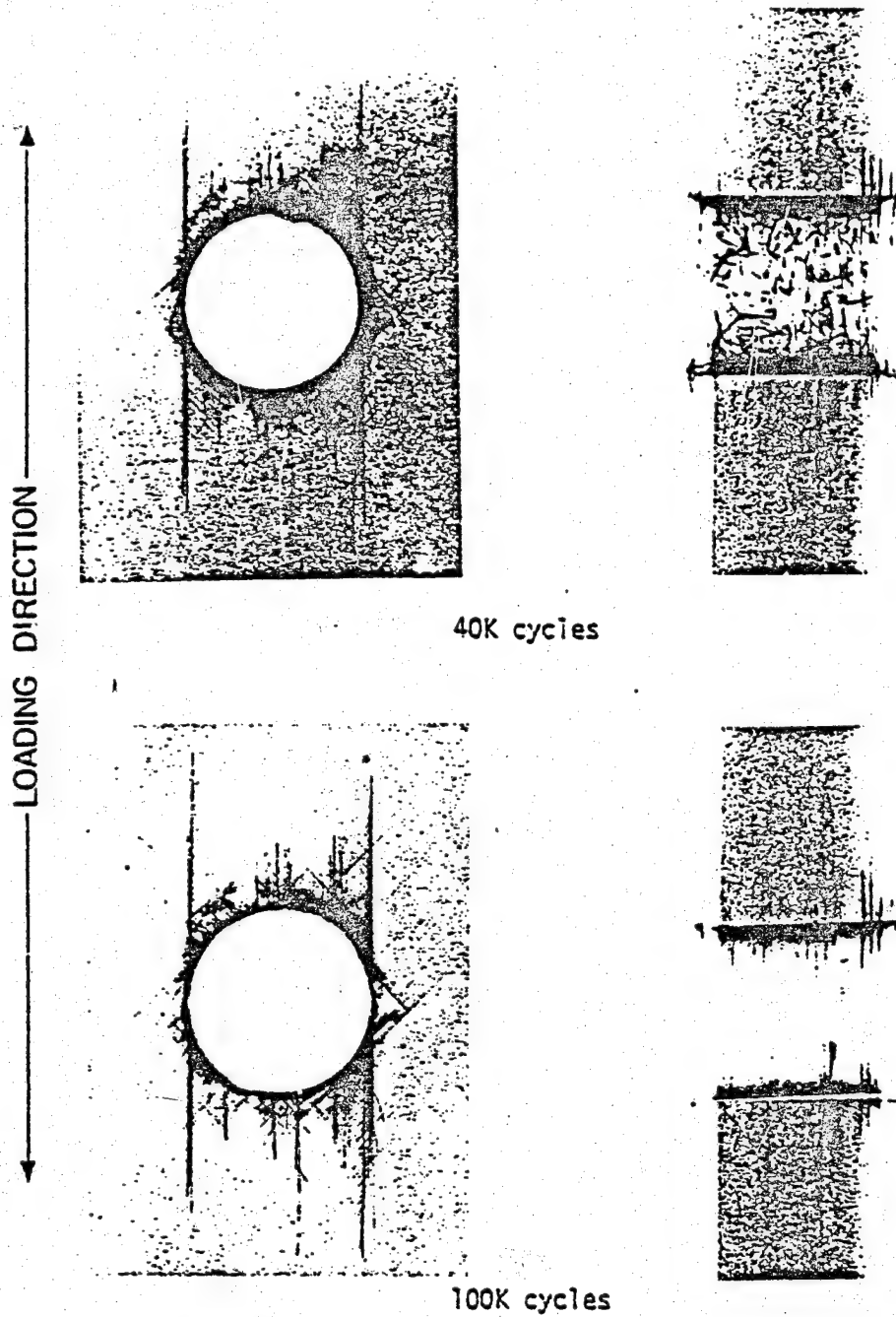
(4X)

Figure 25A. Flat and edge X-ray radiographs of specimen 7B1 (48 ply) during medium stress level fatigue.

LOADING DIRECTION

400K cycles

750K cycles
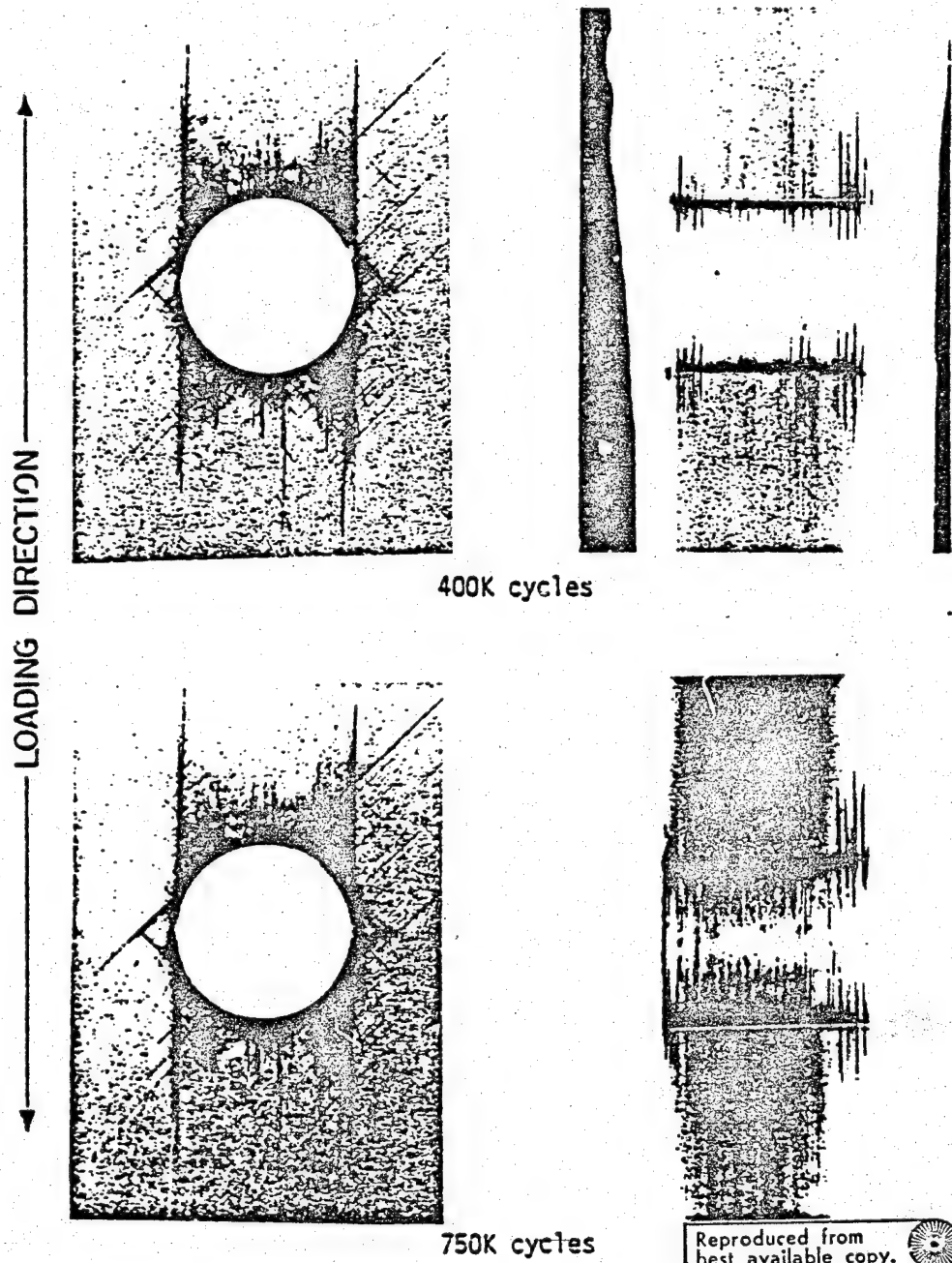
Figure 25B. Flat and edge X-ray radiographs (4X) of specimen 7B1 (48 ply) during medium stress level fatigue.

1300K cycles

2200K cycles
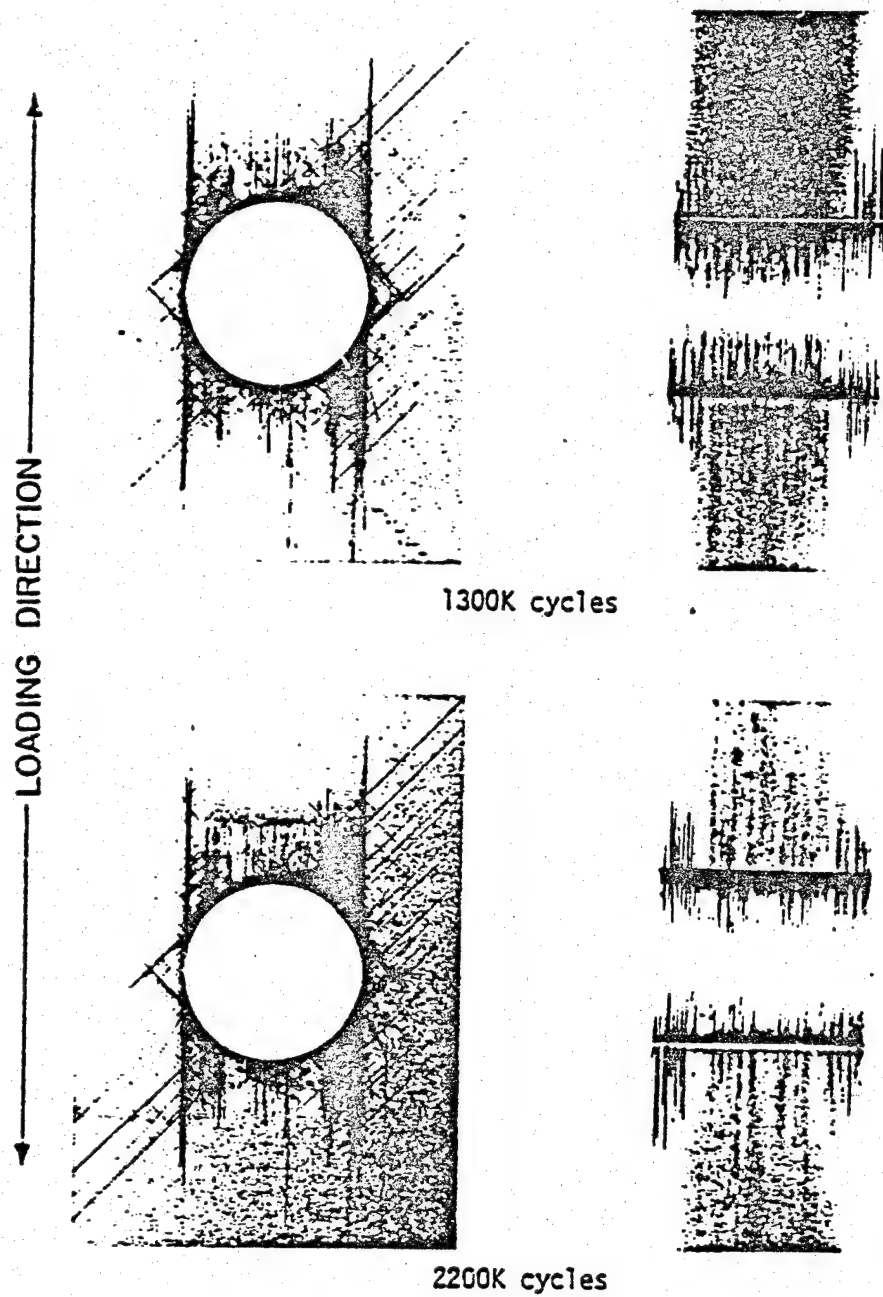
Figure 25C.   Flat and edge X-ray radiographs (4X) of specimen 7B1 (48 ply) during medium stress level fatigue.

25K cycles

250K cycles

LOADING DIRECTION

Figure 25A. Flat and edge X-ray radiographs (4X) of specimen 1C2 (42 ply) during level 4 (26 ksi) fatigue.

LOADING DIRECTION

440K cycles

1000K cycles
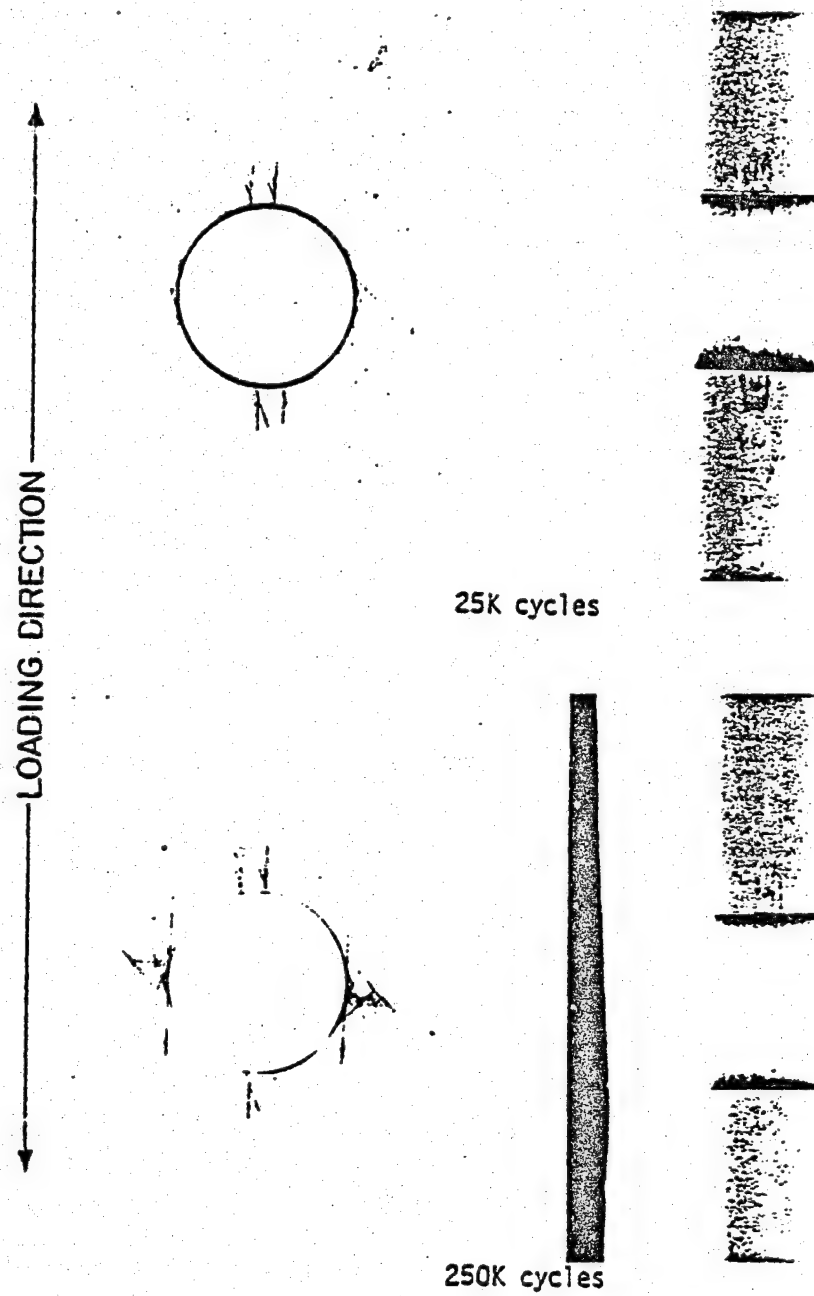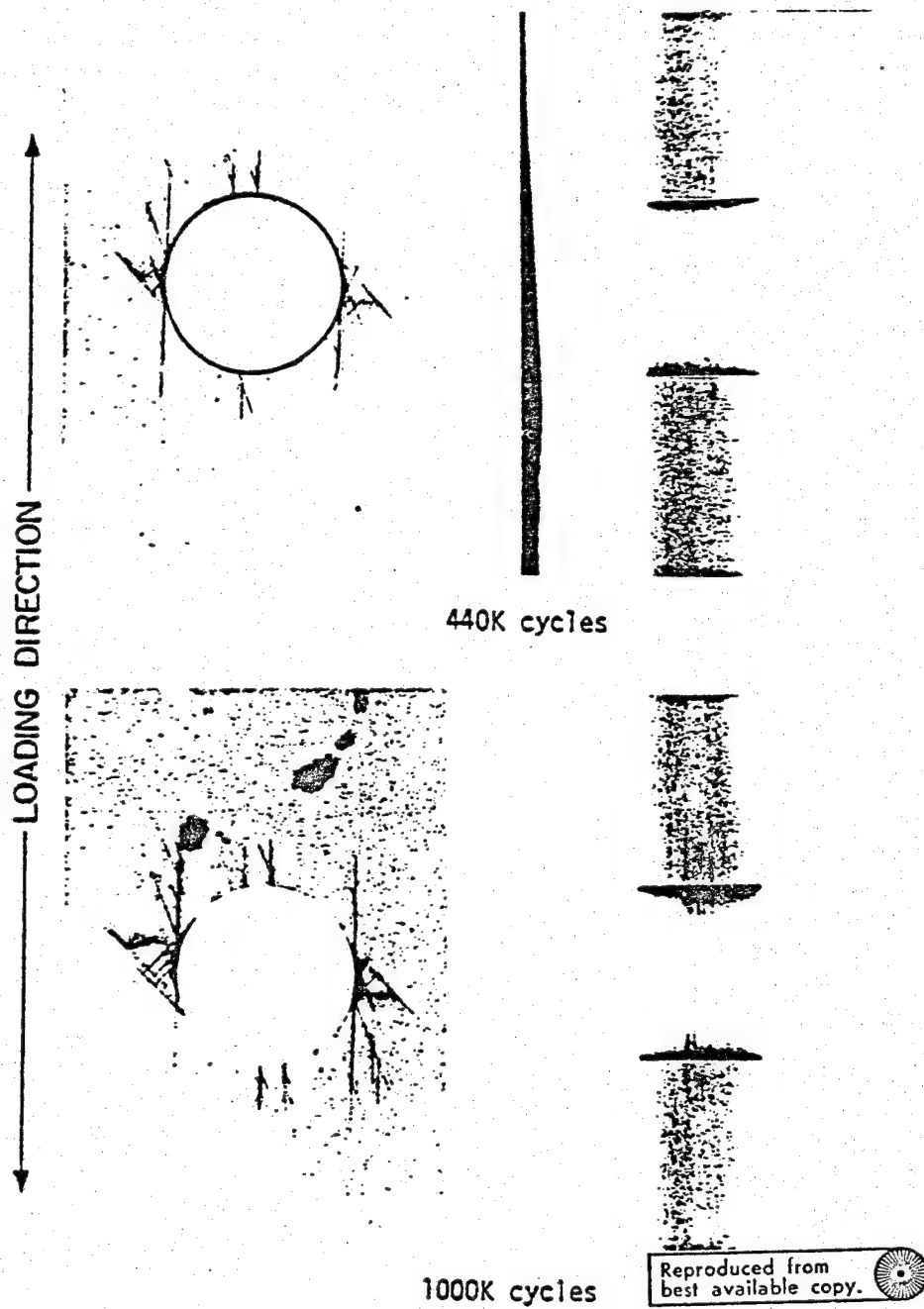
Figure 26B. Flat and edge X-ray radiographs (4X) of specimen 1C2 (42 ply) during level 4 (26 ksi) fatigue.

140K cycles

1000K cycles
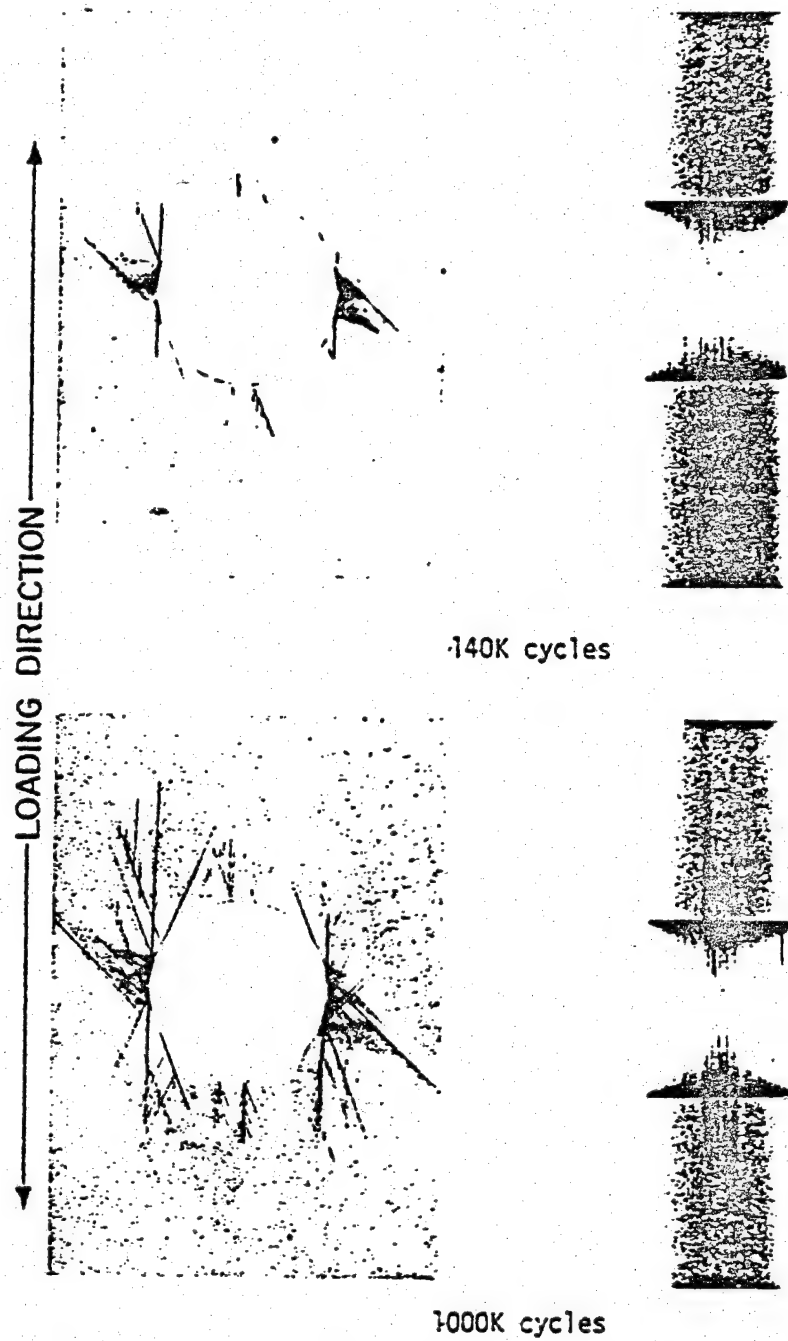
Figure 27. Flat and edge X-ray radiographs (4X) of specimen 10B2
(42 ply) during level 4 (26 ksi) fatigue.

C-scan
Initial

C-scan   X-ray
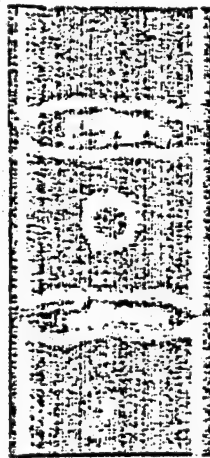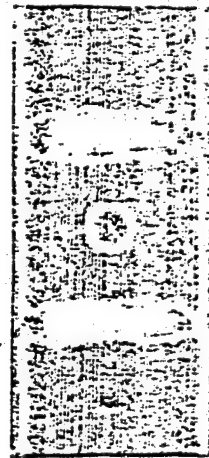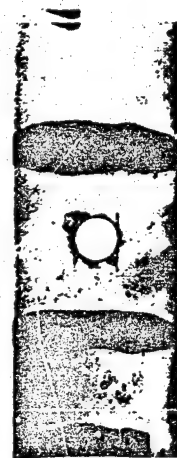
1M cycles

Figure 28. Damage history of specimen 1-8 (47 ply) cycled at the low stress level to 10^6 cycles.
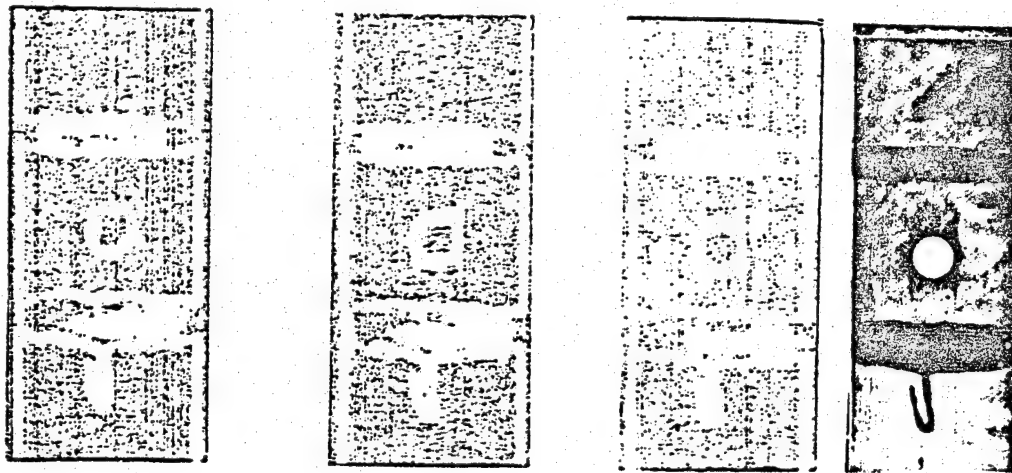
C-scan
Initial

C-scan
100k cycles

C-scan   X-ray
200k cycles
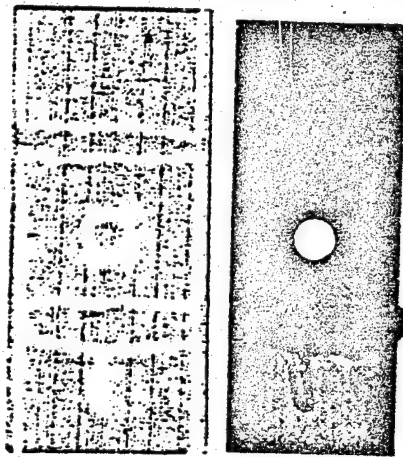
C-scan   X-ray
300k cycles

C-scan   X-ray
350k cycles
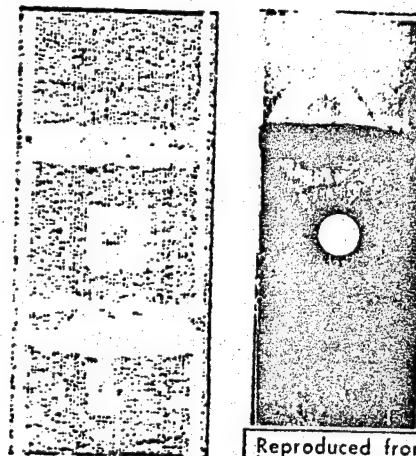
Figure 29.   Damage history of specimen 1-6 (47 ply) cycled at the high
stress level to 3.5×10^5 cycles.
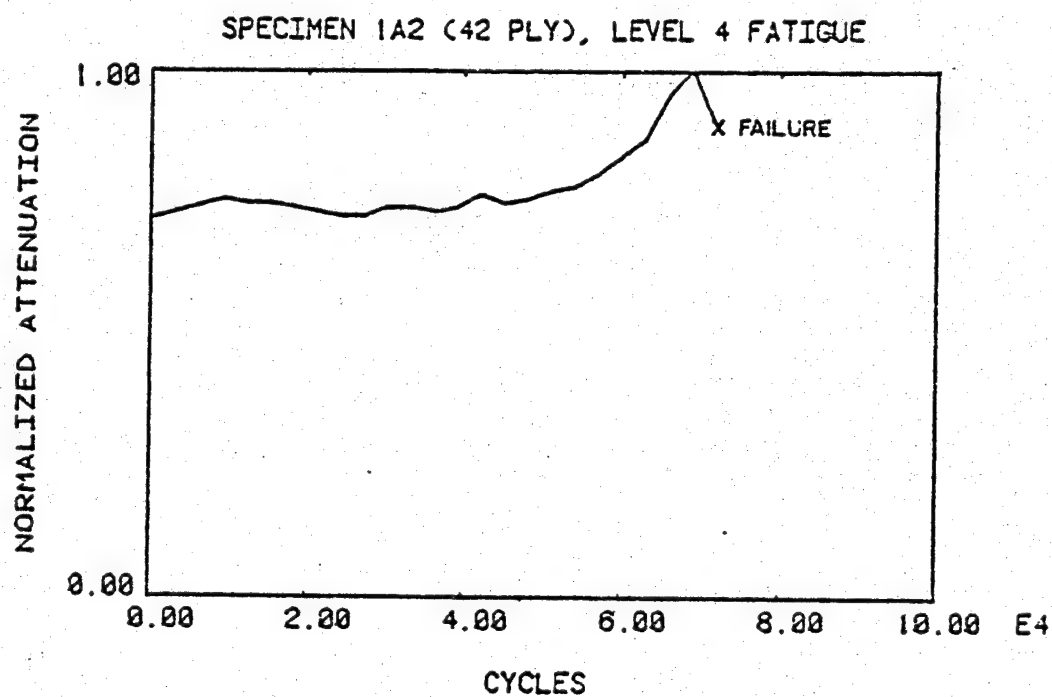
Figure 30. Normalized ultrasonic attenuation vs. fatigue cycles for specimen 1A2 (42 ply) during level 4 fatigue.

SPECIMEN 1-12 (47 PLY), MEDIUM LEVEL FATIGUE
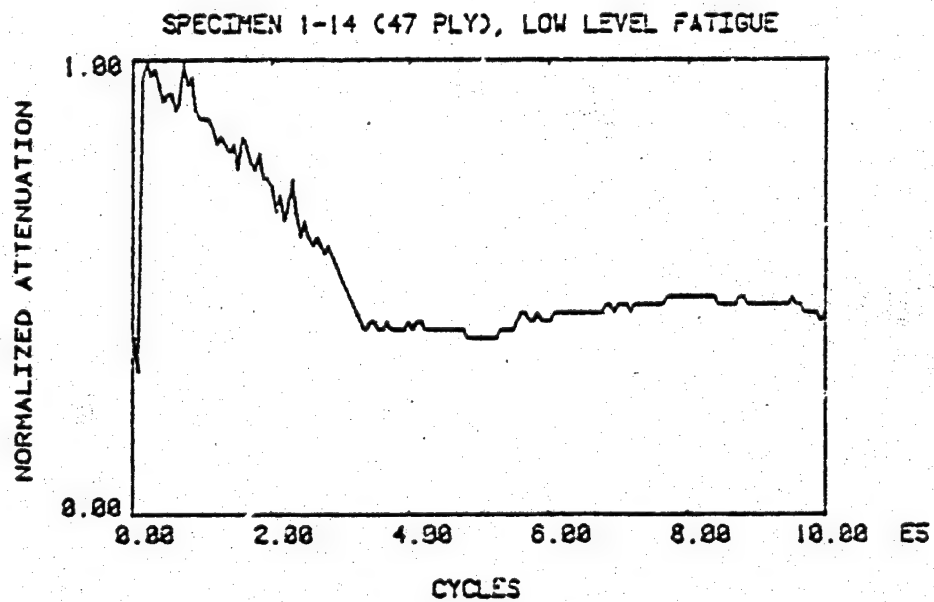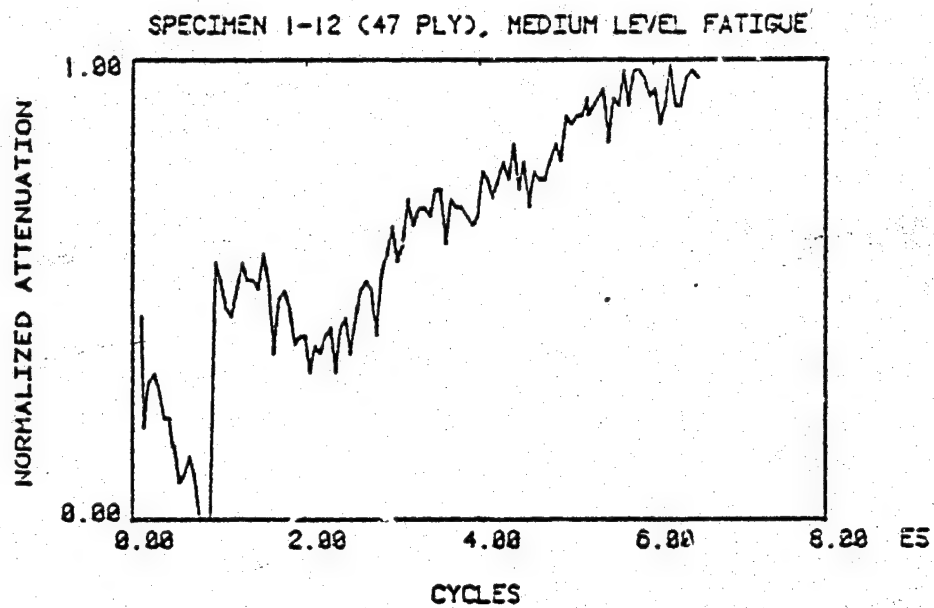
Figure 31. Normalized ultrasonic attenuation vs. fatigue cycles for 47 ply specimens at medium and low level fatigue.

Figure 32. Sectioning study schematic showing cut locations.

112

LOADING DIRECTION

TOP

1

2
3
4

L

R

(8x)

4' 3' 2' 1'

BOTTOM
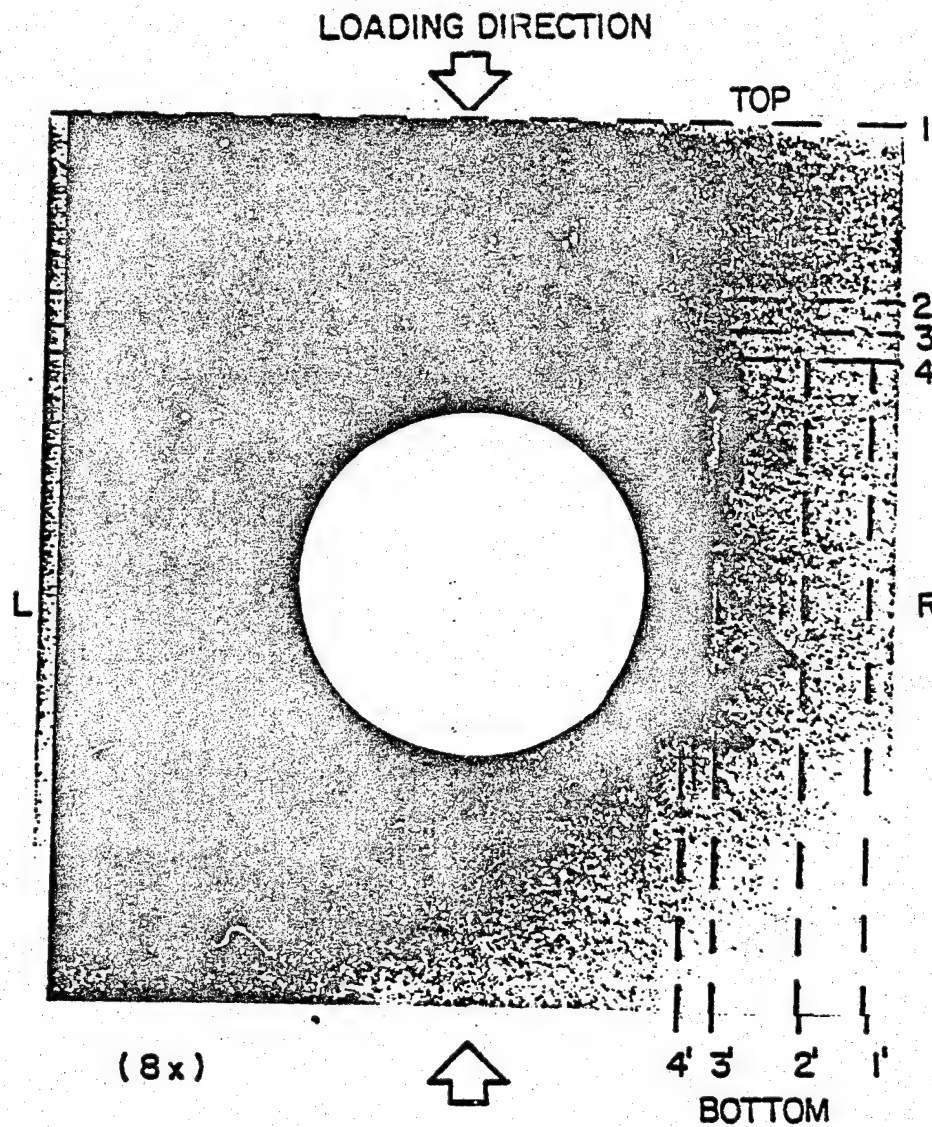
Figure 33. Flat X-ray radiograph of specimen 1-6 (47 ply) showing
sectioned locations.

113
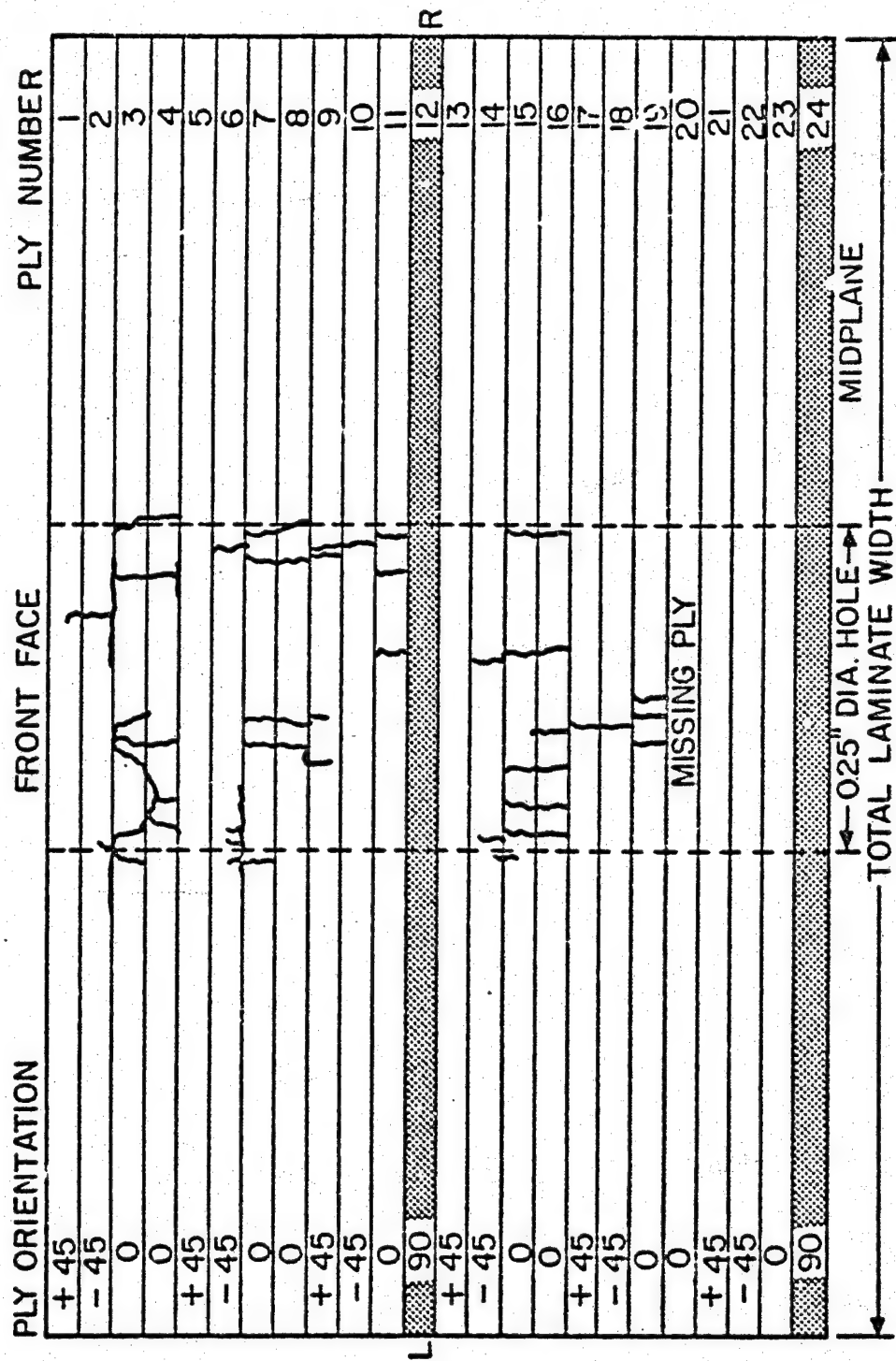
Figure 34A. The fourth transverse section of specimen 1-6 (47 ply) showing damage detail (90 deg. plies have been highlighted for viewing ease).

114

Figure 34B. The fourth transverse section of specimen 1-6 (47 ply) showing damage detail (90 deg. plies have been highlighted for viewing ease).
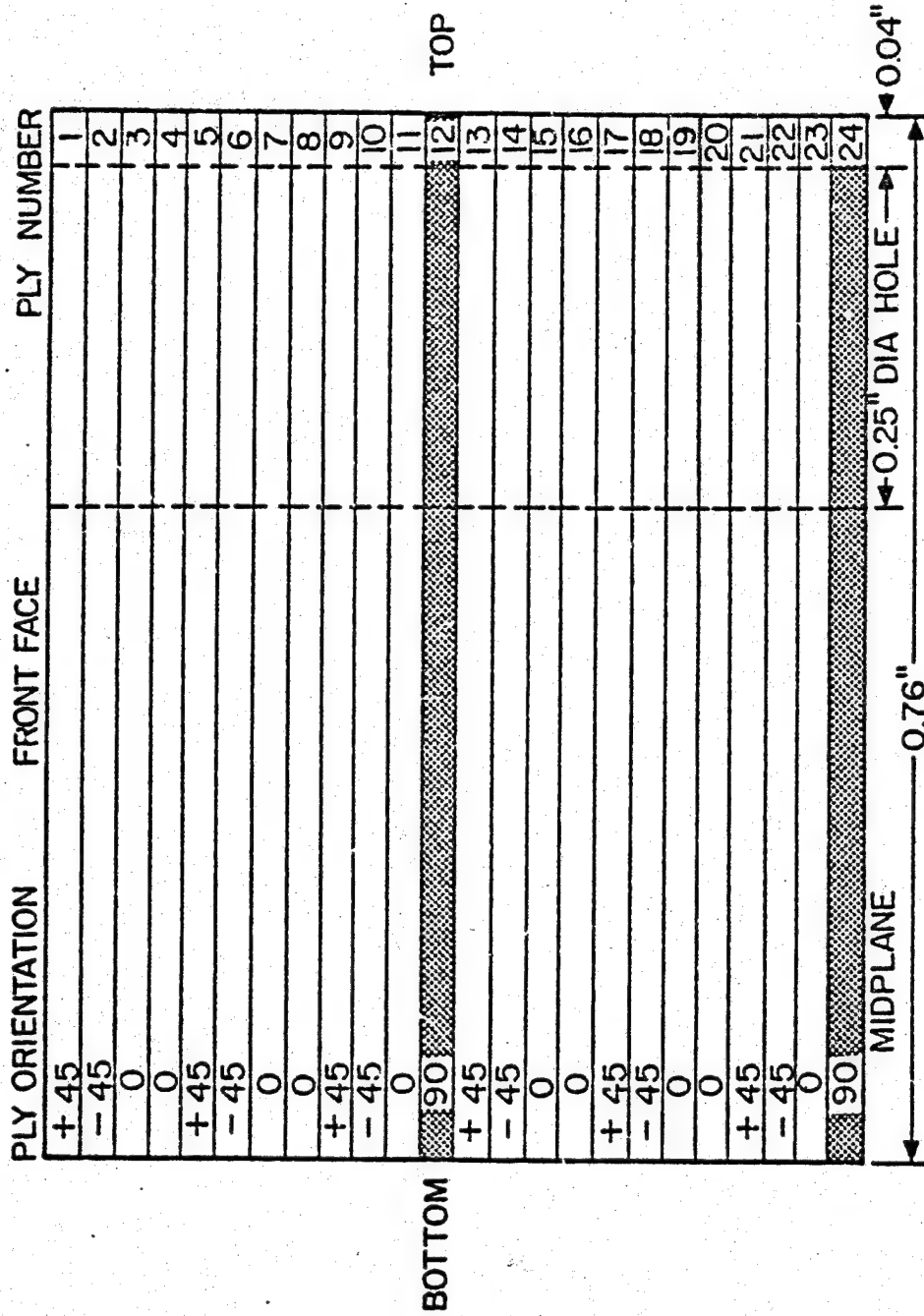
Figure 35A. The third longitudinal section of specimen 1-6 (47 ply) showing damage detail (90 deg. plies have been highlighted for viewing ease).
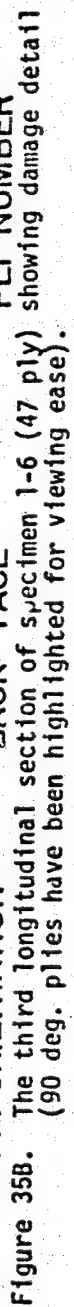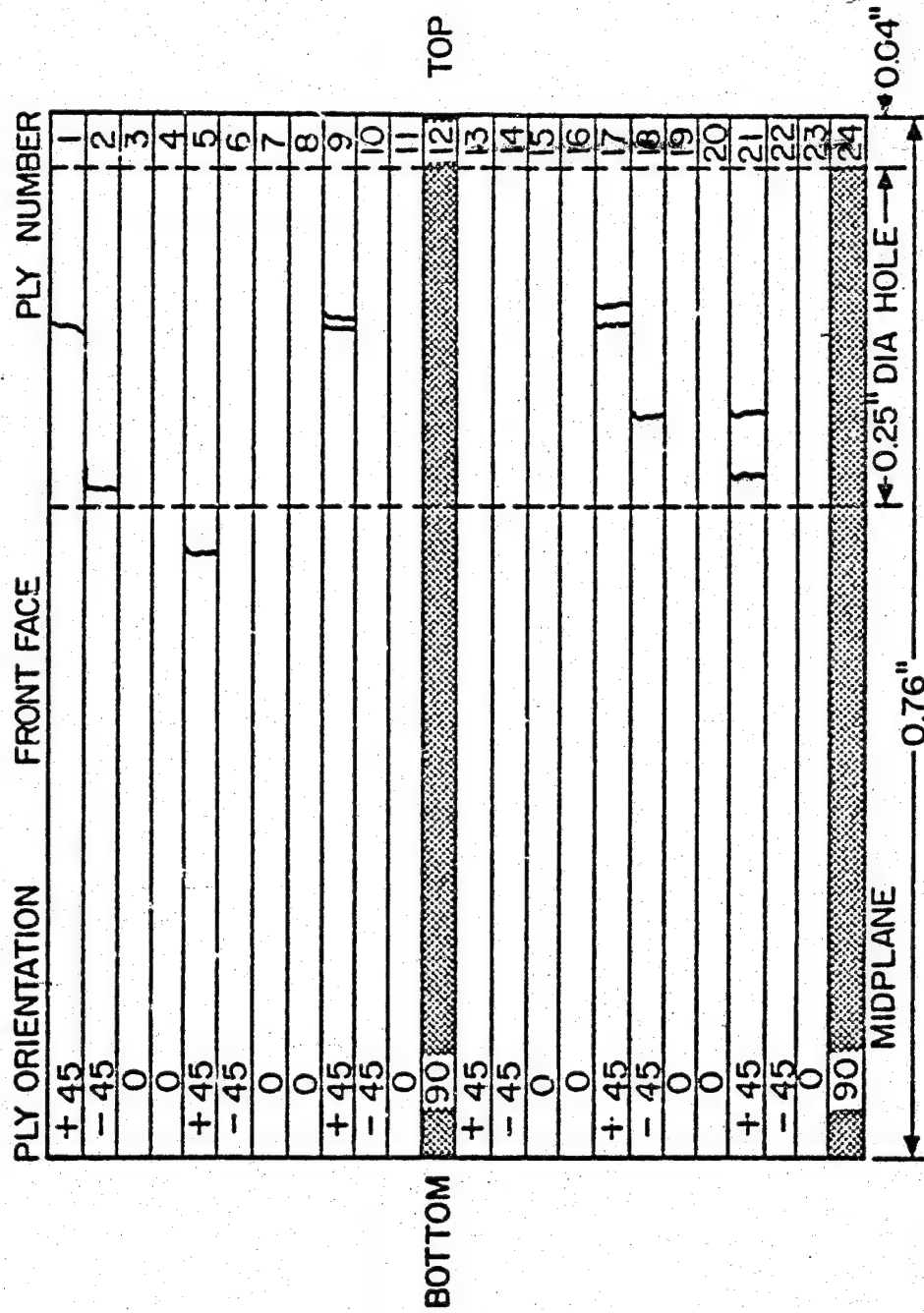
Figure 35B. The third longitudinal section of specimen 1-6 (47 ply) showing damage detail (90 deg. plies have been highlighted for viewing ease).
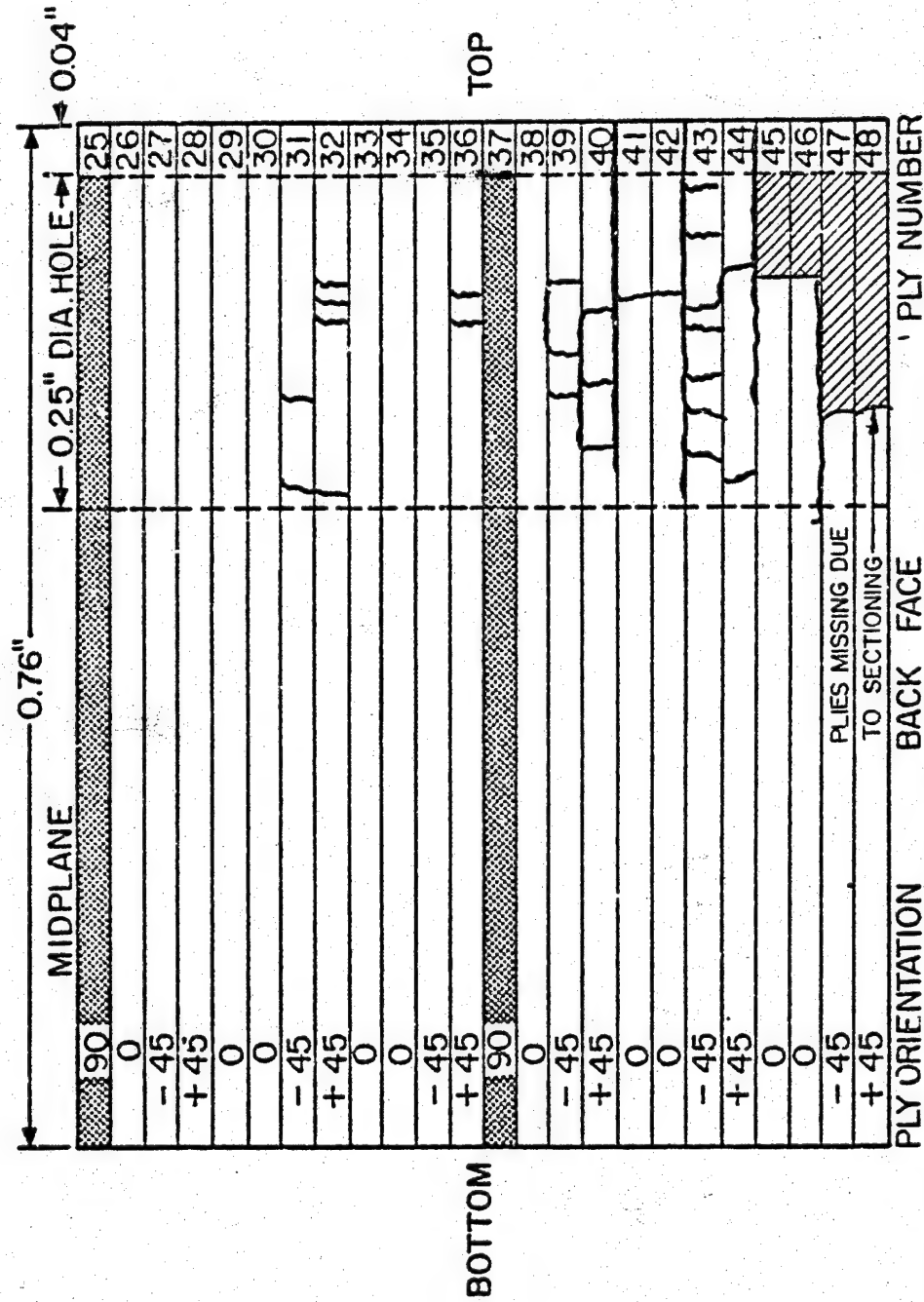
Figure 36A.   The fourth longitudinal section of specimen 1-6 (47 ply) showing damage detail (90 deg. plies have been highlighted for viewing ease).
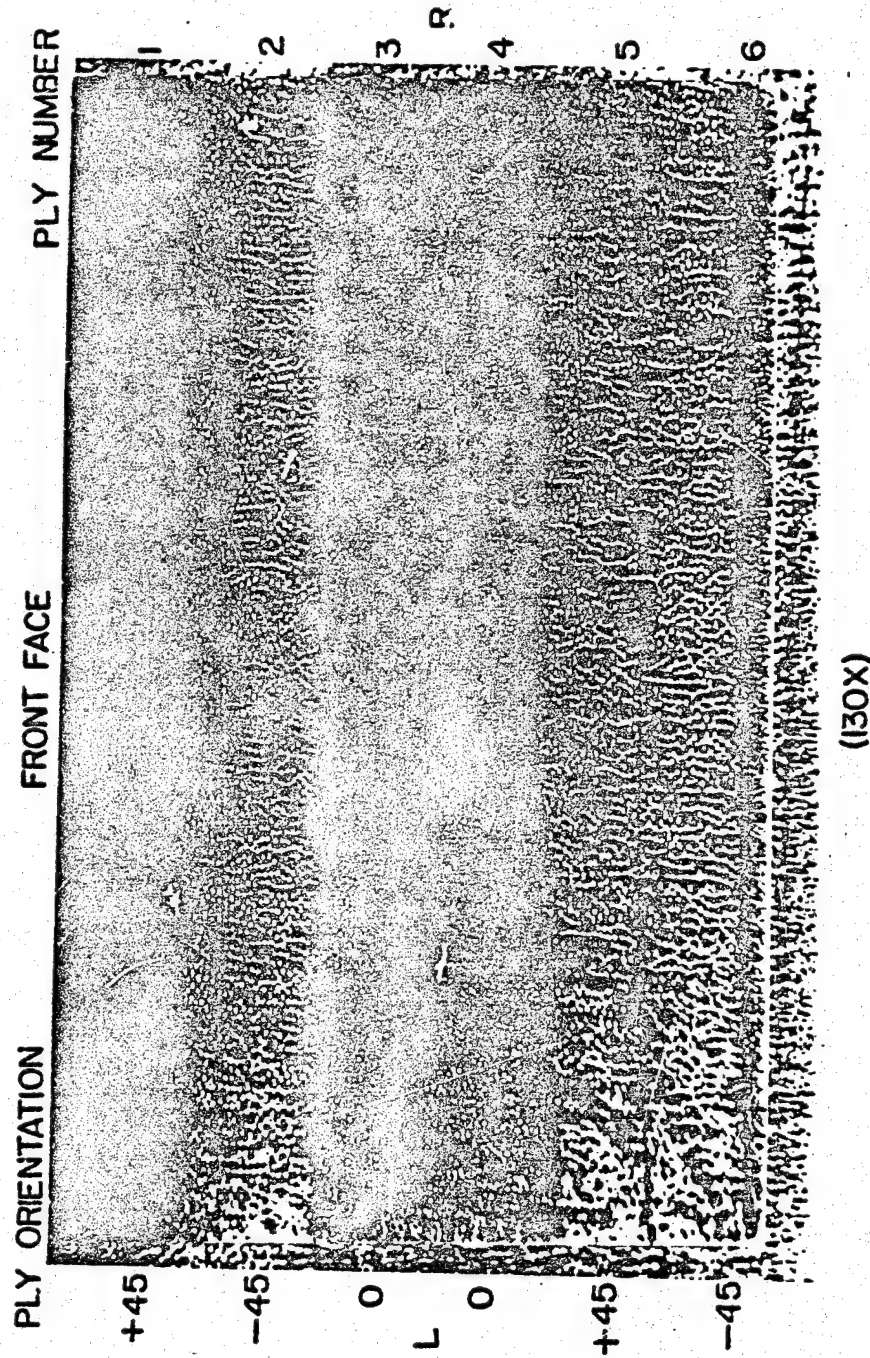
Figure 36B. The fourth longitidinal section of specimen 1-6 (47 ply) showing damage detail (90 deg. plies have been highlighted for viewing ease).

Figure 37. Light micrograph of the fourth transverse section of specimen 1-6 showing matrix cracking and delamination in zero deg. plies.
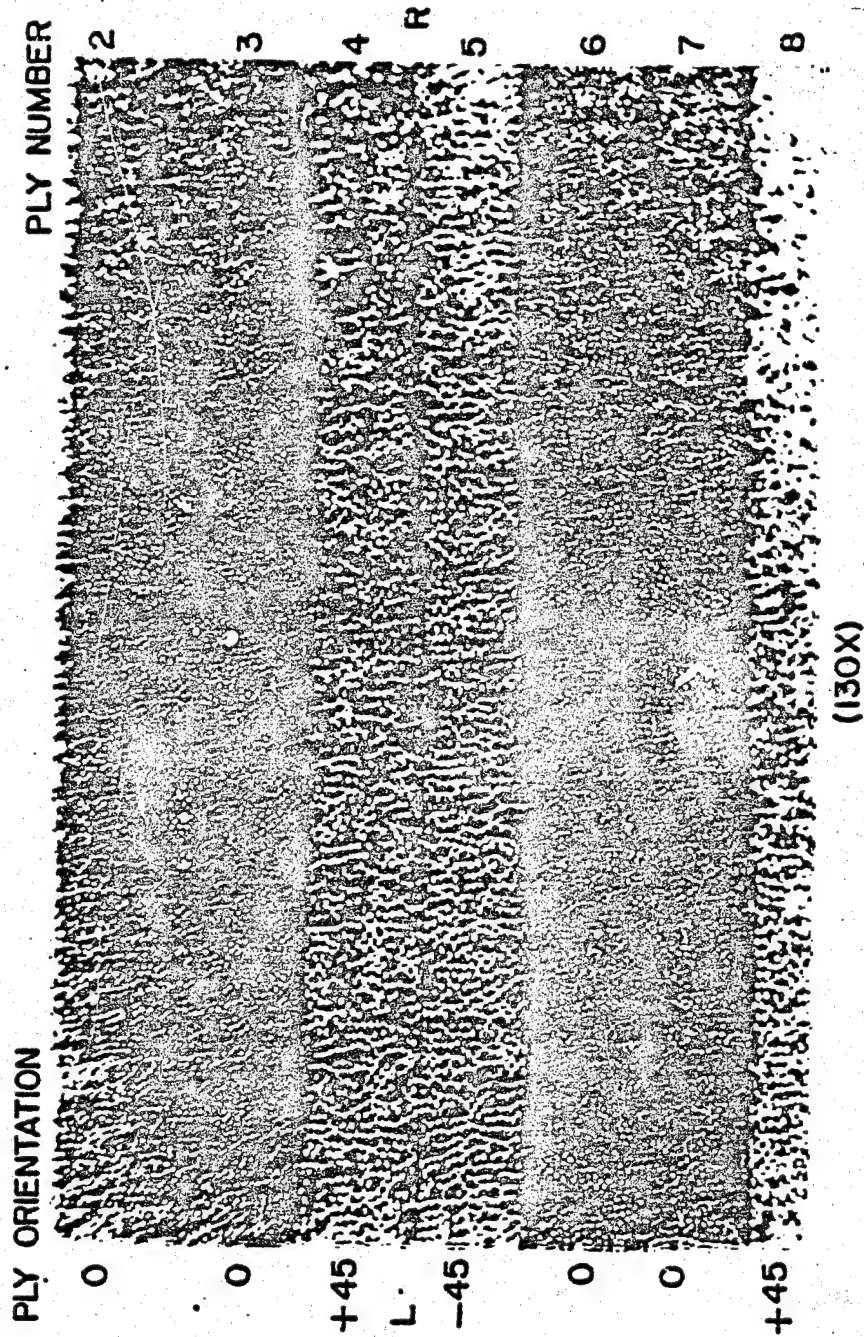
Figure 38. Light micrograph of the fourth transverse section of specimen 1-6 showing matrix cracks in the zero deg. plies.
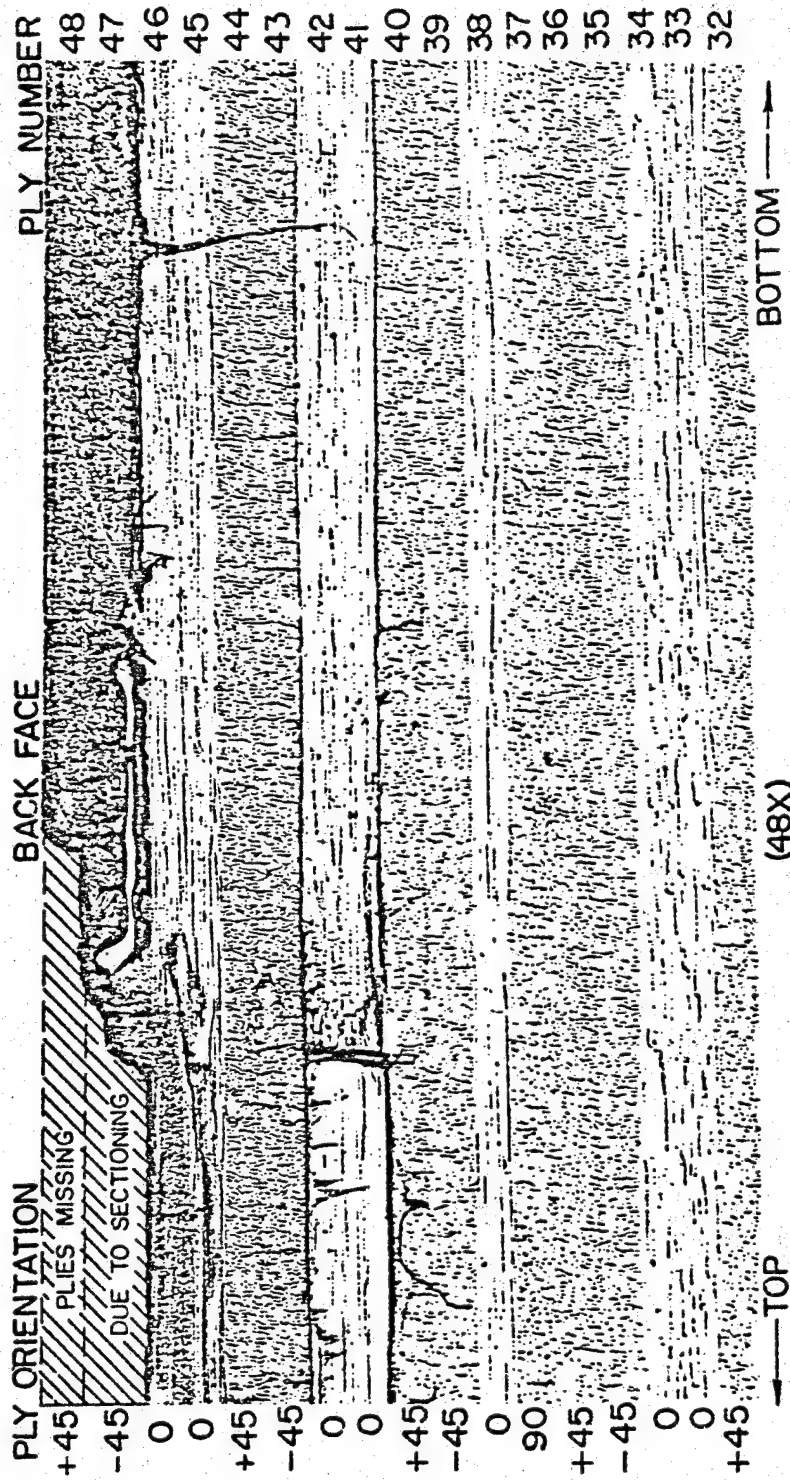
(130X)

Figure 39. Replica of the third longitudinal section of specimen 1-6 (47 ply) showing delaminations at the 45/0 interfaces.
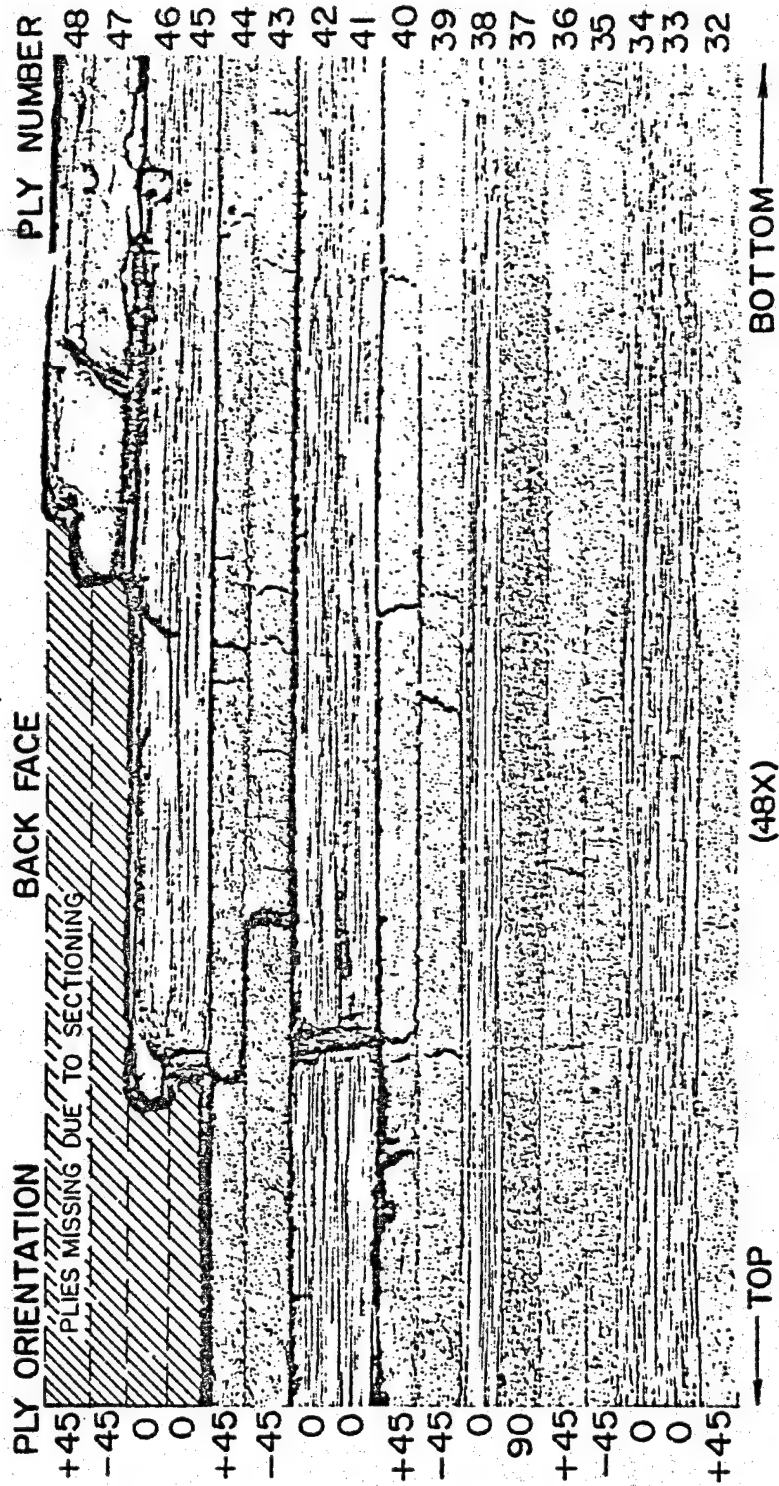
122

Figure 40. Replica of the fourth longitudinal section of specimen 1-6 (47 ply) showing delaminations at the 45/0 interfaces and matrix cracking.
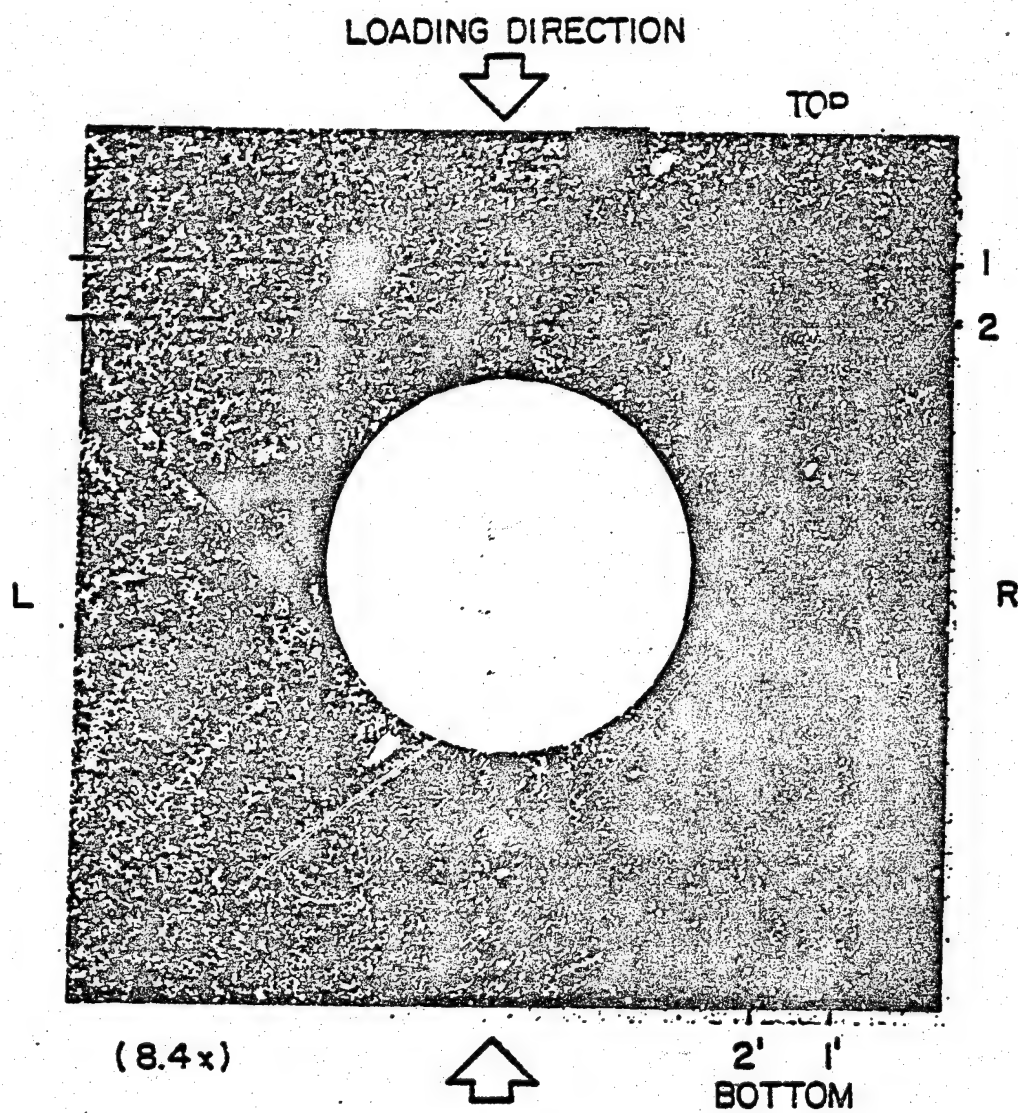
Figure 41. Flat X-ray radiograph of specimen 1C2 (42 ply) showing
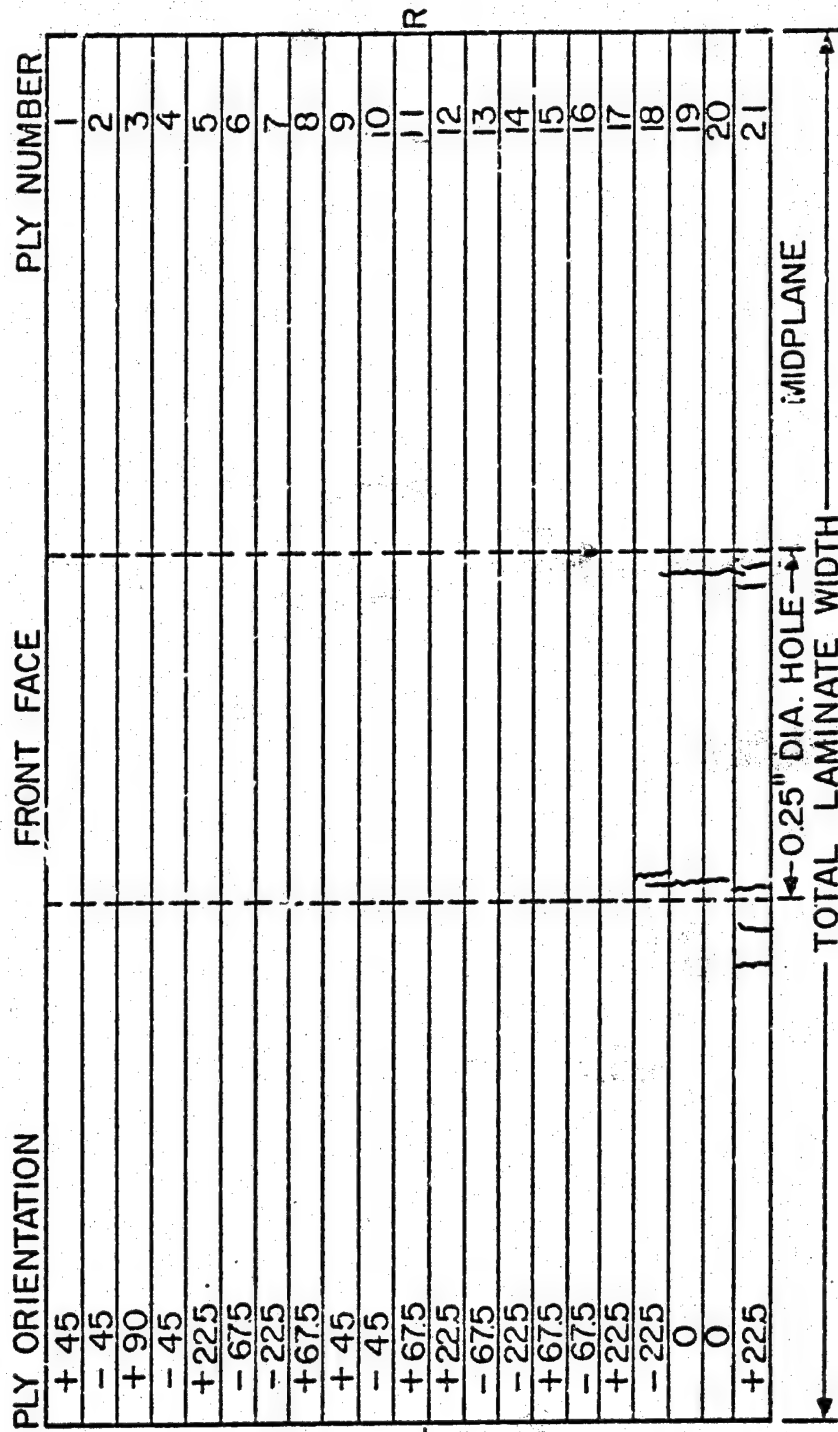sectioned locations.

PLY NUMBER	PLY ORIENTATION
1	+45
2	-45
3	+90
4	-45
5	+225
6	-675
7	-225
8	+675
9	+45
10	-45
11	+675
12	+225
13	-675
14	-225
15	+675
16	-675
17	+225
18	-225
19	0
20	0
21	+225

FRONT FACE

L   R

MIDPLANE

|← 0.25" DIA. HOLE →|

TOTAL LAMINATE WIDTH

Figure 42A. The first transverse section of specimen 1C2 (42 ply) showing damage detail.

PLY ORIENTATION	PLY NUMBER
+22.5	22
0	23
0	24
-22.5	25
+22.5	26
-67.5	27
+67.5	28
-22.5	29
-67.5	30
+22.5	31
+67.5	32
-45	3
+45	4
+67.5	5
-22.5	6
-67.5	37
+22.5	38
-45	39
+90	40
-45	41
+45	42

TOTAL LAMINATE WIDTH
0.25" DIA HOLE
MIDPLANE
BACK FACE
L R

Figure 42B. The first transverse section of specimen 1C2 (42 ply) showing damage detail.

PLY ORIENTATION	PLY NUMBER
+ 45	1
- 45	2
+ 90	3
- 45	4
+ 22.5	5
- 67.5	6
- 22.5	7
+ 67.5	8
+ 45	9
- 45	10
+ 67.5	11
+ 22.5	12
- 67.5	13
- 22.5	14
+ 67.5	15
- 67.5	16
+ 22.5	17
- 22.5	18
0	19
0	20
+ 22.5	21

FRONT FACE

0.25" DIA. HOLE

TOTAL LAMINATE WIDTH
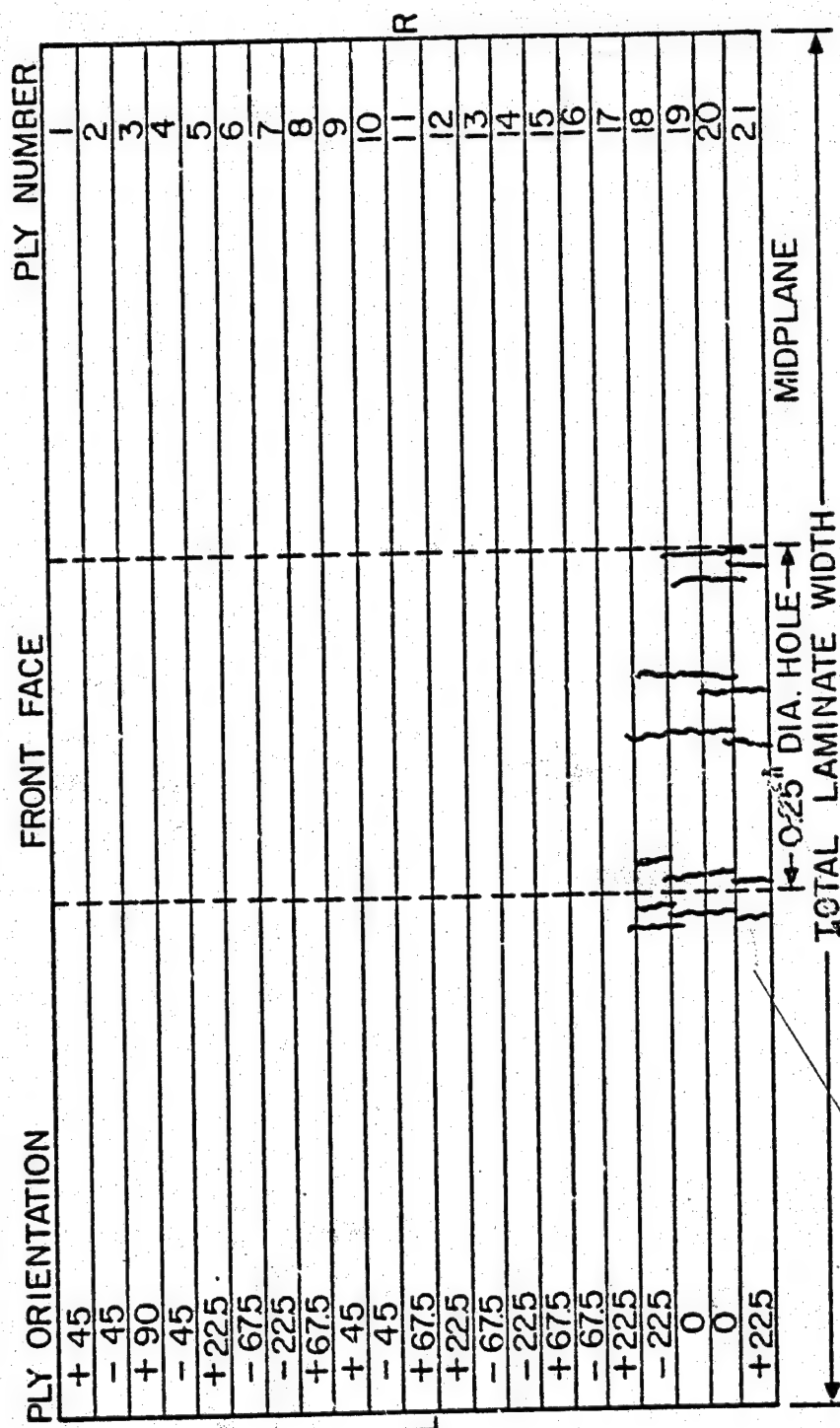
MIDPLANE

Figure 43A.   The second transverse section of specimen 1C2 (42 ply) showing damage detail.

127

Figure 43B. The second transverse section of specimen 1C2 (42 ply) showing damage detail.

PLY ORIENTATION   FRONT FACE   PLY NUMBER

TOP

Ply Orientation	Ply Number
+ 45	1
− 45	2
+ 90	3
− 45	4
+ 22.5	5
− 67.5	6
− 22.5	7
+ 67.5	8
+ 45	9
− 45	10
+ 67.5	11
+ 22.5	12
− 67.5	13
− 22.5	14
+ 67.5	15
− 67.5	16
+ 22.5	17
− 22.5	18
0	19
0	20
+ 22.5	21

BOTTOM

MIDPLANE

0.74" ← 0.25" DIA HOLE → ↑ 0.04"

Figure 44A. The second longitudinal section of specimen 1C2 (42 ply) showing damage detail.

0.04"

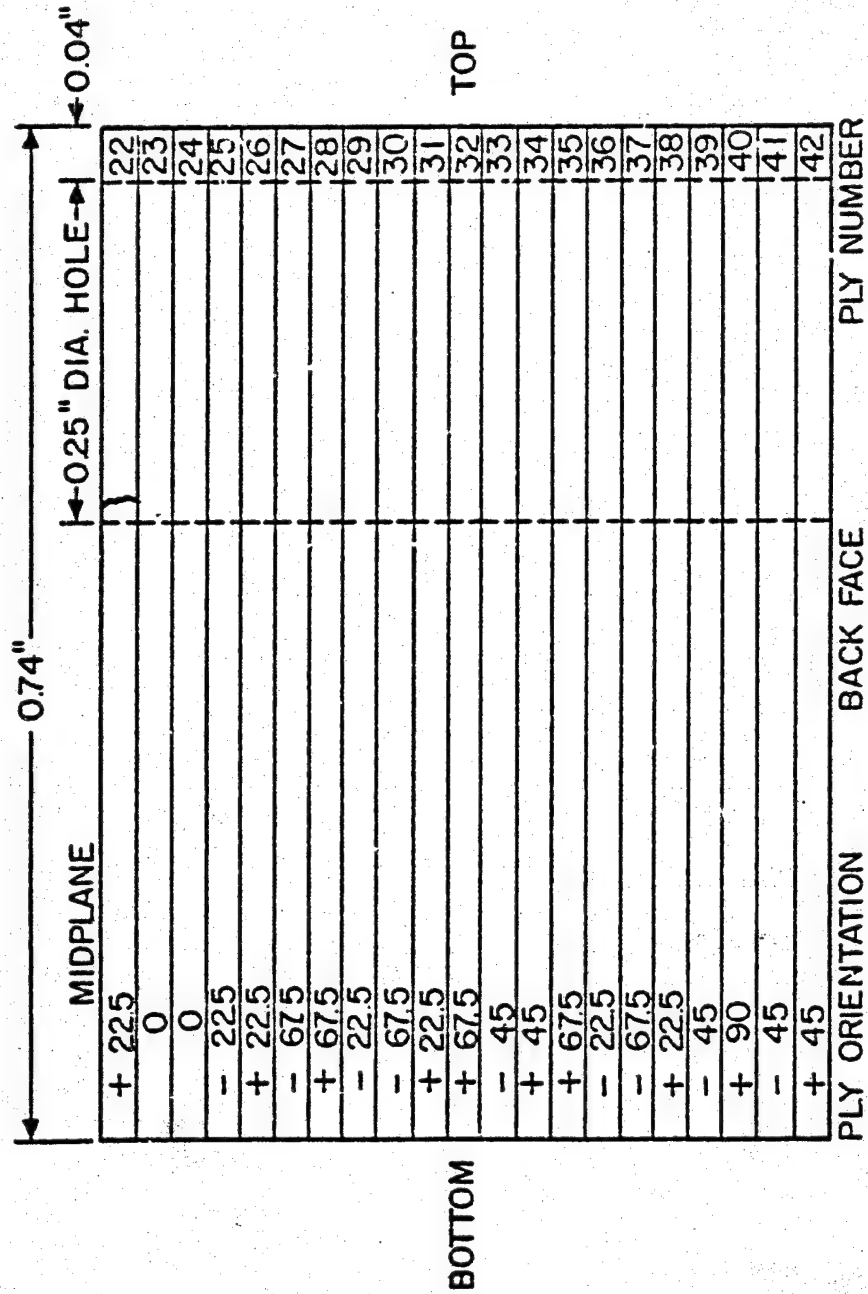0.25" DIA. HOLE

0.74"

MIDPLANE

TOP

BOTTOM

PLY ORIENTATION	BACK FACE	PLY NUMBER
+ 22.5		22
0		23
0		24
– 22.5		25
+ 22.5		26
– 67.5		27
+ 67.5		28
– 22.5		29
– 67.5		30
+ 22.5		31
+ 67.5		32
– 45		33
+ 45		34
+ 67.5		35
– 22.5		36
– 67.5		37
+ 22.5		38
– 45		39
+ 90		40
– 45		41
+ 45		42

Figure 44B. The second longitudinal section of specimen IC2 (42 ply) showing damage detail.

PLY NUMBER

PLY ORIENTATION

+22.5 — 26

−22.5 — 25

0 — 24

0 — 23

+22.5 — 22

+22.5 — 21

0 — 20

0 — 19

−22.5 — 18
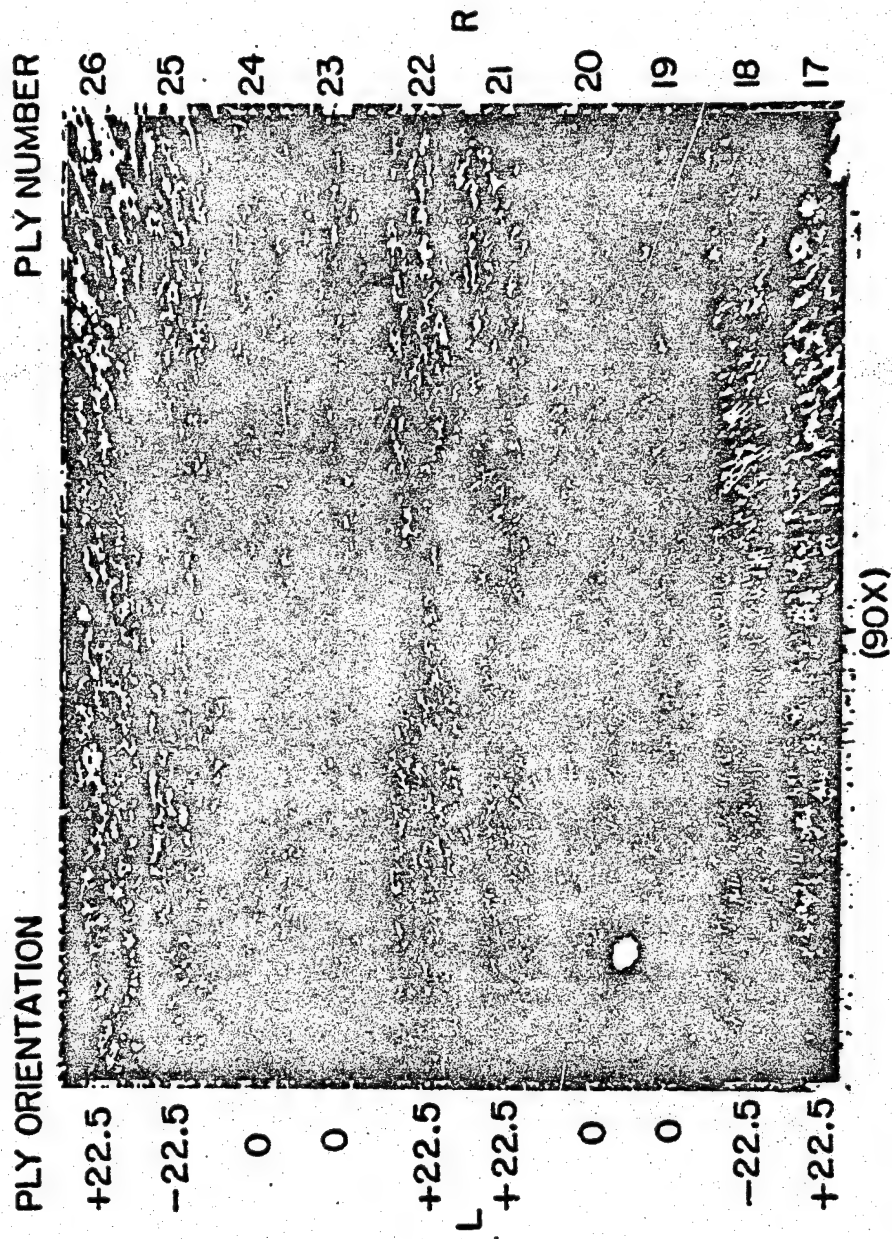
+22.5 — 17

R

L

(90X)

Figure 45. Light micrograph of the second transverse section of specimen 1C2 (42 ply) showing matrix cracking.
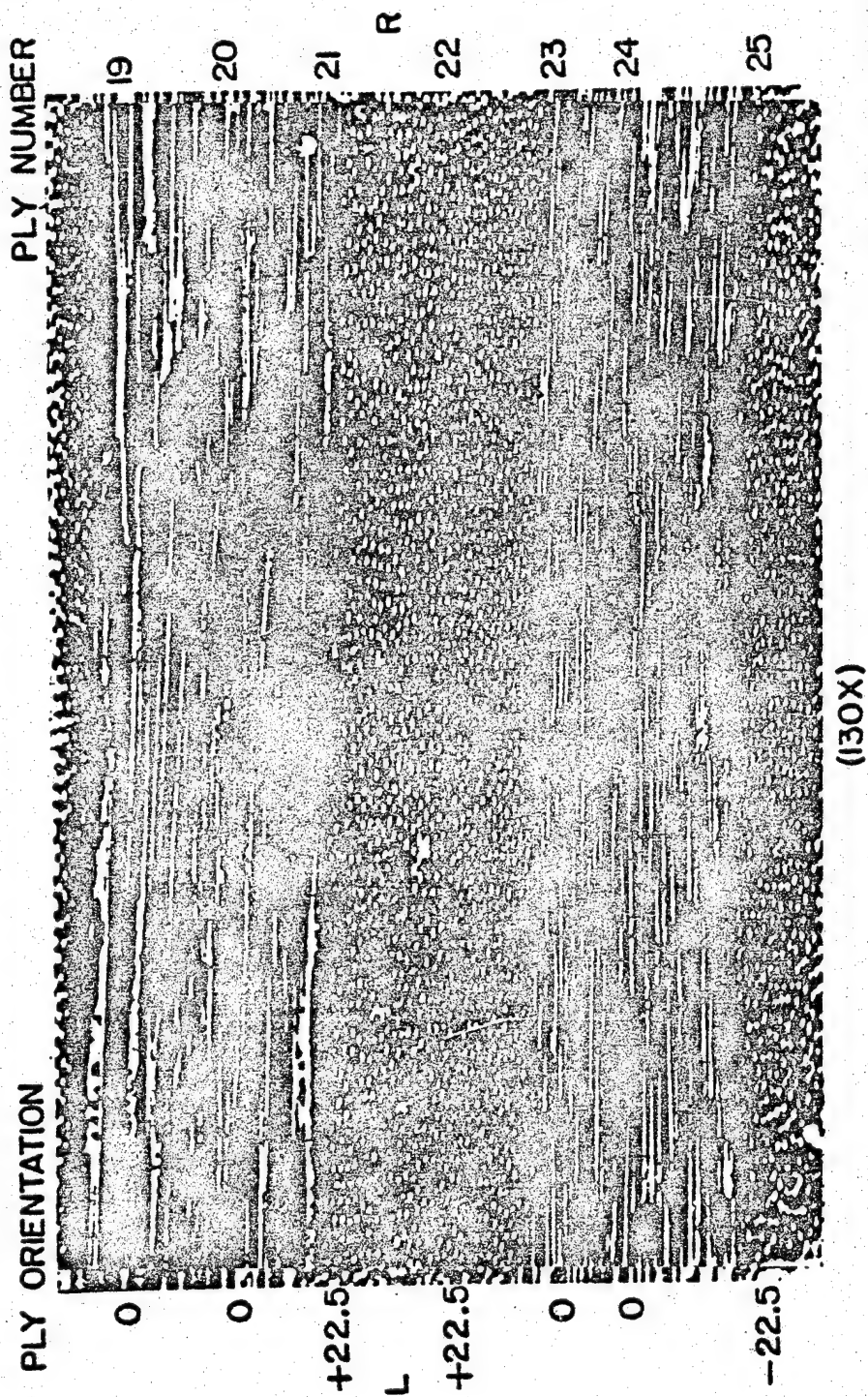
(130X)

Figure 46. Light micrograph of the second longitudinal section of specimen 1C2 (42 ply) showing single matrix crack in 22.5 deg. plies.
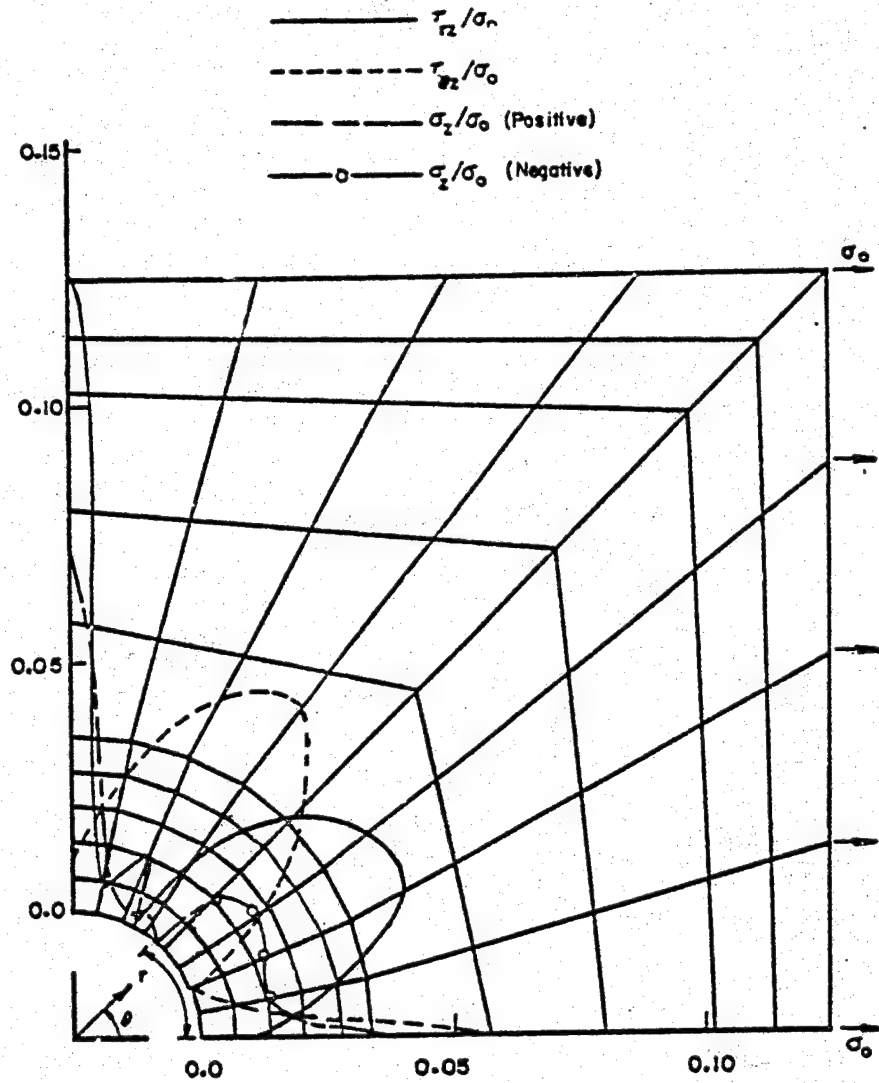
Figure 47. Interlaminar stresses, normalized, in the 48 ply laminate between +45 and -45 deg. plies (plies 1 and 2) at the first interface (figure taken from reference 18).
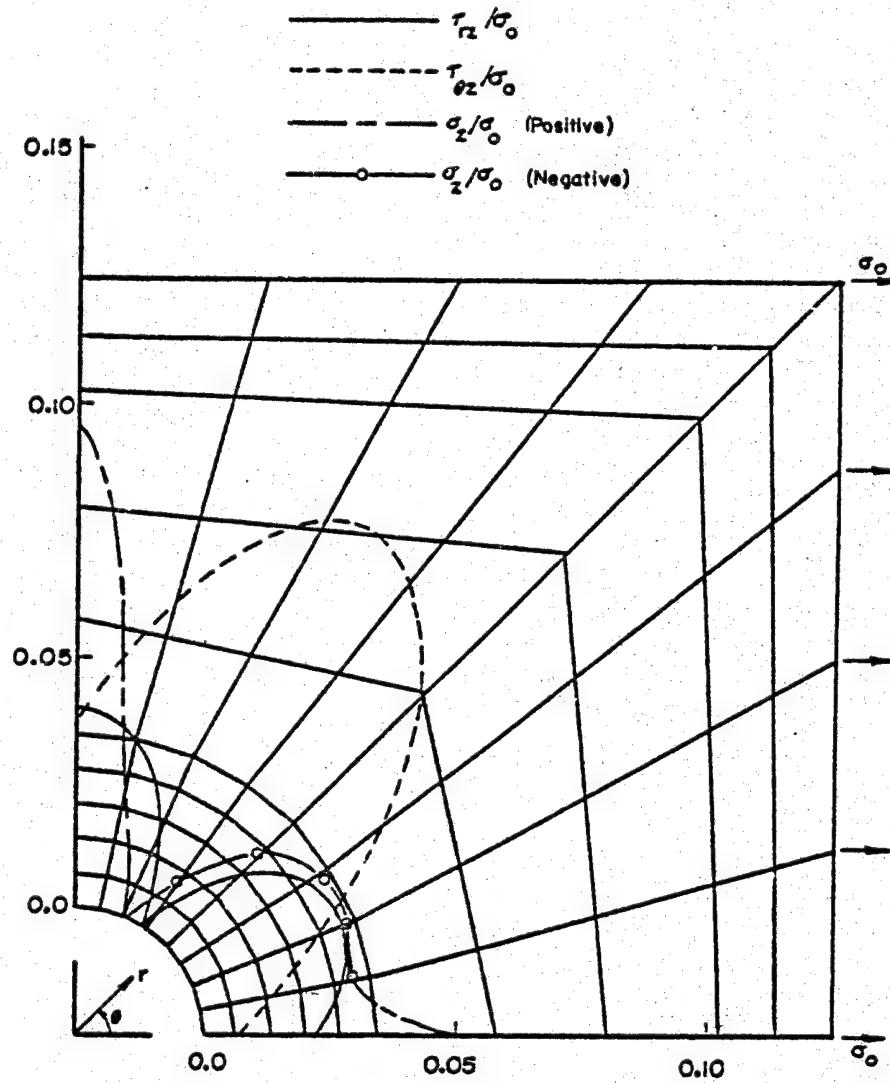
Figure 48. Interlaminar stresses, normalized, in the 48 ply laminate between -45 and 0 deg. plies (plies 2 and 3) at the second interface (figure taken from reference 18).
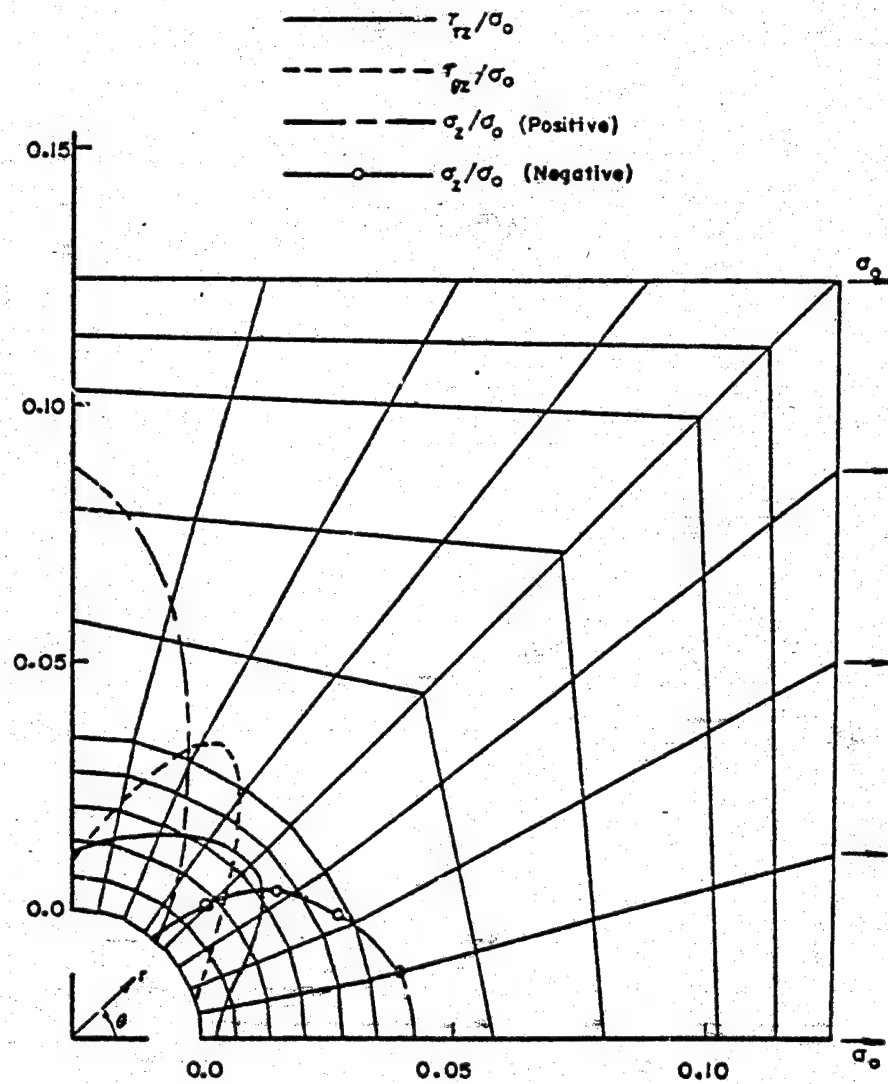
Figure 49. Interlaminar stresses, normalized, in the 48 ply laminate between the 0 and +45 deg. plies (plies 4 and 5) at the fourth interface (figure taken from reference 13).
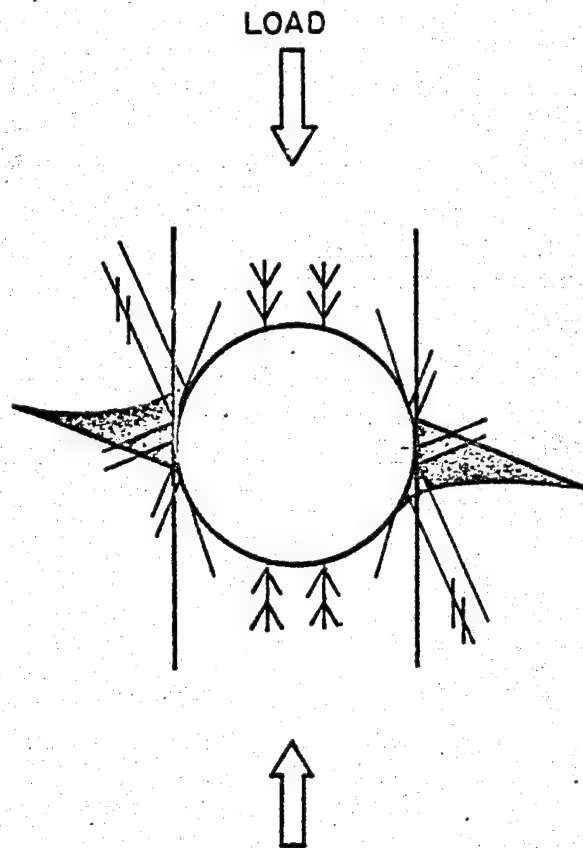
Figure 50. Schematic representation of the in-plane compressive fatigue damage state of the 42 ply specimens (shaded regions represent delaminations).
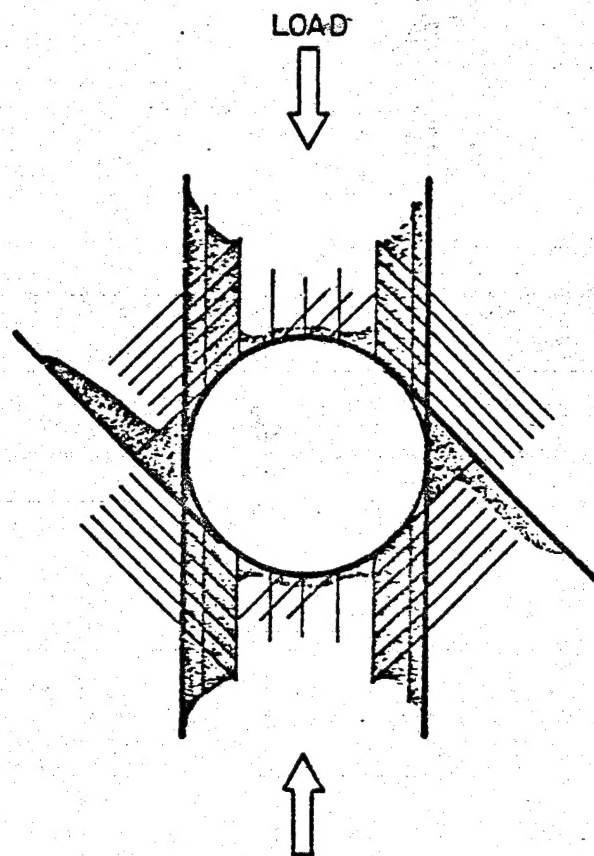
LOAD

Figure 51. Schematic representation of the in-plane compressive
fatigue damage state of the 48 ply specimens (shaded
regions represent delaminations).

VITA

Norman Frederick Black was born on October 29, 1958 in Perth Amboy, New Jersey, the first son, fourth of six children, borne to Bernard and Gloria Black. In June of 1976 he graduated from Sayreville War Memorial High School and the following September he enrolled at Virginia Polytechnic Institute and State University. As a senior he was a co-winner of the Dan Pletta Outstanding Engineering Science and Mechanics Senior Project Award. In June 1980 he received a Bachelor of Science degree in Engineering Mechanics and began graduate work. Following the completion of his Master of Science degree he will begin work with the Northrop Aircraft Corporation of Hawthorne, California in November, 1981.

Norman Frederick Black

DAMAGE DEVELOPMENT MECHANISMS IN NOTCHED GRAPHITE EPOXY COMPOSITE LAMINATES DURING COMPRESSIVE FATIGUE LOADING

by

Norman Frederick Black

(ABSTRACT)

This study has investigated the damage development mechanisms in notched graphite epoxy composite laminates during constant amplitude compressive fatigue loading. Laminates of two different stacking sequences were tested. The effect of the center notch on local stress-strain behavior during static loading, and the relationship between fatigue damage and the resulting life, stiffness, and strength of the laminates have been observed.

Several different nondestructive inspection (NDI) methods were used to characterize and monitor the damage that occurred during static and fatigue loadings. The NDI methods included X-ray radiography, stiffness monitoring, ultrasonic C-scanning, ultrasonic attenuation measurement, and acoustic emission monitoring. Sectioning of the damaged laminates was performed to verify the extent of the observed damage in the X-ray radiographs and ultrasonic C-scans.

Damage in both laminate types consisted of matrix cracking and delaminations. The growth of the damage was observed to have a three dimensional nature. Some correlations were found between locations of maximum interlaminar shear stresses, obtained from a finite element stress analysis, and the initial delaminations observed during cyclic loading.

138

END
DATE
FILMED
2-25-82
NTIS